FACULTY
OF MATHEMATICS
AND PHYSICS
Charles University

DOCTORAL THESIS

Michal Václavů

Low Platinum Content Thin Film Catalysts for Hydrogen Proton Exchange Membrane Fuel Cells

Department of Surface and Plasma Science

Supervisor of the doctoral thesis: Prof. RNDr. Vladimír Matolín, DrSc.

Study programme: Physics

Specialization: Physics of Surfaces and Interfaces

Prague 2016

First, I would like to thank my supervisor prof. RNDr. Vladimír Matolín, DrSc., for leading me during my study, helping with interpreting results and mostly and not lastly for his scientific support.

Next I would like to thank my consultant Doc. Mgr. Iva Matolínová, Dr. for helping not only with this work.

I would also like to thank all my colleagues who have helped me throughout my study with both science and non-science matters, especially Mgr. Filip Dvořák, Ph.D., Mgr. Roman Fiala, RNDr. Stanislav Haviar, Ph.D., Mgr. Ivan Khalakhan, Ph.D., RNDr. Ing. Tomáš Skála, Ph.D., RNDr. Michal Škoda, Ph.D., RNDr. Břetislav Šmíd, Ph.D., Mgr. Mykhailo Vorokhta, Ph.D.

Special thanks goes to Mgr. Jan Beran, Ph.D., Mgr. Tatiana Kolářová, Mgr. Olexander Stetsovych, Ph.D., RNDr. Lucie Szabová, Ph.D., Mgr. Klára Ševčíková, Ph.D. for sharing free time during research stay in Japan.

And I would like to thank all other colleagues from the Surface physics group for everyday advises, help, experiences and shared time.

I dedicate this work to my wife, who has been patiently supporting me during all the time of the writing.

Preface

The presented doctoral thesis is based on results that are or will be published in the following scientific publications:

- Vaclavu, M; Matolinova, I; Myslivecek, J; Fiala, R; Matolin, V
  Anode Material for Hydrogen Polymer Membrane Fuel Cell: Pt–CeO2 RF-Sputtered Thin Films
  J. Electrochem. Soc., **156** (8): B938–B942, 2009.
- Matolin, V; Cabala, M; Matolinova, I; Skoda, M; Vaclavu, M; Prince, KC; Skala, T; Mori, T; Yoshikawa, H; Yamashita, Y; Ueda, S; Kobayashi, K
  Pt and Sn Doped Sputtered CeO2 Electrodes for Fuel Cell Applications
  Fuel Cells, **10** (1): 139–144, 2010.
- Fiala, R; Vaclavu, M; Rednyk, A; Khalakhan, I; Vorokhta, M; Lavkova, J; Potin, V; Matolinova, I; Matolin, V
  Pt–CeOx thin film catalysts for PEMFC
  Catal. Today, **240** Part B (1 Feb): 236–241, 2015.
- Vaclavu, M.; Vorokhta, M.; Khalakhan, I.; Fiala, R.; Matolin, V.; Thin film PtCo enhanced activity PEMFC cathode catalyst. In process of publication.

except the above mentioned, Michal Václavů is a co-author in the following publications:

- Matolin, V; Matolinova, I; Vaclavu, M; Khalakhan, I; Vorokhta, M; Fiala, R; Pis, I; Sofer, Z; Poltierova-Vejpravova, J; Mori, T; Potin, V; Yoshikawa, H; Ueda, S; Kobayashi, K
  Platinum-Doped CeO2 Thin Film Catalysts Prepared by Magnetron Sputtering
  Langmuir, **26** (15): 12824–12831, 2010.
- Bruix, A; Lykhach, Y; Matolinova, I; Neitzel, A; Skala, T; Tsud, N; Vorokhta, M; Stetsovych, V; Sevcikova, K; Myslivecek, J; Fiala, R; Vaclavu, M; Prince, KC; Bruyere, S; Potin, V; Illas, F; Matolin, V; Libuda, J; Neyman, KM
  Maximum Noble-Metal Efficiency in Catalytic Materials: Atomically Dispersed Surface Platinum
  Angew. Chem.-Int. Edit., **53** (39): 10525–10530, 2014.
- Fiala, R; Vaclavu, M; Vorokhta, M; Khalakhan, I; Lavkova, J; Potin, V; Matolinova, I; Matolin, V

Proton exchange membrane fuel cell made of magnetron sputtered Pt–CeOx and Pt–Co thin film catalysts
J. Power Sources, **273** (Jan): 105–109, 2015.

- Khalakhan, I; Vorokhta, M; Václavů, M; Šmíd, B; Lavková, J; Matolínová, I; Fiala, R; Tsud, N; Skála, T; Matolín, V
In-situ electrochemical atomic force microscopy study of aging of magnetron sputtered Pt-Co nanoalloy thin films during accelerated degradation test
Electrochim. Acta, **211** (1 Sep): 52–58, 2016.

I declare that I carried out this doctoral thesis independently, and only with the cited sources, literature and other professional sources.

I understand that my work relates to the rights and obligations under the Act No. 121/2000 Coll., the Copyright Act, as amended, in particular the fact that the Charles University has the right to conclude a license agreement on the use of this work as a school work pursuant to Section 60 paragraph 1 of the Copyright Act.

In Prague, date..... signature

Title: Low Platinum Content Thin Film Catalysts for Hydrogen Proton Exchange Membrane Fuel Cells

Author: Michal Václavů

Department / Institute: Department of Surface and Plasma Science

Supervisor of the doctoral thesis: Prof. RNDr. Vladimír Matolín, DrSc.

Abstract: Novel type of catalyst for proton exchange membrane fuel cells anode is demonstrated. It is based on magnetron sputtered Pt-CeO_2 a Pt-Sn-CeO_2 mixed oxides. It is shown, that these materials allow to significantly decrease amount of platinum in the anode catalyst. The preparation method yields high amount of platinum in ionized form, especially Pt^{2+}, which is related to the high activity. Stability of these catalytic layers were investigated under conditions similar to fuel cell anode (humidified hydrogen at elevated temperature). Also interaction of hydrogen a water under UHV conditions were studied, demonstrating high stability of the Pt^{2+} species. In the last part of the work sputtered Pt-Co mixed catalyst were investigated to be used in the PEMFC cathode. It is demonstrated that at right conditions, the sputtered alloy catalyst improves mass activity on cathode by factor more than two.

Keywords: hydrogen fuel cell, magnetron sputtering, XPS, SRPES, platinum

Abstrakt: V práci je demonstrována účinnost nových typů katalyzátorů pro anodu vodíkových palivových článků s polymerní membránou na bázi Pt-CeO_2 a Pt-Sn-CeO_2, připravených pomocí magnetronového naprašování, které umožňují dosáhnout výrazného snížení obsahu platiny v anodovém katalyzátoru. Tento způsob přípravy umožňuje dosáhnout velké koncentrace platiny v iontovém stavu, zejména Pt^{2+}, která je dávána do souvislosti s vysokou aktivitou katalyzátoru. Je studován vliv nosiče katalyzátoru na výkon, dále je studována stabilita v prostředí palivového článku pomocí modelového systému. Byla studována interakce katalytických vrstev s vodíkem ve vakuu a za atmosférického tlaku, zvýšené teploty a vlhkosti. Byla potvrzena stabilita platiny v iontovém stavu i za podmínek panujících v palivovém článku. V další části práce je studována možnost snížení obsahu platiny na katodě s využitím naprašovaných katalyzátorů na bázi Pt-Co a Pt-Ni. Je ukázáno, že naprašovaný slitinový katalyzátor umožňuje zvýšit hmotnostně specifickou aktivitu více než dvakrát a byly vymezeny podmínky přípravy, které umožňují toto zvýšení.

Klíčová slova: vodíkové palivové články, magnetronové naprašování, XPS, SRPES, platina

Contents

1 Introduction: Catalyst for fuel cells

Modern society today increasingly depends on many mobile systems, which are used for transportation, communication, monitoring and supervision, including computers and various smart devices. In spite of the remarkable progress in the development of those devices and efforts in reducing energy consumption the suitable energy storage with large enough capacity is still required. At the same time there is still need for large scale power sources and the trend is to have decentralized power generation which can in extreme meaning each village or even individual household having its own power station and be independent on the centralized grid system. In both areas there are several approaches possible to solve the problem and among them electrochemical devices play very important role, because they allow direct conversion of stored chemical energy into electricity. Typical representative of the electrochemical energy releasing devices would be batteries and fuel cells (FC), each having its strong and weak points.

Fuel cells (FC) offer very good energy density, high conversion efficiency and virtually unlimited capacity depending on the available supply of reactants. Hydrogen fuel cells represent wonderful choice from the ecology point of view as they produce no emissions and the are key component in eventual hydrogen based economy of energy storage and production.

Proton exchange membrane fuel cells (PEMFC), as one of the several types, are expected to be future power production system for clean and efficient generation of electricity from hydrogen and even hydrocarbons for both mobile and small scale stationary applications.

Unfortunately, in many types of FCs the current technology need use of rare precious metals (mainly platinum) as the catalyst. Moreover, device construction is rather technologically complex and requires other advanced materials. This makes the FC relatively expensive solution and the problem of available supply of the rare metals in case of widespread use is open. Therefore, FCs are in the centre of intensive research and development, especially in the area of catalysts in order to minimize or eliminate completely the dependence on precious metals and improve efficiency.

Novel catalysts with high activity and low content of precious metals can be prepared by thin-film technologies such as physical vapour deposition (PVD) and sputtering. Such approach offers good control of the catalyst composition and structure at the microscopic level. Although these methods are not very common in industrial scale catalyst production and present a challenge it might open a way to unique and novel catalyst materials.

The main point of this work is about principal ways of how to reduce the precious metal content in the fuel cell catalyst needed.

One way is to use alloys of platinum with another less noble metal, this can be beneficial by improving structure and allowing to even tune electronic properties of the catalyst and thus improve the performance.

Another possible way is the use a "catalyst promoter", in this case a transition metal oxide interacting with the active metal is yielding completely new properties and structure.

PEMFC working principle

A typical hydrogen fed PEMFC consists of two electrodes in contact with a proton exchange membrane (PEM), which is in fact an acid electrolyte in solid form. In standard hydrogen and air (oxygen) fed FC the overall reaction looks like:

$$2\ H_2 + O_2 \rightarrow 2\ H_2O + \text{released energy} \qquad (1.1)$$

Practically there are two spatially separated half reactions taking place. On the anode the hydrogen ionises, creating protons and releasing electrons – hydrogen oxidation reaction (HOR):

$$2\ H_2 \rightarrow 4\ H^+ + 4e^- \qquad (1.2)$$

and on the cathode, oxygen reacts with protons coming through electrolyte and electrons coming via external electric circuit forming water – oxygen reduction reaction (ORR):

$$O_2 + 4e^- + 4\ H^+ \rightarrow 2\ H_2O \qquad (1.3)$$

Clearly, for continuous proceeding of both reactions, electrons produced at the anode must pass through an electrical circuit to the cathode while H^+ ions are passing there through the electrolyte. Important fact for correct function is that the membrane

(solid electrolyte) must be only proton (H^+) conducting.

The basic problem of this reaction is that an activation energy is needed to overcame energy barrier in the reaction pathway. Catalysts revealing large active surface and operation at increased temperature are necessary for the reactions to proceed at reasonable speed. The energy released in the reaction is partially in form of useful electric work (electrons going via external circuit) and in partially as heat.

The first demonstration of a fuel cell was documented in [1]. There are actually more types of fuel cells with little different chemical reactions working behind, but this is beyond the scope of this work. One can name a direct methanol fuel cell (DMFC) as one interesting example. DMFC is similar to hydrogen PEMFC, but the hydrogen ions are created by catalyst assisted decomposition of methanol. They can be supplied directly with (diluted) liquid methanol. They require special catalyst, particularly because CO poisoning at the anode has to be solved.

The principle common to all types of FC is the separation of the two half reactions and using the electrons flowing through external circuit to obtain electric work.

Cerium oxide in catalysis

Noble metal ceria-based catalysts are among the systems exhibiting strong metal-support interaction (MSI) effects [2] [3]. In recent years, much attention has been focused to CeO_2-supported noble metal catalysts due to their applications in automotive exhausts. Noble metal catalysts supported on Al_2O_3 are well-known three-way catalysts (TWC) [4], while CeO_2 is added as a promoter to TWC for its oxygen storage capacity (OSC) and stabilization of structure [5]. CeO_2 seems to have a promoting effect on the metal in addition to acting as a support as was reported for example for Pd-ceria activity towards CO oxidation reaction [6].

The Pt-cerium oxide systems have been shown to give high activity for hydrogen production [7], water-gas shift (WGS) reactions [8], CO and hydrocarbon oxidation [9], oxidation of ethanol [10] and decomposition of methanol [11].

The high activity for WGS reaction was associated with the presence of cationic platinum [8] [12] in cerium oxide. Ionic Pt dispersed on CeO_2 crystallite surface by the combustion method formed active adsorption $Pt^{2+,4+}$ sites which led to higher CO + NO and CO + O_2 reaction rates [13].

Ceria exists in two stable stoichiometries: CeO_2 and Ce_2O_3. The electronic structure of the CeO_2 is characterized by unoccupied 4f states of Ce^{4+} whilst the Ce_2O_3 (Ce^{3+}) has $4f^1$ configuration [14]. Studying the occupancy of the Ce 4f states is possible using photoelectron spectroscopy, which is a powerful tool for investigating electronic structure. There are many spectroscopic data showing different 4f configurations using Ce 3d spectra [15] [16][17].

There are several reports concerning the deposition of CeO_2 films using sputtering, mainly for superconducting and microwave applications, e.g. [18][19]. Recently it was reported that co-sputtering of cerium oxide with gold led to formation of a new type of thin film catalyst with high concentration of ionic gold in $Au^{+,3+}$ states [20].

Pt – cerium oxide in PEMFC anode

Catalysts made of platinum in pure form or alloyed with other elements are regarded as the only choice so far for high and stable performance of PEMFC [21][22]. As was mentioned earlier it is essential to find a way to decrease the Pt loading in FC electrodes and research of new low cost materials with high activity is necessary. One of the possible ways is to profit from the MSI effect known for platinum supported on various oxides, especially ceria.

Pt-oxide anode materials such as Pt-RuO_2 [23], Pt-SnO_2 [24], or Pt-WO_3 [25] [26] have been reported. Recently, also the anode properties of Pt-CeO_2 have been investigated for the development of direct methanol fuel cell (DMFC) [27][28]. The cyclic voltammetry showed that Pt-CeO_2 quality as a direct methanol FC anode material might be superior to that of Pt-Ru/CB [29]].

Interaction of ceria with hydrogen leads to higher concentration of Ce^{3+} ions due to surface reduction [30], i.e. creation of oxygen vacancies. A kinetic model of ceria reduction [31] proposes that ceria is reduced at first through a surface step of hydrogen dissociation followed by a bulk diffusion step. The activity of surface steps is highly increased by the presence of transition metal on the surface. Density Functional Theory (DFT) study [32] shows that adsorption of molecular hydrogen on ceria surface is energetically favoured and depends on the surface structure. Adsorption of an H atom causes $Ce^{4+} \rightarrow Ce^{3+}$ reduction of the nearest neighbour single Ce ion. Pt ions incorporated in CeO_2 matrix mostly in +2 oxidation states

enhances hydrogen molecule dissociation to protonic hydrogen and increase hydrogen storage capacity of the catalyst [33]. Similarly, ionic platinum has been found to facilitate the $H_2 + O_2$ reaction [34].

Generally accepted theory supposes that Pt^0 of nanosized supported particles is the most active site in the dispersed Pt-oxide catalysts. However, we have shown that fully ionic Pt^{n+}–CeO_2 catalysts of different concentrations of Pt deposited on CNTs by sputtering method exhibited high activity in hydrogen PEMFC anode [35] showing that cationic platinum is highly active species. We found that properties of the catalysts prepared in such a way resemble properties of the $Ce_{1-x}Pt_xO_{2-\delta}$ solid solution formed by the combustion synthesis [13] on a surface of cerium oxide nanopowder.

Carbon nanotubes as catalyst support

Carbon nanotubes (CNT) exhibit high electrical conductivities and excellent corrosion resistances. The CNT based FC electrode is suitable for the transfer of reactants in the catalyst layer leading to improved fuel cell reactions. For example a CNT supported PtRu anode catalyst for direct methanol FC applications has been successfully tested, e.g. [36]. Pt coating of CNT in the form of supported nanoparticles was reported in [37][38].

Sputtering deposition of catalyst layers

Sputtering is regarded as thin film technology method, which can be used in miniature and on-chip technology, where it simplifies the procedure, as it avoids any wet deposition techniques. Sputtering is not very commonly used to prepare catalysts, it have been shown however that it could be very useful in some applications [39]

Sputtering can be, however, viable method for producing catalytic materials [40]. But so far there are not many studies comprising catalysts prepared by this technique. The most challenging problem is to be able to prepare thin films which exhibit a high porosity. If this problem is managed, one key advantage of TF technology is a possibility to use wide range of materials, which in many respects exceeds those accessible by conventional (wet) preparation techniques. Almost any material combination at any composition is accessible, e.g. in form of composites, alloys, solid solutions, and mixed oxides.

The variation of deposition parameters (substrate temperature, deposition rate and angle, use of reactive atmosphere, plasma treatment, simultaneous or sequential deposition.

Its use would not be limited to standard PEMFC but it also opens a way to fabrication of micro-on-chip FCs [41][42] which requires use of planar technology.

Pt-Co PEMFC cathode

One of the obstacles to the widespread commercialization of PEMFCs is slow kinetics of the oxygen reduction reaction (ORR) at the cathode which then requires high loading of catalyst to be used. Platinum is so far the only proven and most frequently used catalyst. Therefore, it is essential for these limitations on Pt to be overcome or, at least, significantly reduced. In recent past many studies have shown that e.g. Pt-Co alloy catalysts could improve the catalytic activity and even stability relative to pure Pt [43][44]. Similarly also Pt-Ni alloys exhibit promising activities. [45]. Majority of the studies use PtCo alloy nanoparticles prepared by wet techniques, nevertheless magnetron sputtering can be used very effectively to prepare PtCo catalyst alloy by co-sputtering Pt and Co from dual sources.

Present targets in catalyst performance

In order to make fuel cell technology economic and competitive the FC cost should continue to be reduced. There are several aspects necessary to reach that goal, one of the most important ones is to increase the PEMFC power output per gram of Pt, leading to lowered need of the precious metal. The U.S. Department of Energy technical targets for electrocatalysts for transportation application describe 2020 targets as following: 8 kW/g of platinum group metal (PGM) and mass activity of (cathode) catalyst 0.44 $A.mg_{(PGM)}$ @ 900 $mV_{iR\text{-}free}$ [46].

Form of this work

First part, presented in chapter 3, contains characterization of a novel sputtered Pt-CeO_2 and Pt-Sn-CeO_2 catalytic layers which have been found very active

for use in anode of PEMFC. Three different catalyst supports for the use in PEMFC are compared.

In next chapter, investigation of stability of Pt-CeO_2 catalytic material is described. There were two studies done, one consisting of interaction with hydrogen and water in UHV conditions and the second interaction of humidified hydrogen with the catalyst at atmospheric pressure and PEMFC relevant temperature.

The chapter 5 is focused on decreasing platinum content in PEMFC cathode catalyst. Results from fabrication of Pt-Co and Pt-Ni mixed/alloy sputtered catalyst are presented.

2 Experimental methods

2.1 Magnetron sputtering deposition

Magnetron sputtering is a vacuum based PVD technique that uses specially shaped magnetic field in vicinity of sputtering target to enhance plasma discharge intensity, allowing for lower working gas pressure. Incident ions accelerated by electric field towards the target and sputter material from the target which is then deposited onto the sample. Schematic diagram of a magnetron source is depicted in fig. 2.1.1.

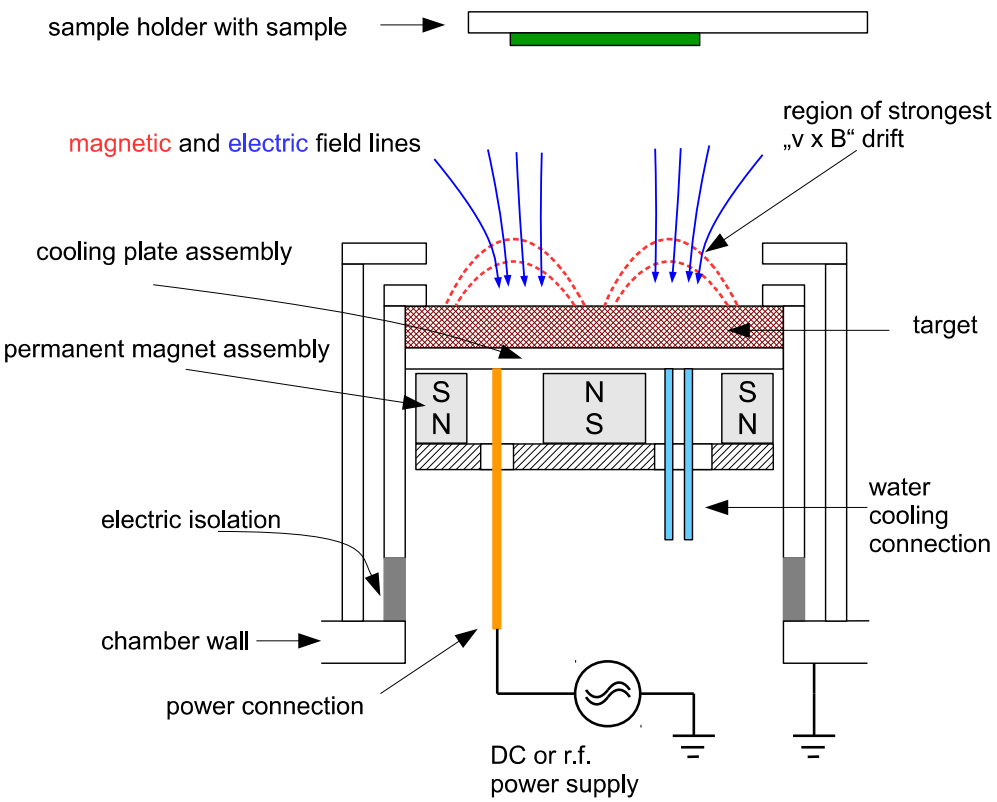

Figure 2.1.1: Schematic diagram of typical setup of magnetron sputtering device

There are many ways in which sputtering conditions can be varied to tune sputtered layer properties. For example deposition angle, use of reactive sputtering, applying bias voltage to samples can influence deposited layers.

In order to deposit a mixed material, it can be done either by simultaneous deposition from multiple sources, or it can be done from single source using composite target.

To prepare some of the samples presented in this work (e.g. Pt-CeO_x catalytic layers) a special configuration of composite target was used. A piece (or several) of metal wire (platinum, tin) was placed radially onto the ceria target. This way it was possible to prepare layers continuously doped with relatively small amount of metallic dopant. An example of the platinum-CeO_2 composite target made from platinum wire, captured during sputtering, is in Fig. 2.1.1.

Classical magnetron sputtering uses DC source to drive the discharge. This works very well but the requirement is that the target has to be conductive. In case of non-conductive targets the solution exist by using high frequency (alternating current) power source. Typically generator with standard industrial frequency 13,56 MHz is used. In this case of a.c. powered discharge, the method is called „radio frequency sputtering" or „r.f. sputtering".

Shortly, the basic properties of r.f. discharge are determined by fact that the light electrons can easily match the changes of electric field at this high frequency whereas the much heavier ions are already too slow and merely drifting in mean static field created by plasma potential in combination with small-amplitude oscillation. Because of the different mobilities of electrons and ions the time evolution of plasma potential V_p is non symmetric during the applied a.c. voltage (V_p is positive, bigger than zero). Moreover because area of the two electrodes, chamber walls and target, is different, the voltage difference between V_p and chamber walls (typically several Volts) is only a fraction of the voltage difference between plasma and target (typically hundreds of Volts) [47]. This voltage difference is then the driving force for the motion of charged particles. The mean value of difference between target voltage and V_p can be measured as a "self bias voltage" on the target, effectively accelerating ions to sputter material from the target. Consequence of this is, that during the r.f. sputtering, also the samples are impacted by ions from the plasma, but generally the flux and energy are very small. Anyway it can have beneficial effects on the properties of the deposited layer.

Figure 2.1.2: Photography of magnetron plasma discharge in argon during operation. Note the wire on right side made of platinum, forming composite target with CeO_2. This is one of the possible configurations that can be used to prepare sputtered Pt-CeOx mixed oxide

Sputtering apparatus used at the Department is equipped with two magnetron sources (both using targets of 51mm or 2 inch diameter), the typical sample distance from target is 90mm from the main, center position magnetron. Second side positioned under 45 degrees can have variable sample target distance, starting from 120 mm.
The chamber is equipped by dual gas inlet control system using metering valves and working pressure regulating valve. Description of the sputtering apparatus including the two independent magnetron sources can be found for example in [48].

Problematic of sputtering and generally vacuum deposition techniques is very wide and there are many sources of information such as [49].

2.2 Photoelectron Spectroscopy

Photoelectron spectroscopy (PES) studies properties of materials by using photons as primary probe and detecting emitted photoelectrons due to photoelectric effect. PES belong to very surface sensitive methods as the information depth is given mainly by inelastic mean free path (IMFP) of photoelectrons, which is typically in the order of several nm.

Basic equation for emission of photoelectrons:

$$E_k = h\nu - E_B - \Phi_S \qquad (2.1)$$

where E_k is kinetic energy of detected photoelectron, h is Planck constant, ν photon frequency, E_B binding energy (BE) of electron in initial state, Φ_S is work function of the detection system of the spectrometer. This formula is valid, when the Fermi level of the sample and detector are equalized by e.g. conductive connection.

The process of photoemission is described well be the "three step model" (I. electron optical excitation, II. electron transport through the solid, III. electron escape from surface). The measured spectrum of kinetic energy of electrons or energy distribution curve (EDC) contains rich variety of information.

The basic information comes from the density of states (DOS) and occupation of them in the material. Since every atom has characteristic energy levels, it is possible to do chemical identification. Secondly because chemical bonds influence the DOS, it is possible to observe "chemical shifts" in the EDC. EDC also contain various signals from elastic and inelastic processes.

X-ray photoelectron spectroscopy (XPS)

The XPS method uses characteristic radiation from classical X-ray source (typically Al or Mg Kα) as primary probe, is due to relatively compact setup widely used for laboratory characterization of materials.

It is possible to quantitatively determine composition of probed material (its surface region), on assumption of homogeneity and flatness, using simple method:

$$n_i / n_j = I_i.S_i^{-1} / (I_j.S_j^{-1}) \qquad (2.2)$$

where n_i is concentration of given element, I_i is peak area and Si is a sensitivity factor, which ideally includes are parameters determining the final intensity of element signal (emission angle, photoionisation cross-section, transmission function of detector, IMFP)

Almost all XPS measurement were performed on apparatus at Department of Surface and Plasma Science laboratory, in an ultrahigh vacuum (UHV) experimental chamber operating at base pressures $<5\text{-}10^{-10}$ mbar and equipped with a SPECS Phoibos MDC 9 electron energy analyser and a dual Mg/Al X-ray source. Most of photoelectron spectra were measured using higher energy of Al X-ray source ($h\nu$ = 1486.6 eV, ΔE = 1 eV). I some cases in order to change surface sensitivity XPS was measured at two photoelectron emission angles 20° and 60° with respect to the surface normal.

Determining the composition of sample (e.g. atomic concentration of Pt in ceria) was done using XPS data, calculated from ratio of area of Ce 3d region and area Pt 4f region, corrected by corresponding sensitivity factors (values for 54.7 deg source angle were used) [50]. It should be noted, that this method only takes into account the average composition near the surface of the sample, from where comes useful XPS signal. This may be different from the composition of the bulk material. However when used on sputtered samples without any treatment, it is reasonable to consider that the difference would be negligible.

Synchrotron radiation photoelectron spectroscopy (SRPES)

The benefits of using tunable synchrotron radiation for PES are mainly possibility to choose information depth, photoionisation cross-section, high intensity, spatially focus beam and many others. It allows also to use advanced PES techniques.

SRPES measurements were performed in an ultrahigh vacuum chamber of the experimental system at the Materials Science Beamline (MSB) at the Sincrotrone Elettra Trieste light source. The bending magnet source provides synchrotron light in

the energy range of 21–1000 eV. The UHV station (base pressure 2×10^{-8} Pa) is equipped with a Specs Phoibos 150 electron energy analyser and a dual Mg/Al X-ray source (for illustration a typical resolution for Pt 4f spectra at hν = 180 eV: ΔE = 200 meV).

Resonance photoelectron spectroscopy (RPES)

The RPES method is wonderful tool that can be used to study electronic structure of valence band of certain materials. What makes this special is the ability to selectively detect only signal coming from states of certain element and separate then from other states. In this case it was applied for determining occupation of Ce 4f states in ceria, which are directly related to the reduction state of the ceria. RPES of ceria is based on measuring valence band (VB) photoemission spectra with SRPES at photon energies corresponding to the 4d→4f resonance either for the Ce^{3+} or the Ce^{4+} ions. The Ce^{3+} resonance at a photon energy of 121.4 eV is caused by a super Coster−Kronig decay involving electron emission from the Ce 4f states located about 1.4 eV below the Fermi edge. On the other hand Ce^{4+} resonance at photon energy of about 124.8 eV involves emission of electrons from O 2p states hybridized with Ce 4f states in the VB around 4.0 eV. In order to subtract "background", the VB spectrum at photon energy of 115 eV (off-resonance) is additionally measured. Resonant enhancements for Ce^{3+}, D(Ce3+) and for Ce^{4+}, D(Ce4+) are quantified by calculating the intensity difference between the corresponding features in and off-resonance [51]. The amplitudes of D(Ce3+) and D(Ce4+) are then directly proportional to the concentrations of Ce^{3+} and Ce^{4+} ions in the sample, respectively. Extent of the reduction of ceria then can be defined as resonance enhancement ratio (RER):

$$RER = D(Ce3+) / D(Ce4+) \quad (2.3)$$

Example of the result of RPES measurement from ceria sample is given in fig. 2.2.1.

More information on PES and details on specific usage of the various methods can be found for example in a book [52]

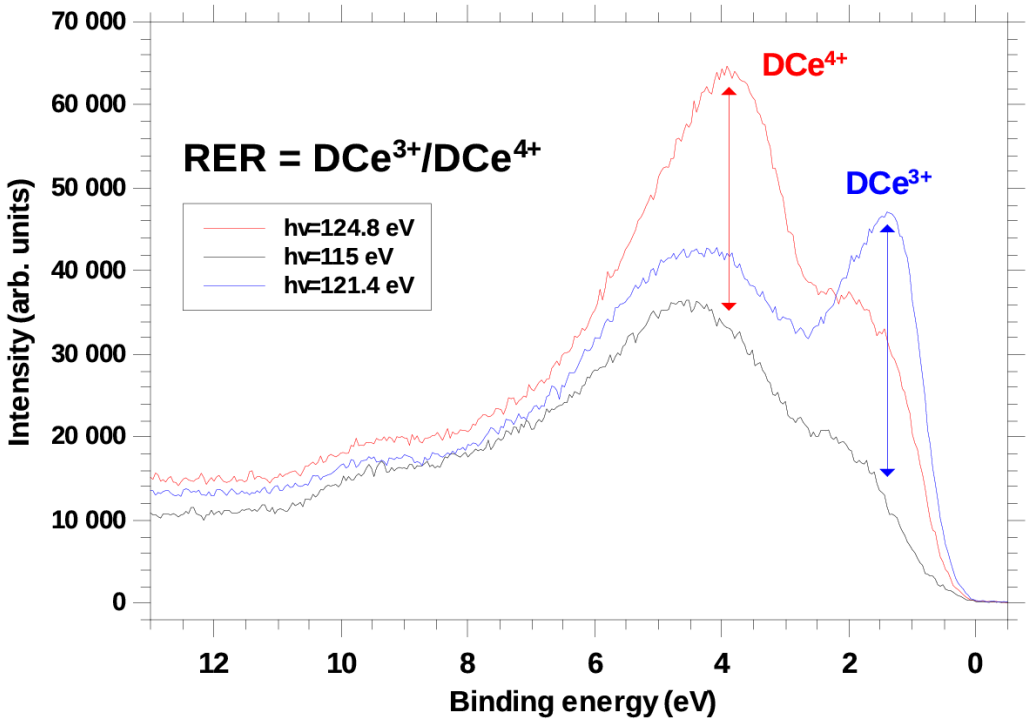

Figure 2.2.1: Example of RPES spectra of valence band region showing resonance enhancement of Ce signal from different states using variable photon energy. Data originates from sample "Pt-CeO_x LowPt", after heating to 400K, in chapter 4.

2.3 Scanning Electron Microscopy, Energy Dispersive X-ray Spectroscopy, Transmission electron microscopy

Scanning Electron Microscopy (SEM) is helpful and indispensable method in research of catalysts as it provide fast and detailed enough images of surface morphology with resolution up to several nm. The primary probe is a focus electron beam with energy of electrons of typically several to tens of keV, which scans over the sample. Images is created from chosen signal type, typically either secondary electrons with low energy or back-scattered electrons with higher energy. Each type of signal can provide different contrast. Typically only surface region of sample is probed.

When the primary beam has high enough energy, it can excite X-rays when interacting with atoms in the sample. This is basis for the method of Energy Dispersive X-ray Spectroscopy (EDX). As each type of atom emits characteristic radiation, chemical analysis can be including quantitative analysis. Due to properties of primary beam and low absorption of X-rays in solid, the information comes from region with depth up to about a micrometer.

Transmission electron microscopy (TEM) can be used to image samples with higher resolution as the primary energy is typically an order higher than in case of SEM and beam diameter is smaller. It needs thin samples, in order for the electrons to get through. There are many modes in which the TEM can be used, typically to obtain high resolution/magnification images or studying crystallographic properties of samples.
More information about electron microscopy can be found for example in [53].

In this work SEM images were acquired by using a TESCAN MIRA (in some cases, TESCAN MIRA 3) microscope, equipped with Bruker EDX detector. Typical electron beam energy used to image samples was 30 keV.

TEM images were obtained using the 200 kV JEOL 2100F microscope. The images were recorded by an on-line charge-coupled device camera, and the analyses of the results were performed using the Digital Micrograph software. The samples for TEM observation have been made by using Focus Ion Beam (FIB) (Tescan LYRA FIB-SEM) technique to create thin lamellas suitable for TEM.

2.4 Atomic Force Microscopy

Atomic force microscopy (AFM) is a powerful method for determination of sample morphology with high lateral resolution (5nm) and exceptional vertical resolution (0.1 nm). It is based on detection of microscopic forces between surface of the sample and very small atomically sharp tip (10nm radius). The tip probe is rastered over the sample and thus a map of surface heights or other characteristics is created.
There are many modes of operation, how the interact with the surface. Basically they can be divided into contact and non-contact modes. More information can be found for example in [54].
In this work an AFM instrument by Veeco, Multimode V was used to acquire AFM

images.

2.5 FC testing, polarization curve, reaction kinetics, simple model of polarization

Fuel cell testing is important when catalyst performance should be evaluated in conditions that are similar to real working conditions. Here in this work the focus is explicitly on PEMFC using hydrogen as fuel.

In order to simulate the real conditions it is necessary to control several parameters, that includes working temperature of the fuel cell, reactant gas flow, reactant humidity and temperature and reactant pressure. And moreover there is ideally a computer controlled electronic load or a potentiostat necessary in order to control working point of the fuel cell and to measure polarization curves.

To control all of these parameters it is necessary to have quite complex system of controllers (temperature, gas flow, pressure), humidifiers, and so on. All of this necessary hardware forms a testing station.

The active part fuel cell itself is the so called Membrane Electrode Assembly (MEA). It consist of two electrodes containing gas diffusion layers (GDL) and catalyst. GDL together with catalyst can be called gas diffusion electrode (GDE). These two electrodes are then attached to membrane (solid electrolyte), forming the MEA. For PEMFC the material of choice for the membrane is typically Nafion, a trademark for a type of tetrafluoroethylene derived fluorinated copolymer [55], which is excellently proton conductive (if properly hydrated) while at the same time has high resistivity for electrons and anions and have excellent thermal and mechanical stability. The necessity for hydration is one of only few drawbacks.

For FC to work, the membrane electrode assembly (MEA) is enclosed between cell gas distributor plates serving at same time as current collectors a thermal regulation elements. Example of cells, that were used throughout the time at the department are shown in Fig. 2.5.2. The 1 cm^2 stainless steel cell on Fig. 2.5.2(left) uses silicon rubber gaskets to seal gas leakage, the commercial cell (middle) seals via Nafion membrane itself with addition of suitable PTFE foil spacer. The 5 cm^2 cell (right) has integrated double edge silicone sealing on each plate which seal directly against the Nafion membrane.

For testing this assembled cell is connected into testing station and testing procedure is carried out.

Typical testing procedure consist of break-in procedure, characterization by polarization (sequence of several measurements), eventually impedance spectroscopy characterization, and at the end electrochemical analysis. In our laboratory we use custom designed protocol which is derived from standard testing protocols, e.g. [56].

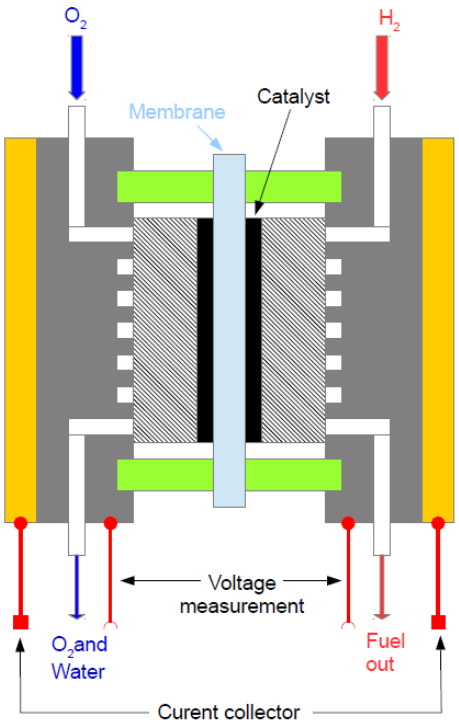

Figure 2.5.1: Typical PEMFC fuel cell testing hardware schematic and operation

As the basic characterization of FC performance serves the so called polarization curve (in fact it is a volt-ampere characteristic or IV curve), which describes cell voltage versus sourced current density. For a given fuel cell assembly, the most important factors influencing its performance is a) catalytic activity of the catalyst (combined from two simultaneous electrode reactions), b) DC electrical resistance of internal components (solid electrolyte protonic resistance, contact resistance between current collectors and catalyst and catalyst-electrolyte resistance), c) limitation in reactant mass transport to the catalyst (concentration polarization losses)

Figure 2.5.2: Fuel cell testing hardware. Left: Old laboratory-made design, 1cm² electrode area, stainless steel. Middle: commercial cell 1 cm² (Electrochem.org), graphite plates. Right: modern cell with 5cm² active area (TP-5, Greenlight Innovation), graphite plates. Designed for fast assembly/disassembly, pneumatic compression holder allows quick and easy exchange of cell.

From polarization curves it is possible to obtain maximum power density, which is good characteristic for the current FC assembly as a whole and assuming, the variation of external parameters are not changing much also of the catalyst.
Also it is possible to obtain the value for mass activity (for the cathode), assuming the conditions are set right, so the mass transport limitations are not present. This is done by using pure oxygen and hydrogen and using high stoichiometry for flow of oxygen.

The mass activity of the catalyst A_M is given by the equation:

$$A_M = i_{0.9} / W \qquad (2.4)$$

where $i_{0.9}$ is the current density in mA.cm^{-2} (corrected for any crossover current) determined from the polarization at voltage of 0.9$V_{iR\text{-}free}$ (after correction for Ohmic losses) and W is platinum or platinum group metals (PGM) loading per electrode area in mg.cm^{-2}.

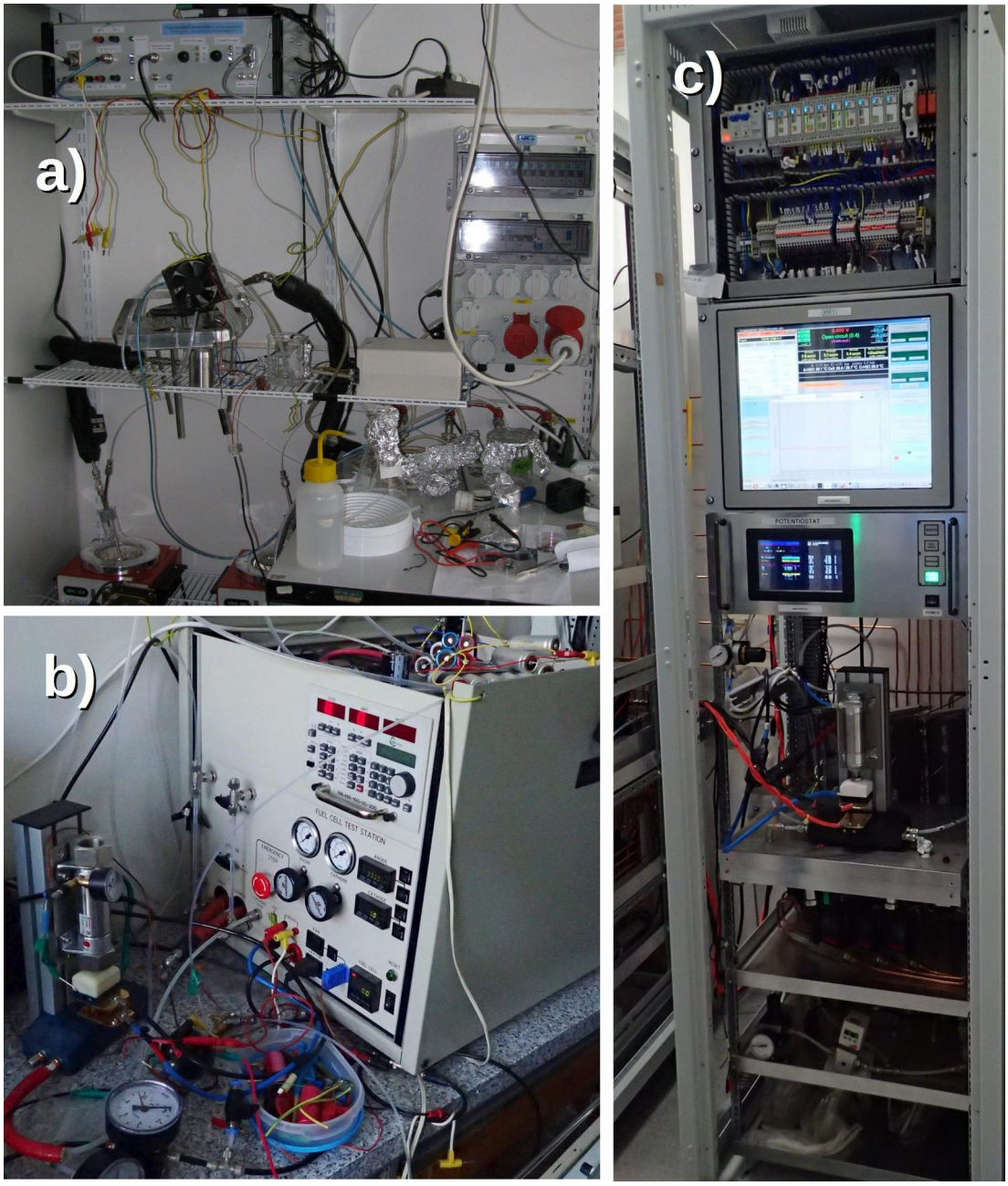

Figure 2.5.3: Photography of testing stations used to measure fuel cell samples. a) oldest, simple laboratory-designed station; b) commercial testing station (FCT Technologies) and c) newest, laboratory-designed station will full computer control of many process parameters.

Specific activity of the catalyst A_S is given by the equation:

$$A_S = i_{0.9} / Sr = A_M / ECSA \qquad (2.5)$$

where *i0.9* is the current density of $0.9V_{iR\text{-}free}$, same as in eq. 2.4, S_r is real (accessible) electrochemical surface area (in cm_{micro}^2) and *ECSA* electrochemical specific surface area ($cm_{micro}^2.g^{-1}$). It is obvious that the two activities are related together by value of ECSA.

The Electrochemical specific surface area (ECSA) is a measure of number active sites that are present in the catalyst by using certain amount of platinum loading. It can be determined using cyclic voltammetry directly with assembled MEA, using a two electrode connection, where one of the MEA electrodes (e.g. anode, when the cathode is to be characterized) works both as counter and reference electrode. The side serving as working electrode is fed with nitrogen, whereas the other part is fed by hydrogen or diluted hydrogen. During the cyclic voltammetry the charge corresponding to adsorbed hydrogen desorption is measured.

Alternatively and in case of platinum based catalyst more precise way is to use so called CO stripping method, which consist of evaluation amount of elector-oxidized CO adsorbed to the electrode active sites after electrode pre-exposition with CO. More details can be found for example in [57].

Electrochemical Impedance Spectroscopy

Electrochemical impedance spectroscopy (EIS) is powerful tool which allows

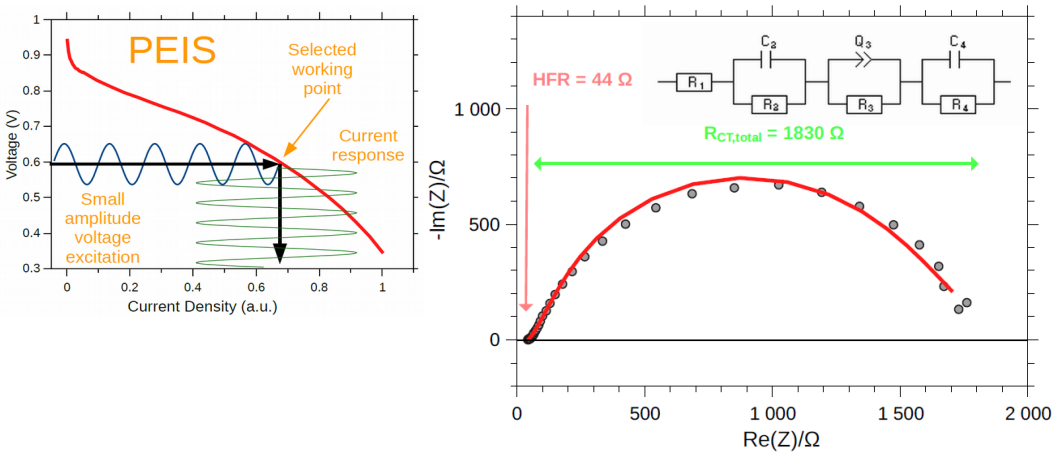

Figure 2.5.4: Schematic of PEIS measurement and example of a Nyquist plot

internal parameter analysis of electrochemical devices in operando. The principle is based on exciting an a.c. electrical signal response from studied devices. By

possibility of scanning over wide range of frequencies a model can be made fitting the obtained dependencies determining parameters of model principal components. Schematically is method described in Fig. 2.5.4. More information is provided e.g. in [58].

Cyclic voltammetry – ECSA and crossover current determination

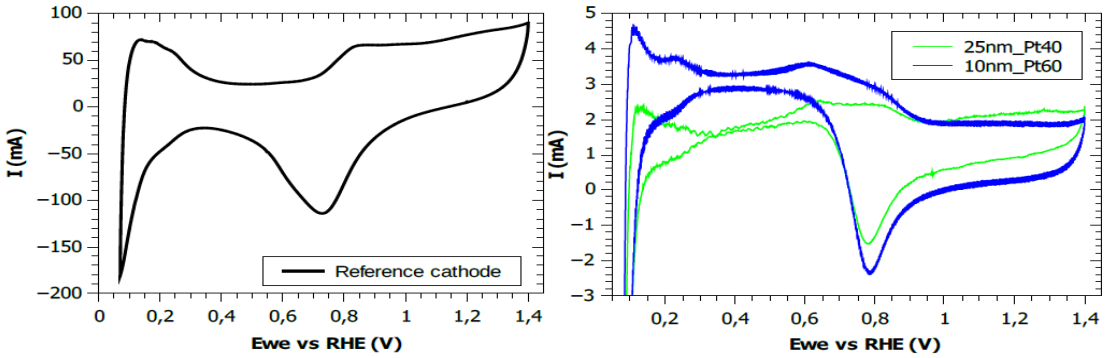

Figure 2.5.5: Cyclic voltammetry in situ fuel cell setup - commercial cathode (left) and sputtered layer of PtCo(right) in the role of working electrode with fuel cell anode in role of both reference and counter electrode. Fuel cell anode was fed with 30 sccm H_2, on cathode was used 30sccm of N_2. Scan rate 100 mV.s^{-1}

The in-situ Cyclic Voltammetry (CV) measurements can be done in simplified 2 electrode set-up, with the flow hydrogen on reference electrode(and counter electrode at the same time) and nitrogen on working electrode.

ECSA can be measured as the charge associated with H_2 adsorption/desorption in the low potential region of the voltammogram. Background (double-layer effect) subtraction is necessary. Example of CV used to determine ECSA is on Fig. 2.5.5.

A convenient indirect method of hydrogen crossover can be done using linear sweep voltammetry.

More information can be found in book [59].

Kinetics of electrochemical reactions, ORR

Electrochemical reactions can be described very well using Butler-Volmer

equation, which relates observed voltage resp. overpotential and current flowing through the electrode (reaction always proceed both directions close to equilibrium):

$$i = i_0 . \left[\exp\left(\frac{\alpha_a z F \eta}{RT} \right) - \exp\left(- \frac{\alpha_c z F \eta}{RT} \right) \right] \quad (2.6)$$

where i0 is exchange current density, α is

Tafel equation

$$\eta = \frac{RT}{\alpha z F} . \ln\left(\frac{i}{i_0} \right) \quad (2.7)$$

A simple model for polarization of the fuel cell which includes overvoltage (voltage loss) from Ohmic resistance, activation polarization (reaction kinetics) and simple mass transport limitation can be written as follows:

$$U(i) = E_0 - \Delta V_{ohm} - \Delta V_{act} - \Delta V_{trans} \quad (2.8)$$

Activation polarization can be express by Tafel equation when far from equilibrium and mass transport losses can be well modeled by a simple exponential term. Then the equation can be written as:

$$U(i) = E_0 - i\, r - A \log_{10}\left(\frac{i + i_n}{i_0} \right) + m \exp(n i) \quad (2.9)$$

Because exchange current density is property that is very difficult to measure directly, it is much more practical to use value of current at some more practical value. Voltage of 0.9ViR-free is typically used to measure current, which in this case is very close to purely kinetic limited value. This value is then typically used to calculate mass activity.

The previous equation can be transformed from exchange current density to using value of current at other potential (marked as x) (as long as Tafel equation is valid for the dependency):

$$A\log_{10}(i_0) \equiv E_x - E_0 + A\log_{10}(i_{x,iR\,Free}) \quad (2.10)$$

We can get a more convenient form, by choosing 900 mV as the potential for defining the value of reference current density. Using the value of $i_{900mV,iRFree}$ the formula becomes

$$U(i)[V] = 0.900 - i\,r - A\log_{10}\left(\frac{i+i_n}{i_{900\,mV,iR\,Free}}\right) + m\exp(ni) \quad (2.11)$$

Example of using this model to depict various losses in a real polarization curve is displayed in Fig. 2.5.6

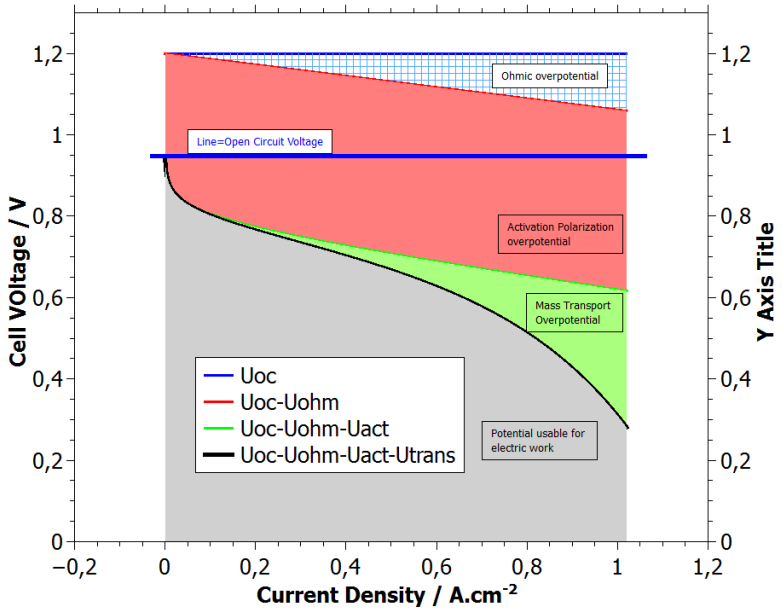

Figure 2.5.6: Distinguishing losses during polarization - based on the model (eq. 2.11) used to simulate the polarization curve of a real fuel cell (in this case sample 25nm Pt100) and assuming the parts in the equation correspond good enough to the real effects influencing the performance of the cell, it is possible to estimate extent of individual type of losses - ohmic, kinetic/activation and mass transport depending on the current flowing through the cell

Normally the anode kinetics is by several orders so we do not observe any Tafel slope from anode polarization, but in some cases (e.g. during CO poisoning) it might

become slow, then combined Tafel slope would be observed. ORR on cathode typically show a Tafel slope of about 60 mV.dec in low current density region/ high voltage (2 electron process, oxidised surface of platinum) and about 120 mV.dec for high current density region/ voltage below about 0.8 V (apparently 1 electron process, it is actually the result of the limiting step, although the reaction in this regime runs as 4 electron process)

3 Novel anode material for hydrogen polymer membrane fuel cell

In this chapter simultaneous magnetron sputtering of platinum and cerium oxide which provides oxide layers continuously doped with $Pt^{4,2+}$ ions during the growth is reported. It is shown that these Pt doped cerium oxide films exhibit an unusually high concentration (nearly 100%) of cationic platinum Pt^{2+} and Pt^{4+}, which makes it an interesting material for catalytic purposes. When used as anode material in hydrogen PEMFC Pt embedded in sputtered ceria films exhibits very high specific power (W/mg) showing that such material represents a promising alternative catalyst for FC applications. In order to elucidate the origin of the activity, there were several following experiments conducted.

3.1 Pt-CeO_2 thin films sputtered on double wall carbon nanotubes

The films were deposited onto carbon microfibre gas diffusion layer (GDL) (Alfa Aesar, Toray carbon paper, teflonated, TGP-60) enhanced by coating with double wall carbon nanotubes (DWCNT), forming a nanostructured fuel cell anode GDL. The GDL were coated with the carbon nanotubes by spin coating of the DWCNTs (Aldrich) dispersed in water. The GDL/DWCNT was then catalysed by using non-reactive r.f. magnetron sputtering deposition of a Pt–CeO_2 30 nm thick thin film. Simultaneously the layer was prepared on Si(100) wafer. On the same set of substrates also pure CeO_2 layers were deposited for comparison.

CeO_2 sputtering was performed from CeO_2 target while the Pt–CeO_2 thin films were deposited from a composite target prepared by placing pieces of 0.5 mm thick and 10 mm long Pt wire on the ceria target surface in the radial direction. In both cases r.f. power of 80 W and working pressure of argon of 6×10^{-1} Pa were used.

Typical deposition rate was 1 nm/min, more details about sputtering apparatus are in chapter 2.1.

Catalyst morphology and structure

AFM measurements of a reference catalyst film deposited on Si(100) wafer reveal a very porous surface with depth exceeding 30 nm and smallest crystallites below 10 nm in diameter (Fig. 3.1.1 b). The polycrystalline character of the oxide deposit is well shown also on the SEM image of the reference film (Fig. 3.1.1 a).

The equivalent compact layer thickness was determined to be 30 nm by means of the SEM cross-sectional view of the reference film which was deposited on a Si wafer simultaneously together with catalyst films. The X-ray diffraction (XRD) pattern of Pt doped ceria film showed only diffraction features which can be associated with CeO_2. The average ceria grain size determined by Sherrer formula from the (220) CeO_2 pattern is 4.4 nm. Pt diffraction features were not visible indicating very small size of Pt particles or amorphous structure.

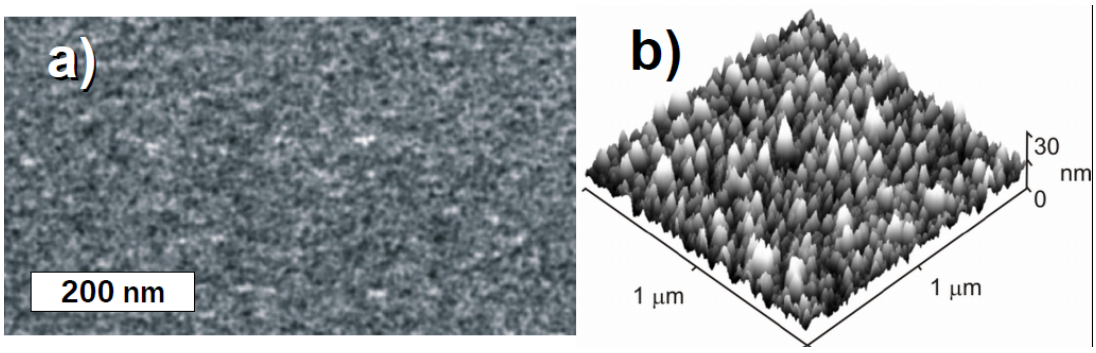

Figure 3.1.1: a) SEM image of the catalyst thin film deposited on Si wafer (30nm thickness) b) AFM image showing surface morphology of the same sample

Photoelectron spectroscopy results

The 3d core level XPS (1486 eV) spectrum of the CeO_2 film deposited without adding Pt is presented in Fig. 3.1.2 (bottom curve). It consists of three $3d_{3/2}$-$3d_{5/2}$ spin-orbit-split doublets characteristic of stoichiometric CeO_2 (Ce^{4+}). The doublets represent different 4f configurations in the photoemission final state and arise from Ce 4f hybridization in both the initial and the final states [15]. The

appearance of a high f^0 signal, together with an f^2 peak which is less intense than the f^1 peak, can be taken as evidence of the formation of CeO_2 [16][15][60]. In Fig. 3.1.2, upper spectrum, the XPS Ce 3d spectrum obtained for the cerium oxide film doped with Pt is shown. It can be seen that the spectra are almost identical, there is no measurable influence of added Pt on the cerium oxide stoichiometry in this case.

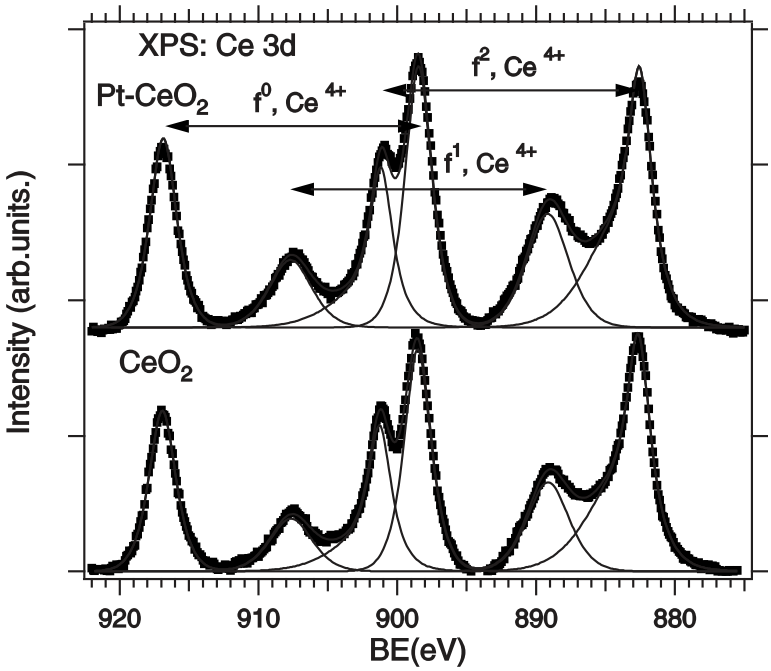

Figure 3.1.2: Ce 3d core level XPS spectra of CeO_2 (bottom) and Pt-CeO_2 (top) catalysts

The Pt 4f PES spectra obtained for the Pt doped ceria film are plotted in Fig. 3.1.3. By taking spectra at different photon energies we changed the information depth of the analysis. The bottom Pt 4f spectrum in fig. 3.1.3 was obtained by Soft X-ray PES (SX-PES) at $h\nu = 180$ eV. For $h\nu = 180$ eV the kinetic energy of the Pt 4f photoelectrons is close to 110 eV corresponding to an inelastic mean free path in CeO_2 of $\lambda = 0.5$ nm [61].

The spectrum exhibits a main doublet at 72.85 eV corresponding to Pt^{2+} species [8]. The doublet shifted by 1.4 eV to higher BE corresponds to Pt^{4+}. Small peak at 71.8 eV shows Pt^0 state. This energy is slightly higher than that expected for metallic platinum, this shift can be explained, however, by a size effect in PES, which is generally observed for very small particles (below 2 nm).

In order to change the surface sensitivity of XPS we measured the photoelectron emission for different angles of outgoing electrons relative to the surface normal. In Fig. 3.1.3 we compare spectra taken at 60° ($\lambda = 1$ nm) and 20° ($\lambda = 2$ nm) [61]. At $h\nu = 1486$ eV relative intensity of Pt^{4+} increases while Pt^{0} signal becomes practically negligible compared to surface sensitive SX-PES spectra.

The relative concentrations of different Pt species determined by decomposing the spectra by fitting into particular components are presented in Table 3.1.1.

Pt 4f XPS spectra obtained for a photoelectron escape angle of 60° (higher surface sensitivity) and 20° (lower surface sensitivity) show Pt^{4+}/Pt^{2+} ratios of 0.77 and 1.06, respectively, i.e. a substantial increase of the Pt^{4+} signal for lower surface sensitivity.

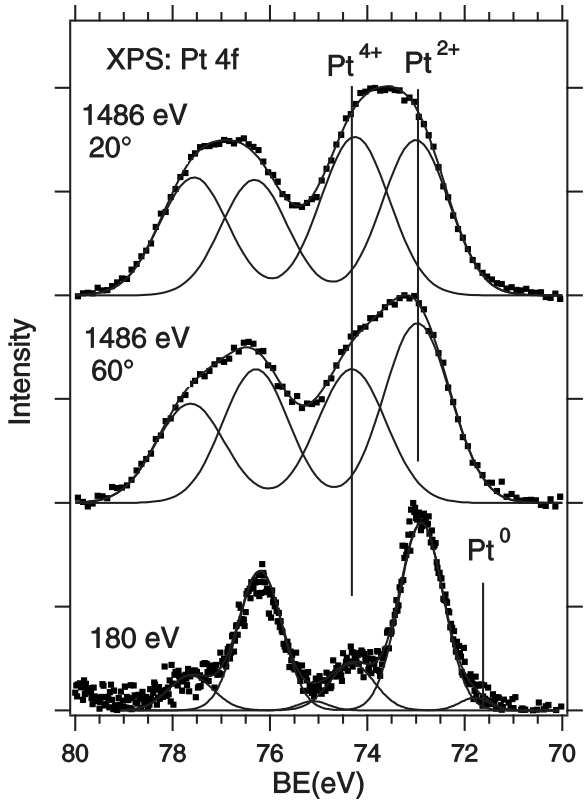

Figure 3.1.3: Pt 4f spectra of Pt-CeO_2, using different photon energy and emission angle to change information depth

A simple estimation based on the enhancement of the Pt^{4+} signal as a function of λ leads to a structural model with very low concentration of metallic platinum

(3.5%) on the surface, Pt^{2+} rich Pt-ceria interface and surface region, similarly as for gold ceria interface in [62][63], and Pt^{4+} dispersed in the ceria film bulk. The most probable picture of the Pt-CeO_2 r.f. sputtered films growth is that of the Pt4+ cations embedded in the growing film and of a very limited segregation of metallic platinum at the surface. The amount of surface Pt increases with increasing concentration of the Pt dopant, this is supported by results in next chapter.

Pt/Ce atomic concentration ratio Pt/Ce = 0.05 were determined from XPS (20°) Ce 3d and Pt 4f peak areas by using the XPS atomic sensitivity factors. It should be noted that the Pt concentration determined in this way corresponds to an average Pt concentration in the surface layer probed by XPS, which is approximately 2 nm thick, and could differ from that of the film bulk.

Photon energy/ emission angle	Pt^{4+}/Pt^{2+}
180 eV/ 0 deg	0.24
1487 eV/ 60deg	0.77
1487 eV/ 20deg	1.06

Table 3.1.1: The ratio of Pt^{4+} and Pt^{2+} content in Pt-CeO_2 determined with different surface sensitivity using Pt 4f peak area

Membrane electrode assembly preparation

The MEA with an active area of 1 cm^2 for FC testing were created by combining the carbon nanotubes enhanced GDL coated by Pt-CeO_2 sputtered catalyst with pretreated Nafion 0.09 mm thick membrane and with cathode electrode made from commercially available catalyst. The pretreatment of Nafion membranes was performed by using a standard process of boiling in H_2O_2 solution, diluted H_2SO_4 and H_2O [64]. The cathode electrodes were made by carbon-supported Pt/C powder (Alfa Aesar, platinum, nominally 40% on carbon black) mixed with the Nafion solution (Alfa Aesar, perfluorosulfonic acid–PTFE copolymer, 5% w/w solution) and coated onto the microporous GDL (Alfa Aesar, Toray carbon paper, teflonated, TGP-H-60). The loading of Pt in the cathode catalyst layer was 5 $mg.cm^{-2}$.

In order to compare performance with a commercially available catalyst, a reference MEA was prepared by using commercial catalysts on the anode. PtRu

powder catalyst (Alfa Aesar, Pt50, Ru50 atom %) mixed with Nafion solution was used (similar procedure and materials as for the cathode). Loading of PtRu catalyst in the reference anode was 5 mg.cm^{-2}.

Fuel cell tests – reference

The laboratory-designed miniaturized stainless steel fuel cell with 1 cm^2 active area, see Fig 2.5.2, was used for testing. To evaluate cell performance pure humidified hydrogen and air were used as fuel and oxidant under atmospheric pressure. The flow rates of H_2 and air were both controlled at 30.0 mL/min. And the fuel cell were operated at room temperature.

The obtained polarization *V–I* curves of the reference FC (made from PtRu anode) together with the power density (PD) are displayed in Fig. 3.1.4. The peak power density attained for hydrogen/air operation was 196 mW.cm^{-2} corresponding to maximum specific power (calculated as a ratio of power/catalyst loading) SP_{max} of 0.04 W per mg of precious metal (PtRu). This performance corresponds to the typical one reported for hydrogen operated PEMFC catalysed with standard PtRu and Pt/C catalysts [21].

Performance of sputtered anode catalyst

The first prototypes of FC with Pt-CeO_2 anode were prepared by depositing the catalyst film directly on GDL. The performance test was obtained at identical conditions as the test of a reference FC (Fig. 3.1.4). Maximum PD obtained for this PEMFC was 12.3 mW.cm^{-2}. Result is displayed in Fig 3.1.6, bottom panel. Pt content of the anode catalyst was 1.2 x10^{-3} mg per cm^2 of MEA, calculated from the Pt-CeO_2 film thickness (30nm) and Pt concentration of 5.2 wt.% determined by XPS and confirmed by quantitative EDX analysis in SEM. The maximum SP power was SP_{max}= 10 W/mg$_{(Pt)}$.

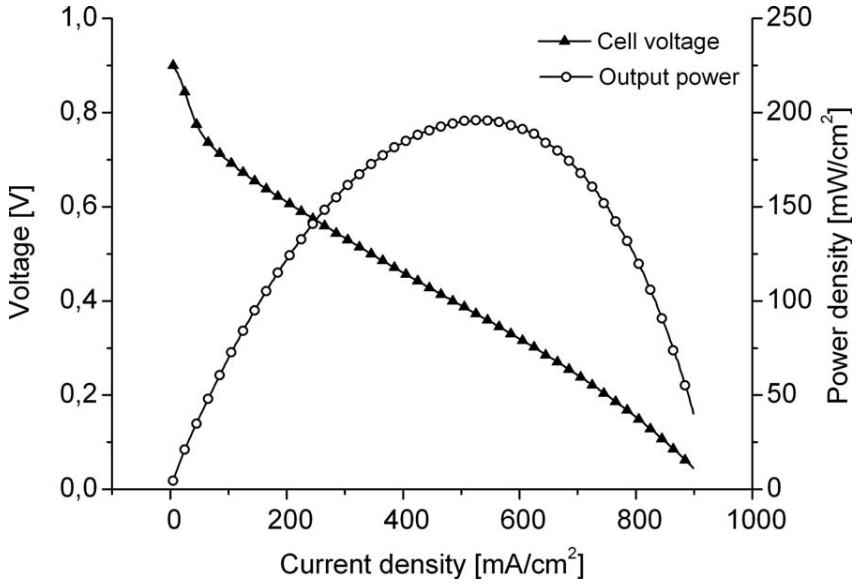

Figure 3.1.4: Polarization curve for reference FC (PtRu Anode & Pt/C cathode), H_2/air operation, room temperature, atmospheric pressure

An increased FC performance was obtained by depositing the sputtered catalyst film on an enhanced GDL by covering it with the DWCNTs. The DWCNT dispersed in water were deposited by using a spin coating method. SEM image in Fig. 3.1.5 a shows the DWCNT deposit in form of balled bunches covering the GDL. Fig. 3.1.5 b shows DWCNT substrate coated with magnetron deposited Pt-CeO_2. Figs. c and d compares detailed views of a bunch of bare carbon nanotubes and bunch of DWCNTs covered with 30nm thick sputtered Pt doped ceria film. In Fig. 3.1.5 b) one can see a typical image of the anode catalyst. A frost-like character of the deposited Pt–ceria film shows a polycrystalline character of the oxide layer with a very small size of the oxide grains.

The PEMFC performance result of anode with the DWCNT/Pt–CeO_2 anode can be seen in Fig. 3.1.6, top panel. In this case we obtained an additional increase in PD giving maximum PD = 43 mW.cm^{-2}. It corresponds to maximum SP_{max} = 35 W/mg_{Pt}. The performance test was obtained at room temperature and hydrogen and air input flow rate of 30 ml/min, i.e., at the same conditions as for the reference FC, see Fig. 3.1.4. By comparing SP_{max} for the reference FC and the cell with CNTs, we can see an increase in the performance nearly 1000 times. The PD is still five times

lower than that of the reference FC however, which shows that it is necessary to continue to search for a further increase in the anode performance.

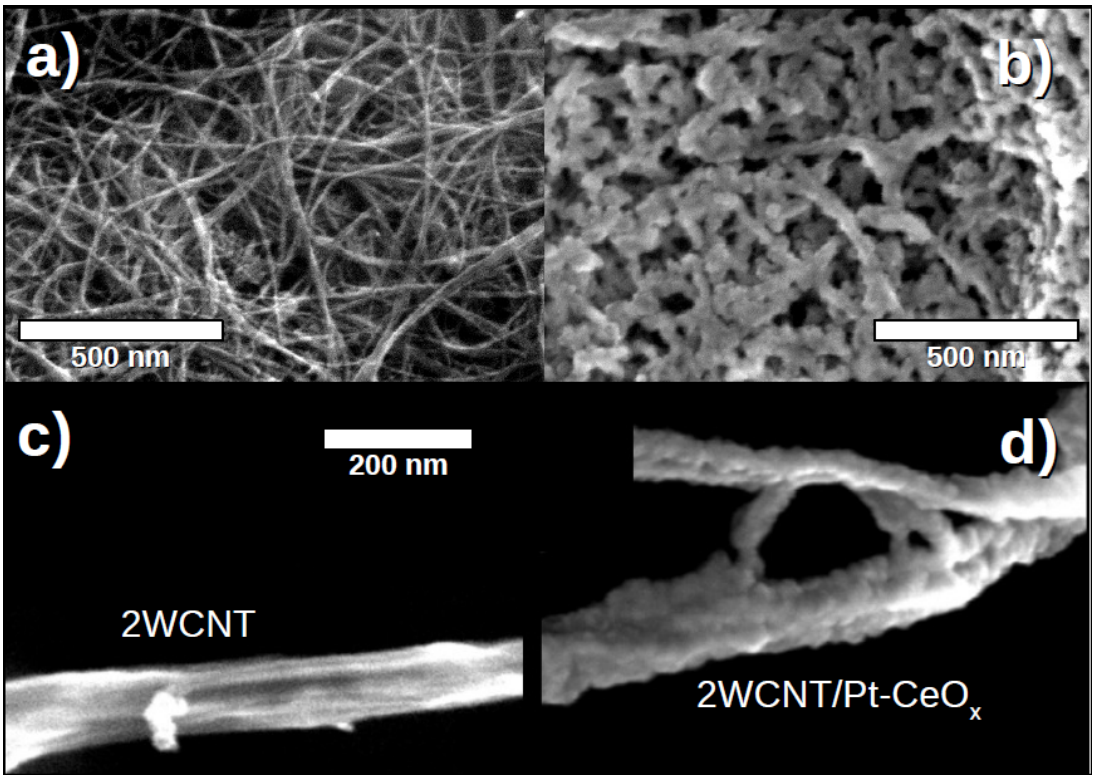

Figure 3.1.5: SEM image of bare double wall carbon nanotubes (a) and coated with sputtered Pt/CeO_x layer (b). On the panels (c) and (d) is detail of single 2WCNT, bare and coated respectively. Imaged with 30 keV primary energy. Panels c) and d) are shown by using the same magnification.

At the time there were several papers reporting on the use of pure sputtered platinum as an anode catalyst. Pt sputtered on GDL and directly on the membrane were reported. The results were rather contradictory, showing very low [65] or comparable PD [66][67].

To compare the activity of Pt–CeO_2 and pure sputtered Pt in our setup, there were two other types of MEA prepared. One with 10 nm of Pt sputtered directly on GDL and the other with 10 nm of Pt sputtered on Nafion membrane. We obtained PDs of 2.4 and 2.5 mW.cm^{-2}, respectively. These values corresponded to SPmax of

0.12 and 0.13 W/mg_{Pt}. Thus in our case Pt–CeO_2 anode catalyst revealed much higher activity than pure Pt one.

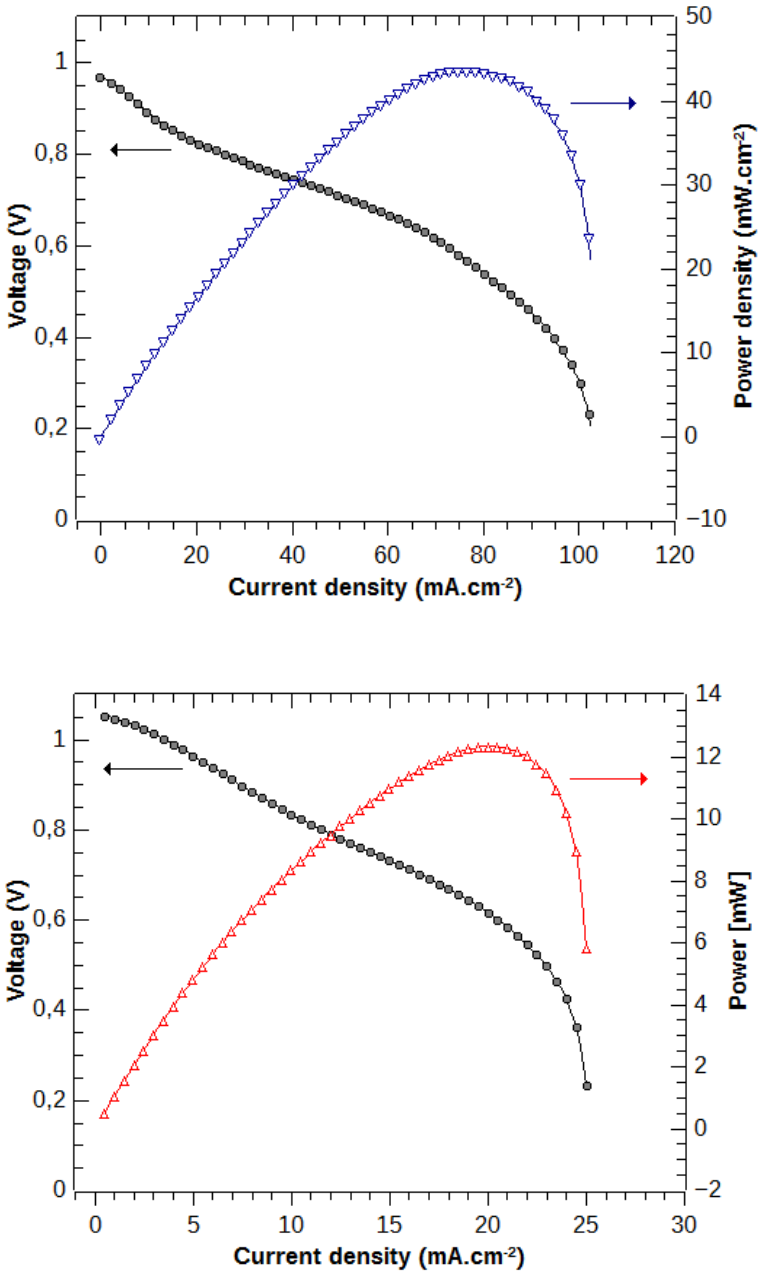

Figure 3.1.6: Top: Polarization curve of PEMFC with Pt-CeO2/DWCNT/GDL on anode. H2/air, room temperature.

Bottom: Polarization curve of PEMFC with Pt-CeO2/GDL (no carbon nanotubes) on anode. H2/air, room temperature.

This experiment published in *M. Václavů, I. Matolínová, J. Mysliveček, R. Fiala, V. Matolín, J. Electrochem. Soc., 2009, 156, B938, Copyright © The Electrochemical Society, Inc. 2009]* was a pioneering work showing for the 1st time that Pt doped CeO_2 polycrystalline film exhibit excellent properties as anode material for hydrogen PEMFC. Pt atoms embedded in the film bulk are completely ionized by forming $Pt^{2+, 4+}$ oxidic species. Cerium oxide has Ce^{4+} character with no measurable concentration of Ce^{3+} species. Quantitative evaluation of low concentration of Ce^{3+} from the XPS data is not easy, however we suppose from the investigation of the Pt-CeO_2(111) model catalyst by the resonance PES, which is showing Ce^{3+} with high sensitivity, that Pt reduces cerium oxide at Pt/CeO_2 interface.

High activity of Pt doped ceria films is given by Pt – ceria interaction. The tests of pure r.f. sputtered ceria film deposited on GDL at identical sputtering conditions showed practically no activity on anode, resulting in maximum PD = 0.41 mW.cm-2. High specific power of FC with Pt doped CeO_2 anode results probably from an enhancement of protonic hydrogen formation by Pt ions [33].
Deposition of the Pt-CeO_2 catalyst on DWCNT improved the fuel cell performance. This was due to an increase of active surface of the anode and due to excellent properties of CNT as FC electrode support [23][68].

3.2 *Pt and Sn doped sputtered CeO_2 electrodes for fuel cell applications*

In previous chapter Pt-CeO_2 oxide catalytic films have been reported as promising anode materials for PEMFC, exhibited an unusually high concentration of cationic platinum Pt^{2+} and Pt^{4+}.

Here the simultaneous magnetron sputtering of platinum, tin and cerium oxide is studied. It results in oxide layers continuously doped with Pt and Sn atoms

during the film growth. It has been reported that the addition of Sn has an important effect on the electronic structure of Pt and its adsorption and reaction properties [10][69][70][71]. It is known that Sn causes cerium oxide reduction $Ce^{4+} \rightarrow Ce^{3+}$ and the formation of a Pt-Sn-Ce mixed oxide [72]. The performance of Pt-Sn-CeO_2 catalyst on anode of PEMFC has been evaluated.

Non-reactive radio frequency (r.f.) magnetron sputtering was used to deposit CeO_2, Pt-CeO_2 and Pt-Sn-CeO_2 thin films on microporous gas diffusion layer (Alfa Aesar, Toray carbon paper, teflonated, TGP-60). The Pt-CeO_2 and Pt-Sn-CeO_2 thin films were deposited from the composite target prepared by placing pieces of 0.5 mm thick and 10 mm long Pt and Sn wires on the ceria target surface in the radial direction. Deposition was carried out at room temperature of the substrate in an Ar atmosphere by keeping the total pressure in the deposition chamber constant at 6×10^{-3} mbar.

The layer thickness was for all Pt-(Sn)-CeO_2 samples determined to be 30 nm and it was controlled by means of the SEM cross-sectional view of the broken reference Si(001) wafer sample obtained by the simultaneous deposition with samples for FC tests.

Pt and Sn concentrations in Pt-CeO_2 and Pt-Sn-CeO_2 catalyst relative to the number of Ce atoms were determined by quantitative XPS (the spectra are not shown) using Ce 3d, Sn 3d and Pt 4f peak areas and XPS sensitivity factors. The concentrations were 7 at.% of Pt for Pt-CeO_2 and 7 at.% of Pt and 8 at.% of Sn in case of Pt-Sn-CeO_2 catalyst film. The Pt concentration determined in this way corresponded to an average Pt concentration in the approximately 2 nm thick surface layer probed by XPS ($h\nu$=1486 eV). Concentration in weight percent of Pt in the anode catalyst was calculated from the Pt-CeO_2 film thickness (30 nm) and Pt atomic concentration, and gave values of 2.2×10^{-3} mg of Pt per cm^2 of the anode.

Fuel cell performance

Fuel cell tests were performed by using a miniaturized polymer membrane fuel cell device with 1cm^2 active area at room temperature (described in previous chapter). The cathode electrodes were made by carbon-supported Pt powder (Alfa Aesar, Platinum, nominally 40% on carbon black) mixed with the Nafion solution (Alfa Aesar, Perfluorosulfonic acid-PTFE copolymer, 5% w/w solution) and coated

on the microporous GDL. The loading of Pt in the cathode catalyst layer was 5 mg/cm^2.

The anode GDL was coated with then 30 nm thick Pt and Pt-Sn doped sputtered films. The pretreated Nafion membrane was sandwiched by the catalysed anode and cathode by hot-pressing to form MEA (10×10 mm^2).

The FC measurement were done using pure humidified hydrogen and air as oxidant at atmospheric pressure. The flow rates of H_2 and air were controlled at fixed value of 30.0 ml/min. The performance of the fuel cell with sputtered anode was compared with that of the reference FC. The reference FC differed from the tested one by the anode preparation only. The reference FC anode was made similarly as in previous chapter, by using standard Pt-Ru powder catalysts with a loading of 5mg/cm^2.

Performance of the miniaturized PEMFC prepared by catalysing the anode GDL with the above described r.f. sputtered Pt-CeO_2 and Pt-Sn-CeO_2 catalyst is shown in Figs. 3.2.1 a) and b), respectively.

The Pt-CeO_2 anode gave a measured power density of 4.9 mW.cm^{-2} while the Pt-Sn-CeO_2 catalyst revealed an increase to 10.5 mW.cm^{-2}. Notably that the power density was relatively low because of the deposition of the catalysts films on GDL which reveals very low specific surface, nevertheless the purpose of this experiment was to compare the relative performance of Pt ceria catalysts doped with Sn and without added Sn. Known concentration of Pt made it possible to calculate maximum specific power SP_{max} for the both catalysts.

For Pt-CeO_2 and Pt-Sn-CeO_2 films, we found SP_{max}= 2.5 and 5.4 W/mg(Pt), respectively. In comparison with the SP_{max} value obtained for the standard Pt-Ru anode (SP_{max} = 0.04 W/mg$_{(Pt)}$ [73], both sputtered catalysts exhibited very high activity per unit Pt content. The Sn doped Pt-CeO_2 catalyst exhibited higher performance than the undoped one suggesting enhancing role of the Sn on the activity of the catalyst.

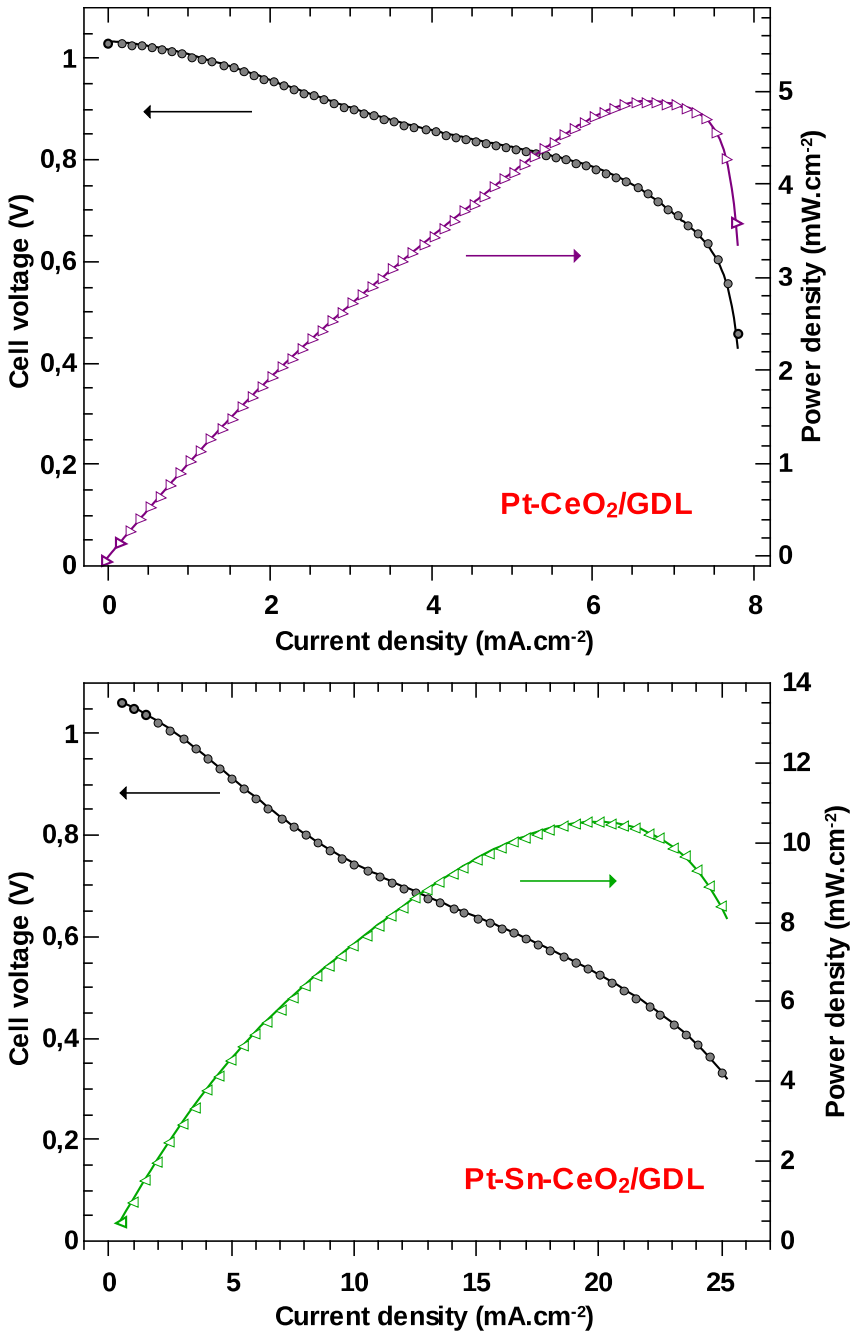

Figure 3.2.1: Polarization and power density vs. current density using hydrogen/air flow at room temperature. FC with (a) Pt-CeO_2 anode, (b) Pt-Sn-CeO_2 anode

Photoelectron spectroscopy

The photoemission spectroscopy of Si supported reference samples was performed with X-rays of three different energies in order to vary the kinetic energy of the photoelectrons, and therefore the probing depth. We refer here to the lowest energy as soft X-ray photoelectron spectroscopy (SX-PES). These measurements were performed in an ultrahigh vacuum chamber of the experimental system at the Materials Science Beamline (MSB) at the Elettra synchrotron light source in Trieste ($h\nu$ = 180 eV, ΔE = 200 meV). The highest energy photoemission spectra referred as hard x-ray photoelectron spectroscopy (HX-PES) were performed at BL15XU beamline of the SPring8 synchrotron facility [74]. The total energy resolution ΔE = 280 meV was determined from the Fermi edge of an Au reference sample. Medium energy photoelectron spectra were measured using an Al X-ray source ($h\nu$ = 1486.6 eV, ΔE = 1 eV) and we refer to these data simply as XPS results. All PES experiments were performed ex situ in ultra-high vacuum (UHV) experimental chambers operating at base pressures < 10-10 mbar. The SX and HX-PES spectra were taken at normal emission, while XPS was measured at two photoelectron emission angles 20° and 60° with respect to the surface normal, in order to change surface sensitivity.

The high resolution 3d core level HX-PES (5946.8 eV) spectrum of the CeO_2 film deposited on Si(001) without adding Pt is presented in Fig. 3.2.2 (bottom curve). It consists of three $3d_{3/2}$-$3d_{5/2}$ spin-orbit-split doublets characteristic of stoichiometric CeO_2 (Ce^{4+}). The doublets represent different 4f configurations in the photoemission final state and arise from the Ce 4f hybridization in both the initial and the final states. The middle curve in Fig. 3.2.2 shows a HX-PES Ce 3d spectrum obtained for Pt doped films. The spectra of CeO_2 and Pt-CeO_2 films are practically identical, showing that there is no measurable influence of added platinum on the cerium oxide stoichiometry.

The Pt 4f PES spectra obtained for the Pt doped ceria films are plotted in Fig. 3.2.3 (left panel). Spectra at different photon energies have different information depth. For HX-PES the kinetic energy of the Pt 4f electrons is about 5870 eV

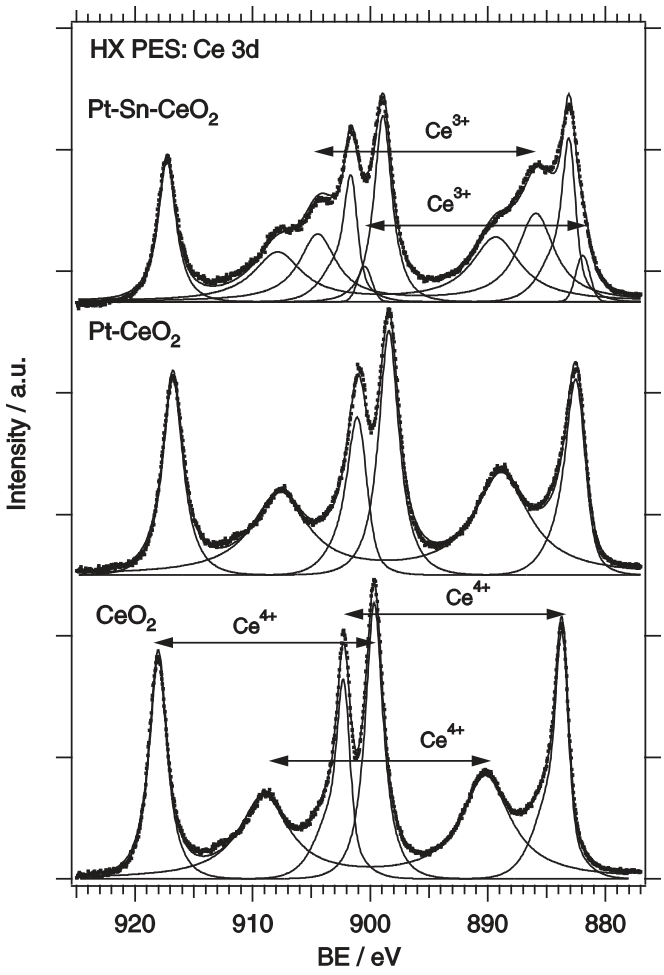

Figure 3.2.2: Ce 3d HX-PES spectra (hν= 5946.8 eV) of the r.f. magnetron sputtered films. Bottom spectrum was measured on pure cerium oxide film, upper spectra on Pt and Pt-Sn doped samples

corresponding to an inelastic mean free path in CeO_2 of $\lambda = 7$ nm [75]. For $h\nu = 180$ eV, the kinetic energy of the Pt 4f photoelectrons is close to 110 eV, corresponding to λ of 0.5 nm.

The spectrum at $h\nu = 180$ eV with the highest surface sensitivity exhibits a Pt $4f_{5/2}$ – $4f_{7/2}$ doublet at 72.9 eV corresponding to Pt^{2+} [8] and a doublet shifted by 1.4 eV to higher binding energy (BE) corresponding to Pt^{4+} [10]. A small peak at 71.8 eV is assigned to the Pt^0 state. This energy is slightly higher than that expected for metallic platinum. This shift can be explained, however, by a size effect in PES, which is generally observed for very small particles (below 2 nm). The ratio of the

Pt^0 peak area relative to the whole Pt signal $Pt^0/Pt = 0.035$. The Fig. 3.2.3 clearly shows that with increasing hν, the relative intensity of Pt^{4+} increases.

The upper curve in Fig. 3.2.3 (left panel) shows the Pt 4f HX-PES spectrum obtained for the Pt doped ceria film, i.e. the spectrum measured at highest information depth. The spectrum exhibits Pt $4f_{7/5} - 4f_{5/2}$ doublets corresponding to Pt^{4+} and Pt^{2+} states only. Contribution of Pt^0 is negligible, which indicates that platinum atoms in the ceria layer are fully oxidized. The Pt 4f spectrum obtained by HX-PES reveals a platinum ion concentration ratio of $Pt^{4+}/Pt^{2+} = 1.45$.

The XPS Pt 4f spectra, middle and bottom, also show high intensity of the Pt^{2+} and Pt^{4+} with negligible Pt^0 signal. In order to change the surface sensitivity of XPS we measured the photoelectron emission for different angles of outgoing electrons relative to the surface normal. In Fig. 3.2.3 we compare spectra taken at 60° (λ = 1 nm) and 20° (λ = 2 nm) [75]. Pt 4f XPS spectra obtained for a photoelectron escape

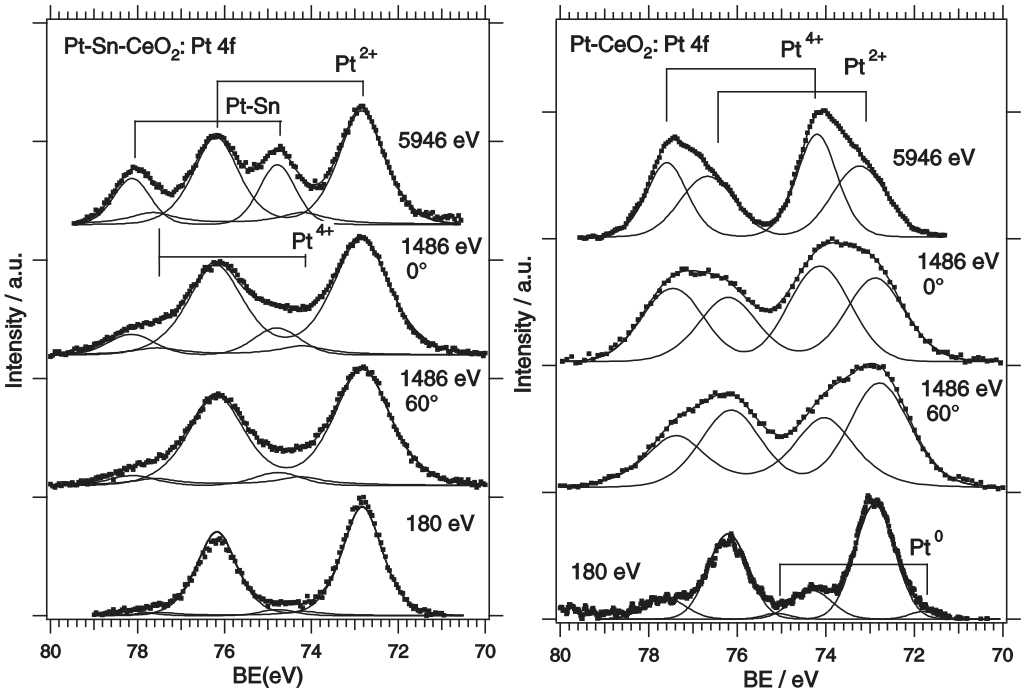

Figure 3.2.3: The SX-PES, XPS at photoemission angle of 20° and 60°, and HX-PES Pt 4f spectra of the Pt-CeO_2 film (left panel) and Pt-Sn-CeO_2 film (right panel).

angle of 60° (higher surface sensitivity) and 20° (lower surface sensitivity) show Pt^{4+}/Pt^{2+} ratios of 0.77 and 1.06, respectively, i.e. angle resolved XPS confirms a substantial increase of the Pt^{4+} signal with decreasing surface sensitivity.

Photon energy/ emission angle	Pt^{4+}/Pt^{2+}	$Pt(Sn)/Pt^{2+}$
180 eV/ 0°	0.24	0.12
1487 eV/ 60°	0.77	0.15
1487 eV/ 20°	1.06	0.26
5946 eV / 0°	1.45	0.6

Table 3.2.1: The relative concentration of of Pt^{4+}, Pt(Sn) and Pt^{2+} content determined with different surface sensitivity using Pt 4f peak area

A simple estimation based on the enhancement of the Pt^{4+} signal as a function of λ leads to a structural model with Pt^{4+} dispersed in the ceria film bulk, Pt^{2+} rich Pt-ceria interface and surface region, and very low concentration of metallic platinum on the surface.

Fig.3.2.3 (right panel) shows Pt 4f spectra of the ceria layer simultaneously doped with Pt and Sn during the film growth. The upper spectrum was obtained for HX-PES at hν = 5946 eV. We fitted the spectrum with two doublets, with the most intense peak corresponding to Pt^{2+}. The Pt^{4+} intensity observed in Fig.3.2.3 (left panel) at 74.3 eV vanished whilst a new state appeared at Pt $4f_{7/2}$ = 74.8 eV, indicating the formation of a new chemical state of Pt. The corresponding HX-PES Ce 3d spectrum in Fig. 3.2.2 (upper curve) clearly indicates that tin induces a partial reduction of ceria which can be seen as appearance of the Ce^{3+} states in the film bulk. We calculated the Ce^{3+}/Ce^{4+} concentration ratio as the ratio of the sums of areas of the corresponding fits in Fig. 4, and obtained a value of Ce^{3+}/Ce^{4+} = 0.28, showing that approximately 25% of Ce atoms are in the Ce^{3+} state. The partial reduction of cerium oxide by tin is in agreement with previous results [76] showing a strong Sn-CeO_2(111) interaction leading to the $Ce^{4+} \rightarrow Ce^{3+}$ transition [77].

The BE of the Sn $3d_{5/2}$ state of 486.7 eV corresponds to Sn^{4+} (spectra not shown, can be found in original paper [35]).

The BE of Pt $4f_{7/2}$ in a Pt-Sn alloy is close to 71 eV [69][70], i.e. it has a relatively small shift relative to metallic Pt. The high binding energy of Pt $4f_{7/2}$ observed in our case together with a Sn $3d_{5/2}$ BE typical for SnO_2 leads to the conclusion that the new

Pt phase in the Pt-Sn-ceria film might correspond to a binary Pt-Sn and/or ternary Pt-Sn-Ce mixed species, probably highly dispersed in the catalyst film.

Similarly to the case of the Pt-CeO_2/Si sample we changed the information depth of the analysis by taking spectra at different photon energies and different electron emission angle. The results in Fig. 3.2.3 (right panel) show a decrease of the Pt-Sn phase (74.8 eV) concentration relative to Pt^{2+} with increasing surface sensitivity.

Sn has an important chemical effect on the electronic structure of Pt, and in particular induces changes in the d-band occupation due to d–sp orbital hybridization, Pt → Sn charge transfer and an increase of the Pt 5d hole number [69]. Pt → Sn charge transfer is in agreement with the observed high binding energy of the new platinum state. An increase of the Pt 5d hole number could tentatively explain the observed high activity of the Pt-Sn-CeO_2 anode in the hydrogen PEMFC due to an increase of the probability of $H \rightarrow H^+ + e^-$ splitting.

3.3 Pt-CeO_2 thin films sputtered on nanoGDL

The studies reported in previous chapters were focused on preparation of thin cerium oxide films by r.f. magnetron sputtering on bare and/or CNT coated GDL substrate. The results revealed very high specific power due to low Pt loading, however the disadvantage of these systems was still a low power density which would make such catalyst uncompetitive if used in real PEMFC system. It was found that this low activity was due to relatively bad technical quality of the small single fuel cell and simple testing station we used for performance study on one side, and also due to still rather low catalyst active surface in case of CNTs on other side. Therefore in the experiment we replaced the home-made small cell by a commercial pneumatically operated one provided by Greenlight Innovation company (Greenlight TP-5 Research Cell), see Experimental part, chapter 2.5.

Our studies showed that using carbon support the structure and morphology of the deposited layers depended on the oxygen concentration in working gas during magnetron sputtering used for cerium oxide deposition. It was reported in [78] that ceria deposition is accompanied by a considerable erosion of the carbonaceous sub-

strate and by formation of highly porous carbon/cerium oxide interface. Etching of the carbon interlayer with oxygen species occurring simultaneously with cerium oxide film growth is considered to be the driving force for this effect resulting in the formation of nanostructured cerium oxide films with large surface.

By a rigorous tuning of the deposition parameters and by selecting a new type of a catalyst support, in this case so called “nGDL” or “nanoGDL” (SGL TECHNOLOGIES GmbH, Sigracet GDL 25 BC), it was possible to increase the sputtered catalyst power density to the desired range, comparable with that of standard commercial catalysts. In Fig. 3.3.1 the structure of bare GDL (a) and of the nanoGDL (b) is shown. It can be seen that nanoGDL surface is coated by a layer of carbon NPs with particle average size of 50 nm. Zoom on Pt-ceria coated nanoGDL in Fig. 3.3.1 (c) reveals fine cauliflower like porous structure.

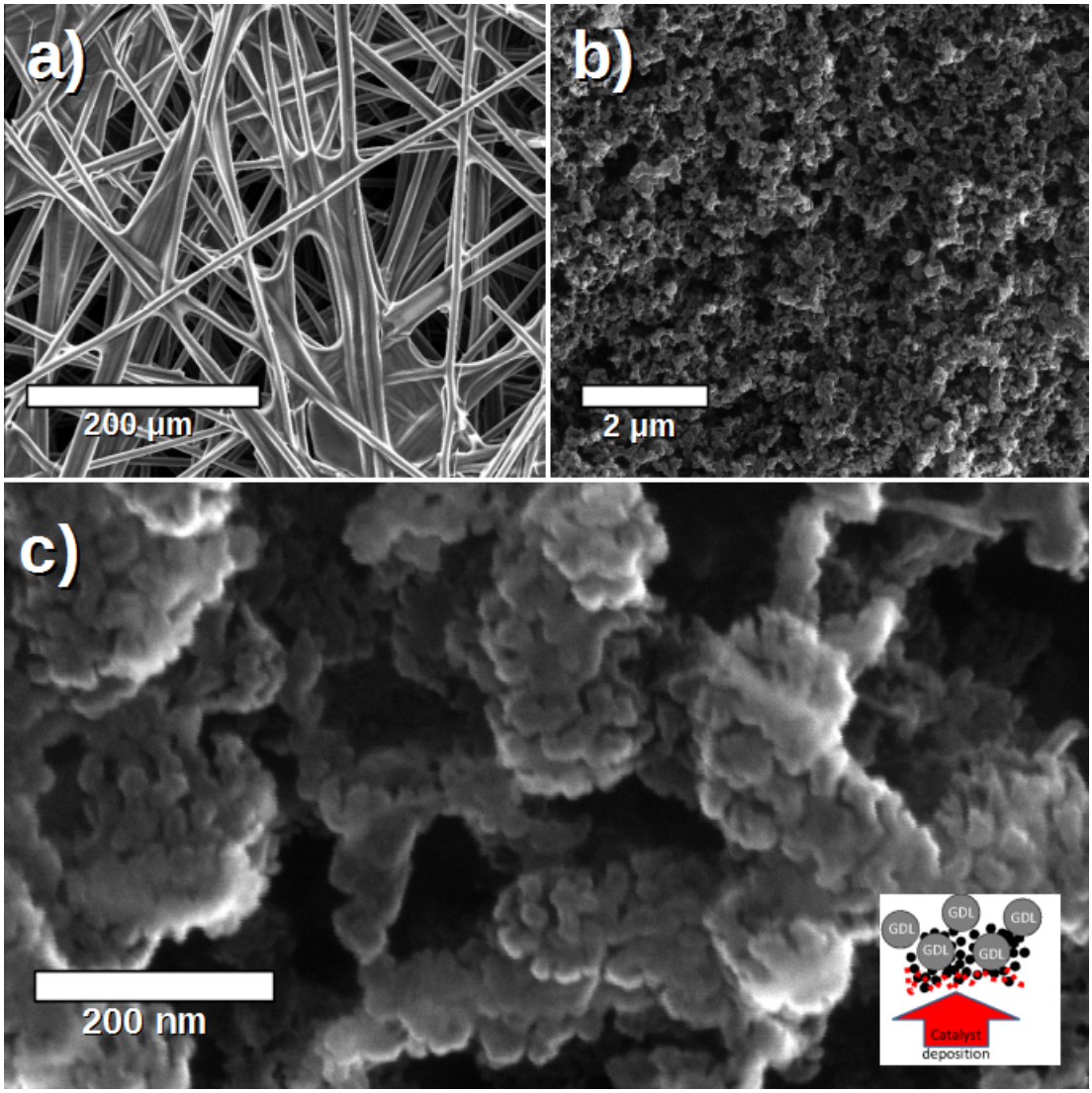

Figure 3.3.1: SEM image of bare GDL (a) GDL with microporous layer of carbon nanoparticles - nGDL (b) and detail of nGDL coated by Pt-CeO_2 catalytic layer (c)

Scanning transmission electron microscopy cross view of one catalyst coated carbon nanoparticle shows that porous structure is due to etching of nano channels inside the particle which are coated with the catalyst film, see Fig. 3.3.2. The sample was prepared using cutting by focus ion beam (FIB) technique.

In this case the FC tests were performed by using actually much improved testing station and with using commercial fast exchange cell holder with graphite plates, the cell being pneumatically compressed using 800 kPa piston pressure. The active area of MEA is in this case 4.6 cm^2. MEA was assembled from the 0.05 mm thick Nafion membranes (DuPont Inc., Nafion NR-212, perfluorosulfonic acid-PTFE

copolymer), which was sandwiched by the catalyzed anode and commercial cathode catalyst. No hot-pressing were done and also no pretreatment of the Nafion was carried out, since this recasted form can be used directly.

The anode electrode was fabricated from the commercial nGDL support which was coated by 30 nm thick Pt–CeO_x layer by reactive r.f. magnetron sputtering. The cathode electrode was commercially available GDL supported Pt catalyst (Alfa Aesar, No.45368, loading of Pt is 2 mg/cm^2). The cell was operated with pure humidified hydrogen as fuel and oxygen as oxidant under atmospheric pressure. The flow rates of H_2 and O_2 were controlled at 40 ml.min^{-1} and 30 ml.min^{-1} respectively. Temperature of the cell as well as both humidifiers was controlled at 65 °C.

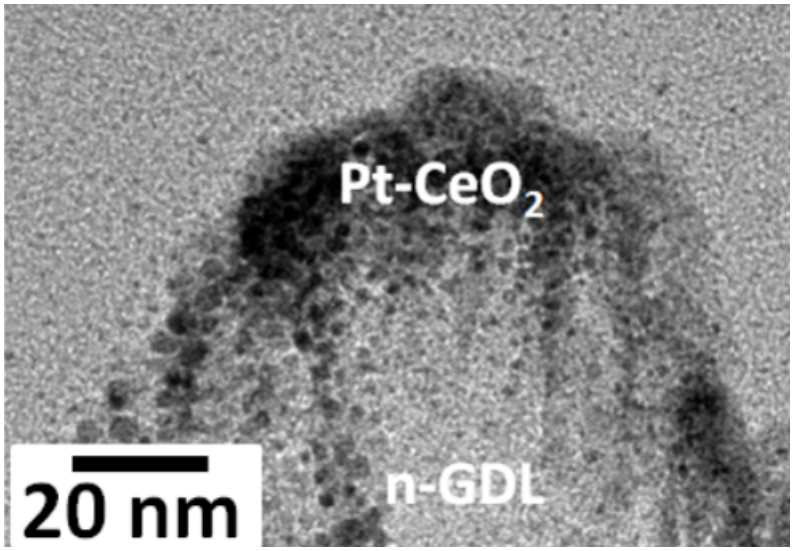

Figure 3.3.2: TEM image of a lamella made from sputtered Pt-CeO_2 catalyst layer deposited onto nGDL substrate. Detail of single carbon particle coated by the catalyst. Porous structure due to etching is shown.

The performance of the Pt doped cerium oxide anode was compared with a reference anode tested at same conditions. For the anode in reference MEA a commercially available Pt–Ru catalysed GDL (Alfa Aesar, No. 45367) was used. The PGM loading on this anode product was according to the supplier nominally 2.7 mg Pt/cm^2 and 1.25 mg Ru/cm^2.

The polarization curves obtained for both the reference and containing Pt-CeO2 anode MEA is shown in Fig. 3.3.3. It can be seen that at the selected temperature the maximum power density obtained was PD_{max}= 0.41 W cm^{-2}. This value corresponded to specific power of SP_{max} = 103 W $mg^{-1}_{(Pt)}$ for Pt loading of 4 µg.cm^{-2}.

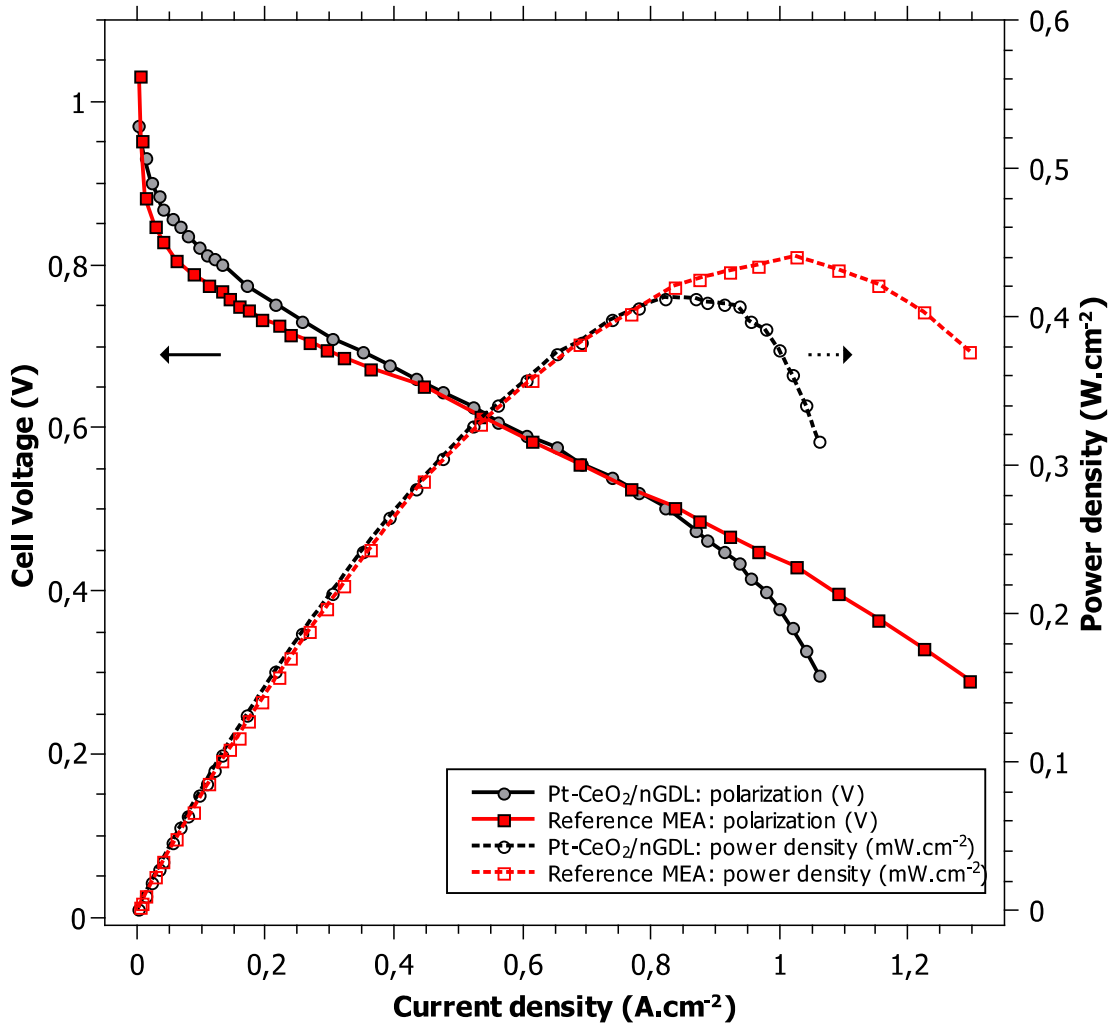

Figure 3.3.3: Polarization curve of sputtered Pt-CeOx supported on nGDL substrate and comparison with commercial reference. Adapted from [83] Copyright © 2015 Elsevier

By using Electrochemical Impedance Spectroscopy we determined the cell resistance as high frequency resistance to be typically about 140 mΩ.cm^{-2}, by using Linear Sweep Voltammetry on cell operated with nitrogen/hydrogen with scan rate of

0.5 mV/s the crossover current was 2 $mA.cm^{-2}$ as the limiting current at potential of 0.220 V.

In Fig. 3.3.3 one can see also the results of the reference FC measured at the same conditions using the same cathode catalyst and by replacing the Pt–CeO_x/nGDL by the standard commercial Pt–Ru catalysed GDL. It can be seen that in spite of 1.4 times higher PD_{max} in case of the reference MEA, the specific power obtained for Pt–CeO_x anode was very high due to very low Pt loading. Considering loading of precious metals (PM) in the reference catalyst 2.7 mg of Pt/cm2(giving PD_{max}= 0.1 W mg^{-1}(Pt)) we can see that SP_{max} of the sputtered catalyst film was more than by 2 orders of magnitude higher relative to the reference catalyst case. It shows that nano-carbon supported Pt–CeO_2 thin film catalysts exhibit unprecedentedly high activity.

Although a complete long time endurance test was not performed, after a more than one day continuous operation the FC did not show any noticeable decrease of the activity.

By comparing with our previous results obtained for similar Pt–ceria films deposited on CNTs [79] (PD_{max} = 74 $mW.cm^{-2}$ at 75◦C), in the case of the nGDL support we obtained the anode performance which was well comparable with that of the commercial catalysts. It should also be noted that this result is important from practical point of view because nGDL is much more easily available (commercially) while CNTs must be grown on GDL by using a chemical vapour deposition (CVD) method.

In order to compare the activity of the Pt doped cerium oxide catalyst with that of pure Pt there was a reference catalyst prepared by sputtering deposition consisting of 4 μg of pure Pt directly deposited onto the nGDL. In the FC test there was obtained PD_{max} = 0.1 W cm^{-2} i.e. about 4 times lower value relative to that of the Pt–CeO_x anode.

Summary

If the result from nGDL substrate is compared with results from chapter 3, where the sputtered Pt-CeO_2 catalyst was deposited either directly on the microporous GDL or onto dispersed DWCNTs on GDL,

4 Stability and interaction of Pt-CeOx catalytic layers with hydrogen and water

In the harsh environment of PEMFC electrodes, where the electrochemical reactions takes place at the interface of solid electrolyte and catalyst, in the presence of varying potentials and exposition to reactants and elevated temperature, the catalyst are inevitably being influenced and may undergo changes including morphology, chemical composition and structure.

Studying these changes in operando is quite hard task which cannot be done without special instrumental equipment. To at least partially understand possible effects of the anode environment on the anode catalyst presented in previous chapter, the following experiment was conducted.

Catalytic layers of similar composition and thickness of that used inside FC MEA were deposited on Graphite foil (C-foil). The C-foil was chosen as suitable carbon substrate, because it is similar to carbon particles, which are typically used as support in fuel cell electrodes. Moreover it has good conductivity and is easy to handle. Theses samples were exposed to hydrogen and water vapour at atmospheric pressure at temperatures typical for PEMFC operation. After this ex-situ treatment, the samples were then analysed using SEM and XPS methods.

In parallel to this experiment there was also an UHV study conducted, using identical samples, but studying the interaction effects in-situ using SRPES and XPS.

One of key questions might be: what the stability of the catalyst in these conditions is and what happens to platinum in ionic state?

4.1 UHV experiment

The objective of the experiment was to investigate hydrogen and/or water interaction with the Pt-CeO_x mixed oxide catalytic layers on C-foil substrate and the

effects of temperature treatment. The experimental steps were chosen in such a way that after every sample temperature treatment followed an exposition of the sample to hydrogen and water. After each major step the state of the sample was documented using series of measurement by PES.

This experiment was done in experimental chamber of Material Science Beamline at Elettra Sincrotrone Trieste. Details about this experimental installation and parameters can be found in chapter 2. Main reason to use tunable synchrotron radiation is the possibility to get highest surface surface sensitivity for selected element and second the possibility to use RPES method, which can be used in this case to evaluate oxidation state of ceria with high resolution and surface sensitivity.

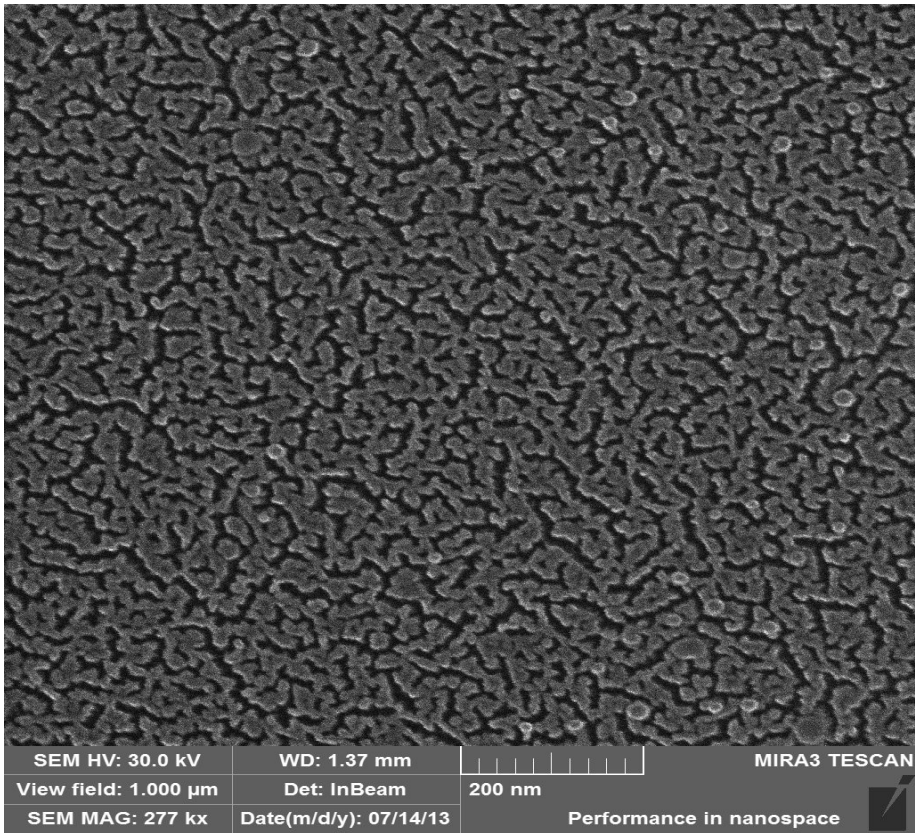

Figure 4.1.1: SEM image of typical morphology of sputtered Pt-CeOx layer on C-foil

All samples were deposited onto C-foil substrate (Alfa Aesar) using reactive magnetron sputtering from composite target made from 51 mm diameter CeO_2 target

(Kurt Lesker) on which one (lower platinum content) or two pieces (higher content) of platinum wire (0.5 mm diameter, Alfa Aesar) were placed radially, details in chapter 2. Sputtering was done using working gas composed of mixture of Ar (5.0 quality) with added 0,25% of O_2 at pressure of about 0.4 Pa and 30W r.f. power. Typical deposition rate was about 0.8 $nm.min^{-1}$.

Typical morphology of the prepared samples is displayed on SEM image in Fig. 4.1.1. It can be seen that the sputtering deposition process creates rather porous surface structure. This phenomenon is specific for case when carbon substrate is used in combination with reactive sputtering deposition and has been thoroughly described for the ceria sputtered films in [78]. As was already mentioned earlier, during deposition the plasma containing oxygen ions and radicals reacts with the carbon support causing partial etching of carbon. During the deposition the incoming material is masking the substrate surface and combination of these processes sustains the porous growth by achieving larger active surface area of catalytic layers. Controlling of the etching process can be done by dosing trace amount of oxygen into the working gas.

Three type of samples were studied. All were prepared ex-situ and then transported to the experimental apparatus over atmospheric conditions. First type of sample is sputtered Pt-CeOx mixed oxide with relatively small Pt content, which will labelled as “Pt-CeOx Low/C-foil” or “Low-Pt”, second sample with higher content of platinum is labelled “Pt-CeOx High/C-foil” or “High-Pt”, and lastly also pure sputtered CeO_2/C-foil sample was studied (table 4.1.1). All samples were deposited onto C-foil substrate, thickness of all samples was selected to about 25nm. It could be possible to calculate mass of Pt inside the layers, but then an assumption on the layer density and/or structure would have to be made, so here it was chosen to stay with the atomic Pt/Ce fraction as directly determined by XPS (details are described in chapter 2).

The thickness of the samples were determined from calibration of sputtering rate, which has been done using an AFM instrument by measuring height difference on edge created by peeling off masked part of reference sample. The masking were done by coating a drop of nail varnish onto silicon wafer sample.

sample	equiv. thickness	Pt/Ce ratio (XPS)
Pt-CeO_x high/ C-foil	25nm	0,16
Pt-CeO_x low / C-foil	26nm	0,03
CeO_x/ C-foil	20 nm	---

Table 4.1.1: Composition and thickness of samples used in UHV study of interaction with hydrogen and water.

Similarly to catalytic layers presented in chapter 3 the sputtered layers of mixed ceria doped with platinum contains high amount of platinum in ionic state (either 4+ or 2+), this is observed in both cases of platinum concentration. The as received samples exhibit at least two different components in the Pt 4f spectra. (For High-Pt sample Fig. 4.1.2 and for Low-Pt sample Fig. 4.1.3 respectively). One spin-orbit doublet can be found at about 72.8 eV (Pt $4f_{7/2}$) and this can be associated with Pt^{2+} state, most likely in the form of Pt-O_4 planar moiety [80].

The second spin-orbit doublet can be found at about 74.5 eV which corresponds to the Pt^{4+} state. This state belongs probably to platinum atoms trapped in substitutional positions inside the ceria matrix [73].

There is no detectable amount of metallic platinum in either samples in as received state (with surface sensitive PES measurement).

From Ce 3d spectra it is evident, that the sample with High-Pt content is more reduced in the as received state than the low Pt content sample, as can clearly be seen (even without fitting) from the shape of the Ce 3d spectra at around 886 eV (Fig. 4.1.2). The degree of reduction observable from Ce 3d spectra well matches value determined by RPES from Ce resonance data. The RER numbers representing concentration of Ce^{3+} species for Low-Pt and High-Pt samples are presented in Fig. 4.1.5, top panel.

O 1s spectra shows to separated peaks, first one at lower BE can be assigned to lattice oxygen in CeO_x, which can generally be a combination of $O_{lattice}(Ce^{4+})$ in stoichiometric ceria and lattice oxygen in reduced ceria $O_{lattice}(Ce^{3+})$. Position $O_{lattice}$ determined from XPS measurement was 529.5 eV in case of low-Pt sample and 529.9 eV in case of high-Pt sample (corresponding to Ce 3d $f^0_{3/2}$ component placed at 916.8 eV). This would correspond to lower and higher reduced ceria, when compared

to model systems in [83]. The second peak is very likely composed of more contributing components, mainly chemisorbed water and hydroxyl groups, including special species of OH connected to Ce^{3+} vacancies. There is also a contribution from adventitious carbon species. It was concluded, that it is not possible to reliably decompose the peaks into separate components and therefore the peaks are taken as unresolved components consisting of more species.

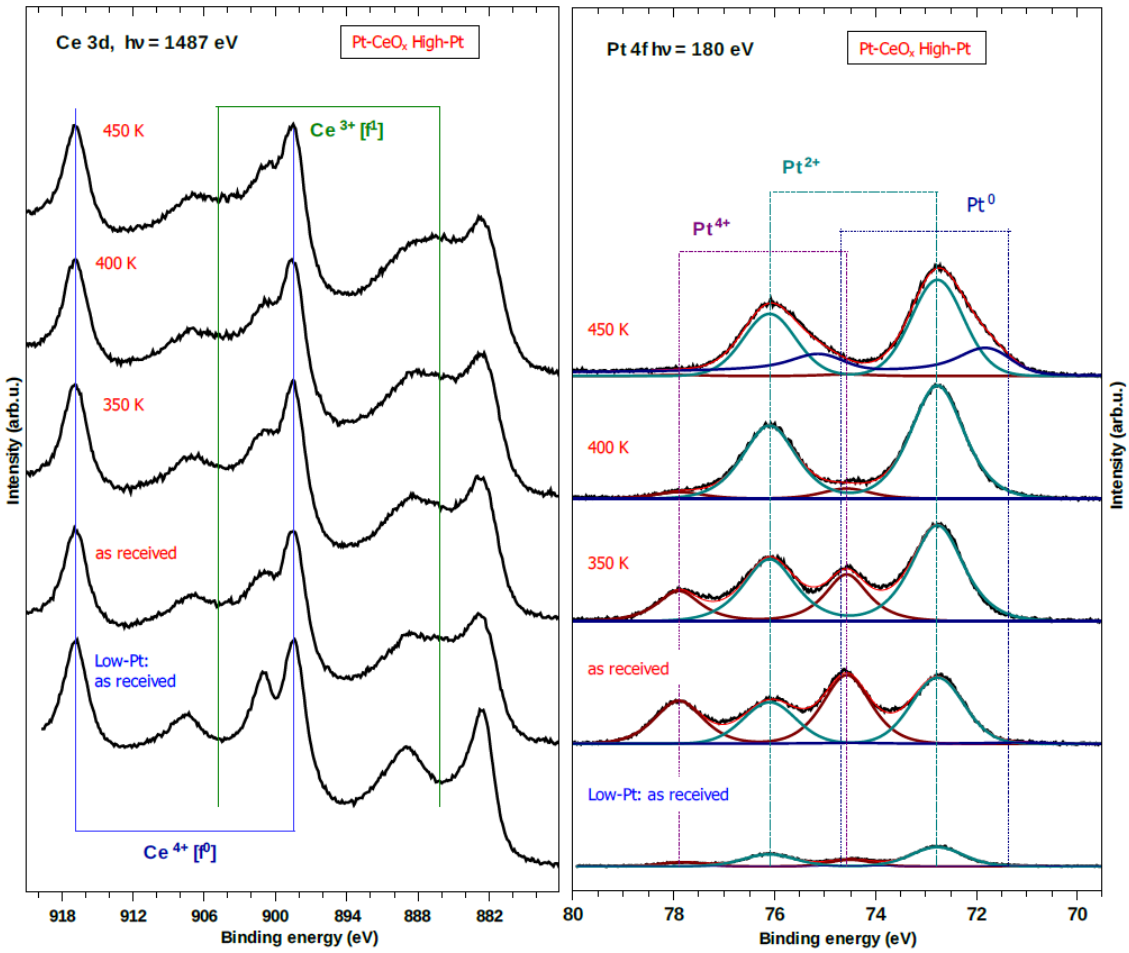

Figure 4.1.2: Sample Pt-CeO_x High-Pt / C-foil: XPS Ce 3d and SRPES Pt 4f spectra after different annealing temperatures and comparison with corresponding spectra for Pt-CeO_x Low-Pt/ C-foil sample (only in as received state)

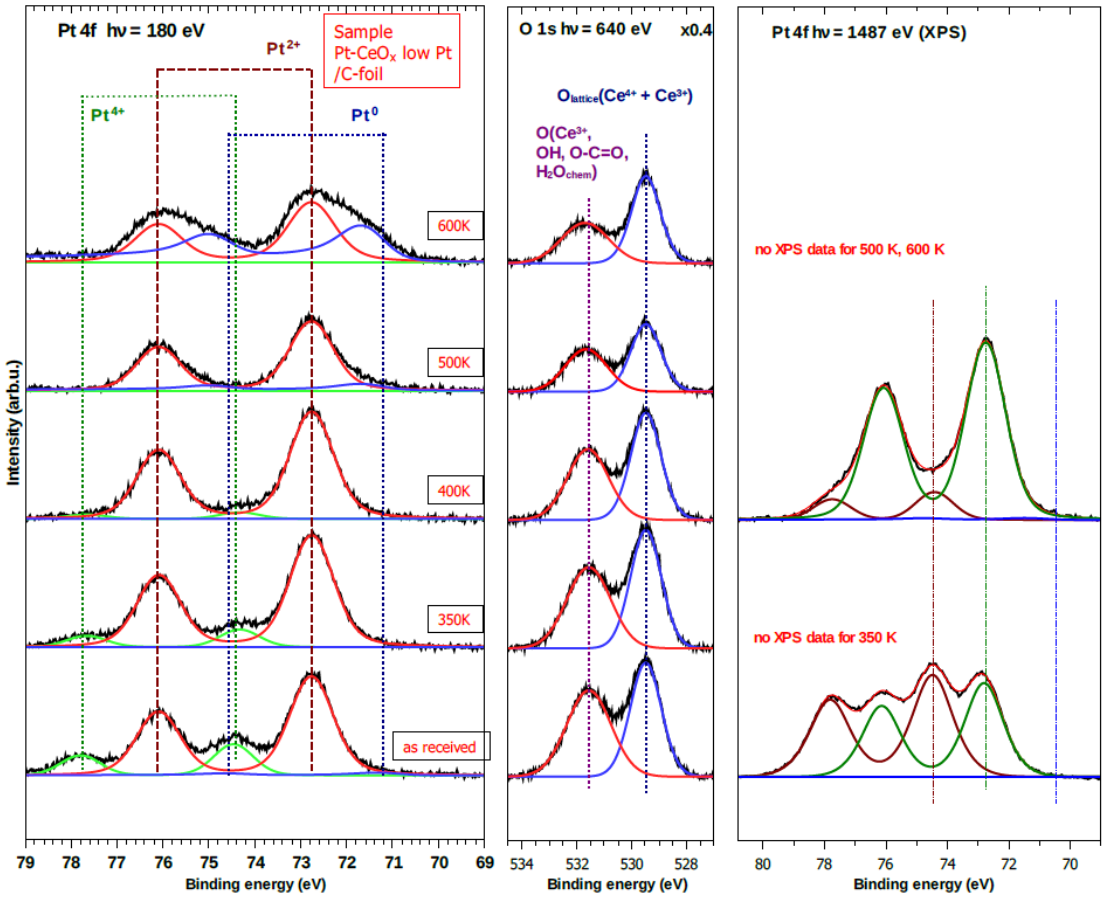

Figure 4.1.3: Sample Pt-CeO_x Low-Pt / C-foil: SRPES Pt 4f and O 1s and comparison with XPS Pt 4f spectra (measured only for selected steps) after different annealing temperatures

Effects of annealing on platinum in ceria layers

The most prominent changes observed during the UHV experiment are temperature induced reduction of cerium and platinum. This is illustrated in Fig. 4.1.2 on the High-Pt sample, for comparison there is also spectrum for as received state of Low-Pt sample.

During the sequential annealing the Pt^{4+} state transforms to Pt^{2+} state. At 450K there is almost no Pt^{4+} left at surface in case of High-Pt sample. Probably because there is not enough capacity of the surface to stabilize all the platinum in ionic form, part of the platinum is transformed to metallic platinum. Also the amount of Ce^{3+} is slightly increasing with higher annealing temperature. In case of Low-Pt state, this

cannot be confirmed, as the 450K step was skipped for this sample, but similar process is detectable after 500 K annealing and to obtain similar condition, annealing higher than 500 K is needed..

Changes of Pt species content with different surface sensitivity are demonstrated on sample Low-Pt, comparing as received state and state after annealing to 400K. In the as received state, there is practically no metallic component in Pt4f spectrum present as determined using very surface sensitive SRPES Analysis by XPS with more depth information also shows no metallic platinum (Fig. 4.1.4). However the ratio between Pt^{2+} and Pt^{4+} is differs based on surface sensitivity, XPS shows more of the 4+ state present. This is in accordance with previous results, showing that the platinum near surface is mostly in 2+ state whilst in depth, the 4+ component prevails.

After heating to 400 K, it can be seen that practically all Pt^{4+} state disappears and only Pt^{2+} state remains with surface sensitive SRPES. XPS confirms the trend of the change, but still some amount of Pt^{4+} (about 10% compared to 50% in "as received" state) is detectable with the longer IMFP coming from use of Al Kα X-ray source (Fig. 4.1.4).

The transformation of Pt^{4+} as seen by XPS is completed after repeated annealing at 400K (not shown). This can be caused by the relatively thick layer of material and porous structure of sample, also transformation of Pt is happening mostly in the surface region. Reduction in bigger depths then follows and possibly it might be combined with diffusion of Pt.

The information depth can be roughly estimated by taking IMFP of photoelectrons travelling inside CeO_2 matrix (this is very likely not entirely true, but should by sufficient). According to [61] this would yield for XPS (E_k ~ 1400 eV) λ ~ 2,2 nm and in case of SRPES (E_k ~ 105 eV) λ ~ 0,5 nm.

It can be seen that XPS generally shows higher relative content of Pt in 4+ state compared to surface sensitive measurement with low primary energy. After heating to 400K there is only Pt^{2+} left the surface as determined by SRPES, however XPS still shows some remaining Pt^{4+}.

At 400 K measured by SRPES there is only Pt^{2+} present in the Low-Pt sample. Only when annealed above 400 K there appears some metallic component. After 600 K the metallic component becomes relatively large.

It should be noted that after annealing in case of both samples (after 450 K for High-Pt and 600K for Low-Pt) there appears a new Pt state at lower binding energy at about 72.0 eV (Pt $4f_{7/2}$). This state can be assigned to metallic platinum in the form of very small small particles. Similarly as was reported in the chapter 3, it can be explained in the terms of the size effect, which causes shifting of this peak to higher BE and therefore it does not have the typical BE of metallic platinum (Pt $4f_{7/2}$ about 71.2 eV) [73].

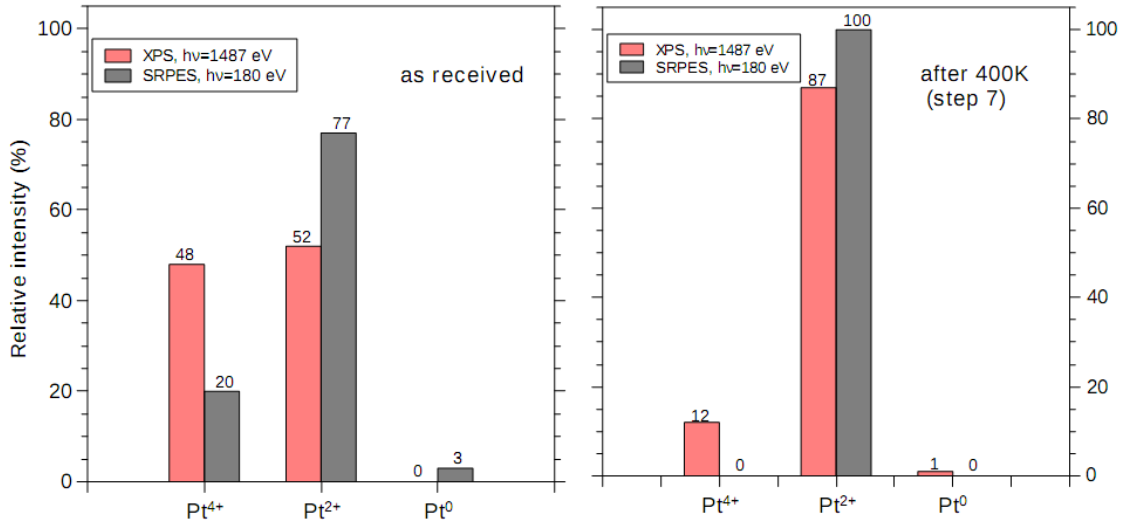

Figure 4.1.4: Photoelectron spectroscopy „depth profiling“: relative content of Pt 4f spectra components for sample Pt-CeO_x LowPt, comparison of as received state and state after 400K heat treatment, measured with different surface sensitivity

Comparison of changes in low-Pt and high-Pt samples during annealing

The evolution of selected parameters for the two type of samples with different platinum content is compared in Fig. 4.1.5.

In the as received state the sample with higher Pt content the ceria is more reduced as indicated by the RER number (about twice higher value), this is also with agreement with the Ce 3d XPS spectra (Fig. 4.1.2).

The High-Pt sample has also bigger fraction of Pt in 4+ state and lower relative signal of lattice oxygen. Since the ceria is more reduced in the High-Pt sample, also the BE separation was found to be lower ($O_{lattice}$ component is found on higher BE in as received state).

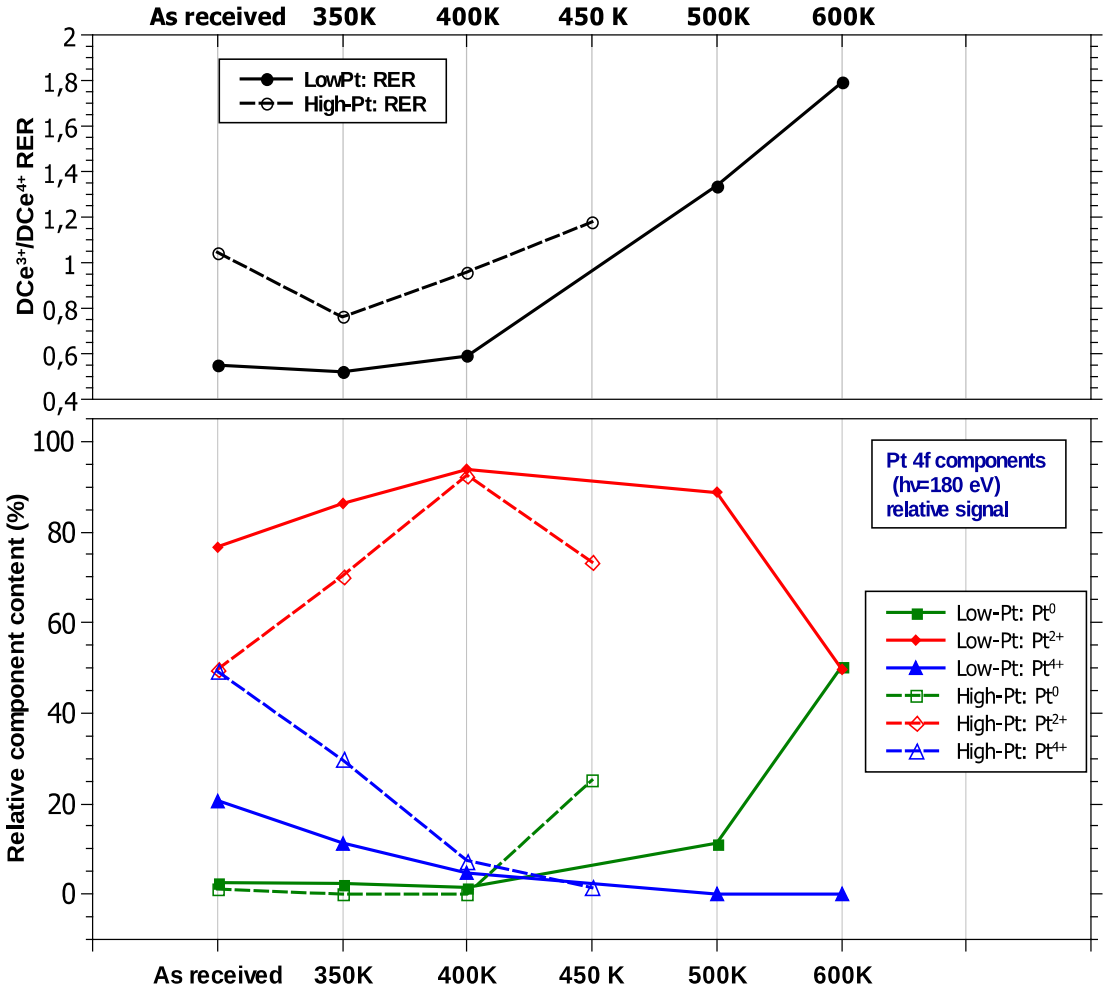

Figure 4.1.5: Comparison of samples Pt-CeO_x Low-Pt and Pt-CeO_x High Pt: RER number, Pt 4f components relative content.

For both samples mild heat treatment of 350K for 10 minutes already causes Pt^{4+} state to disappear partially as can be seen from in Fig. 4.1.5 indicating that the 4+ state is not very stable. The effects are stronger for High-Pt sample. In that case the

RER number decreased slightly more during this step. It might be connected with decrease of Pt^{4+} content, however in the case of Low-Pt sample, there is almost no change in RER observed.

After annealing at 400 K both samples exhibited maximum in Pt^{2+} content and almost all Pt^{4+} was transformed to Pt^{2+}, however, no metallic component was observed yet.

In case of High-Pt sample after annealing to 450K (only measured for this sample) remaining Pt^{4+} (as observed by SRPES) seems to be transformed into metallic state. Some part of Pt^{2+} state is also transformed into metallic component, because its relative content decreased a little. Apparently the maximum capacity of sites in the surface region suitable to stabilise the Pt^{2+} state was reached for this Pt concentration, so any Pt exceeding this capacity changes into metallic.

In case of Low-Pt sample the next major change starts to take place after heating to about 500K. The metallic platinum then starts to form on the surface.

After further heating to 600K, the structural changes in layer are more radical and significant amount of platinum in metallic state is formed. Because this Pt 4f peak for "metallic" platinum is rather wide and shifted to higher BE it is very likely an exhibition of size effect and probably small particles with various sizes are formed. Here it was possible to fit the Pt component using one asymmetric doublet (Doniach-Šunjić shape convoluted with Gaussian) slightly shifted to higher BE. This could be easily explained by presence of one or more population of very small platinum particles, which then due to size effects are observed on higher BE.

The same can be said for Pt^0 component on High-Pt sample after the 450 K treatment.

The most interesting fact is that there is still substantial amount of platinum in 2+ state left even after annealing to relatively high temperatures. It confirms stability of this species even on this rather porous graphitic samples. It indicates there are still many suitable "nanopockets" present on the rough surface, where can Pt^{2+} exist in stable configuration [80].

The evolution of ceria oxidation state monitored by RPES starts with partially reduced state for both types of samples. With higher annealing temperatures it can be summarized that the RER number increases with every increase in the temperature. The Low-Pt sample starts with lower RER, but after 500K it already surpasses the High-Pt sample at 450 K. Unfortunately it is not possible to compare on higher temperatures. For the Low-Pt sample there is significant change in RER after 500K towards more reduced ceria (RER about 1.3) and after 600K the reduction increased even more, reaching the RER number of about 1.8.

Regarding the reliability of the RER number, the reduction state of the surface is to some extent influenced by instability of some samples under irradiation with X-rays. Especially at initial state of the samples the irradiation was observed to cause reduction of ceria in some cases. The reduction due to irradiation was fast at first but later stabilising at certain values (not shown). So the values of RER should be treated as overestimated in the initial steps (up to factor of about 2). However in later stages of the experiment, the error is likely much smaller. Anyway the error of determination of RER is at least 10% in any case.

Sample CeO_2

Similar procedure had been attempted also with pure ceria on C-foil with no added Pt. Unfortunately it turned out that the sample was very unstable under irradiation (XPS and SRPES), so there are no data presented for this sample. Generally in can be said that the ceria does not interact with the hydrogen under UHV conditions. Reason has been given in for example [81], the theoretical calculation determined barrier for H_2 molecule to dissociate on common sites on ceria surface is about 1 eV, so for example much higher pressures would be needed for that.

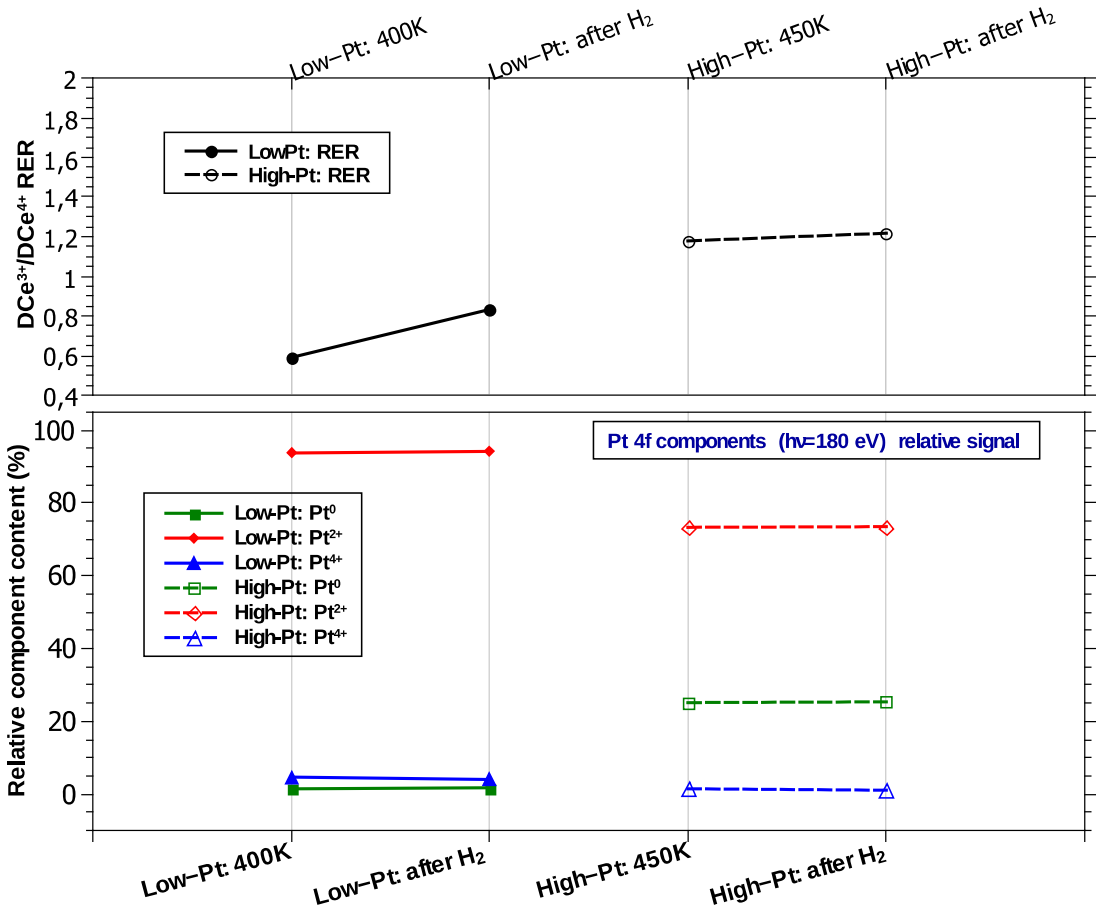

Figure 4.1.6: Effect of H_2 exposition on samples Pt-CeO_x Low-Pt (after 400K annealing) and Pt-CeO_x High Pt (after 450K annealing): RER number, Pt 4f components relative content

Effect of Hydrogen exposition

Samples were exposed in various stages to hydrogen (up to 600L) in some cases also in combination with water (10L). Effect of hydrogen was generally minimal, on the edge of detection limit. Selected results for Low-Pt sample (250 L H_2 exposition after 400K annealing) and for High-Pt sample (10 L H_2 exposition after 400K annealing) are displayed in Fig 4.1.6. The results are practically the same, as was obtained in other stages of experiment after exposition of samples to hydrogen.

On the platinum 4f spectra, there is negligible change either in intensity or in relative content of components.

To some extent, the ceria becomes little more reduced judging from change in RER. For Low-Pt sample the change is bigger compared to High-Pt sample.

The minimal effect of hydrogen on the studied samples in the UHV experiment is most likely due to the “pressure gap” effect.

4.2 Atmospheric pressure study of interaction of hydrogen and water with Pt-CeO_x catalyst layers

Hydrogen and water vapour treatment of the catalyst layers simulating the FC working condition such as temperature, gas flow and humidification was performed using the laboratory-designed micro-flow reactor (for more details about this equipment see [82][Johanek2015_ASS]).

The samples were prepared similar way as samples in previous chapter used for UHV stability experiment. In this case, there were also different set of samples prepared on silicon wafer supports, that were used in the micro-reaction apparatus experiment. These samples have different concentration of platinum. The parameters are shown in table 4.2.1.

In order to simulate the real fuel cell conditions, the interaction with hydrogen or water was done at temperature of about 340 K. The samples were then exposed to 30sccm flow of hydrogen. In case of water, helium gas was used as a carrier going through a humidifier.

Each exposure had 24 h duration and immediately after the exposition, the samples were transported into in UHV chamber equipped with the XPS to be characterized.

sample	layer thickness	Pt/Ce ratio (XPS)
Pt-CeOx / C-foil	25 nm	0,19
CeO2 / C-foil	22 nm	---

Table 4.2.1: Composition and thickness of samples used for atmospheric pressure experiment

Distinguishing effects of treatment with water vapour and dry hydrogen

Effects of exposition of the samples to water vapour or dry hydrogen is demonstrated by the first set of measurements where catalytic layers were deposited on a silicon wafer substrate. The Ce3d, Pt 4f and O1s XPS spectra are shown in Fig. 4.2.1. Although catalyst layers deposited onto a Si-wafer substrates generally has different morphology then on C-foil, the principal changes can resolved and the difference in interaction with water or hydrogen can be distinguished. This set of samples were prepared with different loading of platinum, according to XPS the Pt/Ce ratio was found to be 0,08.

The "as prepared" sample shows Ce state to be mostly 4+ with only small amount of reduction indicated by rather deep valley in the Ce 3d spectra at binding energy characteristic for Ce^{3+} species (a doublet component labelled Ce^{3+} [f^1]) at about 886 eV BE. Platinum is mostly in 4+ state, only some small amount of Pt^{2+} is present, no metallic component was detected. Oxygen O1s spectra suggest some presence of hydroxyl groups. Similarly as in the case of the UHV study, it is possible to clearly distinguish only two main components, that is the lattice oxygen peak and secondly the unresolved component belonging mainly to hydroxyl groups (chemisorbed water) and oxygen species related to oxygen vacancies together with other minor species. In case of lattice oxygen the same approach is kept as in the UHV study and the peak is treated as a single component, although separation of contributions from Ce^{3+} and Ce^{4+} species could be attempted.

After hydrogen exposure, the layer becomes substantially reduced as is clearly visible in the Ce 3d spectra, a strong Ce^{3+} component signal appears. Pt 4f spectra shows that platinum 4+ signal practically disappears and end up being converted to metallic and 2+ state. Presence of large amount of Pt^{2+} state after reduction by hydrogen indicates its stability and large capacity of the catalyst to support this Pt^{2+} species.

The change in O1s spectra related to the reduction of ceria is not straightforward, as was also shown in the case of UHV study. The relative intensity of the component at high BE increases by factor of about 2 in respect to lattice oxygen component. The BE separation between the components is also increased by about 0.3 eV.

There is also a possibly very small shift of lattice oxygen component to higher BE by about 0.1 eV after reduction but this is below reliable determination in this case.

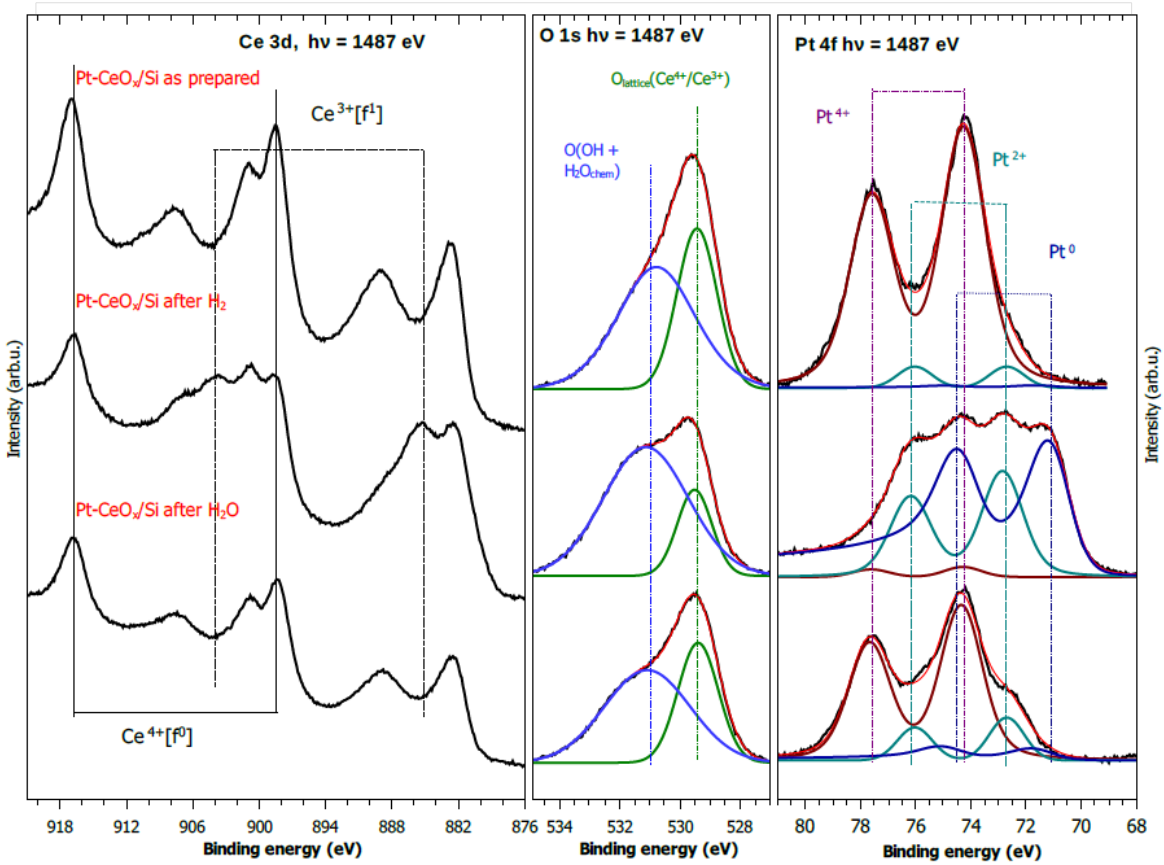

Figure 4.2.1: Distinguishing the effects of water and hydrogen exposure at 80 °C on samples of Pt-CeOx/ Si wafer: XPS spectra of Ce 3d, Pt 4f, O 1s.

This change in O 1s spectra can be explained with appearance of increased number of oxygen vacancies created due to reduction by H_2 and thus providing more sites for hydroxyls groups and chemisorbed water. Also higher amount of the surface OH groups species attenuates some of the bulk signal where lattice oxygen mostly originates. Some of the lattice oxygen close to surface is probably removed by interaction with H_2 forming OH groups or water species which then can desorb from the surface. As is proposed in [81] the platinum plays important role in this process, because it can facilitate the reaction with hydrogen by allowing reverse spillover of oxygen from ceria onto platinum particles, which are formed on the surface. Then the disso-

ciated hydrogen located on the Pt particles can react easily with the oxygen and leaving the surface in the form of water and causing reduction. This at same time destabilizes the Pt2+ and thus it promotes transformation into metallic platinum particles.

In case of interaction with water (middle spectra in in figure 4.2.1), the results show that the surface is also reduced to some extent, but much less than in the case of exposure to hydrogen. There is a small increase in content of Ce^{3+} in the Ce 3d spectra. Also small part of the platinum originally mostly in 4+ state is now transformed to 2+ state, but in much less amount compared to case after interaction with hydrogen, there is a trace amount of metallic platinum species present. This Pt species transformation may be however induced just by the increased temperature (if compared to UHV experiment, at 350 K already fraction of Pt^{4+} was transformed into Pt^{2+}). In the O1s spectra there is minor change after water treatment: the ratio between component at higher BE and lattice oxygen increased by about 10% and there is again an increase in BE separation by about 0.3 eV.

It should be noted that after the exposure in both cases there were observed some contamination of the surface by carbon based species (not shown). This contamination might be originating from external sources during the experiment.

Water can effect the surface with vacancies via dissociation to a hydroxyl group thus leaving one hydrogen behind. This hydrogen can then interact [81] with oxygen from ceria forming another hydroxyl group. That could explain the small extent of the reduction of the surface. As long as there is sufficient partial pressure of water the surface is covered by chemisorbed water and further reduction is limited. This similarly may works as inhibiting factor when wet hydrogen interacts with the surface as the adsorbed/chemisorbed water blocks reduction by hydrogen as was proposed also in [83].

Effect of humidified hydrogen on samples prepared on C-foil substrate

This set of experiments simulated closely the environment in PEMFC anode. The XPS data from before and after annealing in hydrogen for catalytic layers supported on C-foil are displayed in Fig. 4.2.2. The samples prepared on C-foil have much rougher surface (SEM image in Fig. 4.1.1) than Si wafer supported ones (compare e.g. Fig. 3.1.1) since there is the reactive sputtering effect for c-foil substrates. Generally ceria in samples Pt-CeOx/C-foil is already moderately reduced in as prepared condition (judging by the not so deep valley at about 885 eV in Ce 3d spectra). To some extent this Ce^{3+} signal can also be coming from the ceria-carbon interface. The reduced ceria phase is known to be present at the interface [83], also carbide formation is possible [84].

The effect of long exposition to wet hydrogen at elevated temperatures can lead to extreme reduction of the ceria catalytic layer, as displayed in Fig. 4.2.2 (bottom spectra). In this case the reduction is so extended that almost no ceria is left in the 4+ state.

Surprisingly the Pt^{2+} species in rather high amount are still present in the surface region in spite of observed ceria state change. This is probably the most important observation. Moreover the Pt^{2+} can apparently coexist together with platinum in metallic state.

The Ce 3d spectra for the reduced Pt doped ceria does not appear entirely like pure Ce^{3+} oxide. Likely, there are some carbides from the ceria-carbon interface present which would influence the peak shape and also it is possible that the layer is not homogeneously charging due to irradiation by X-ray source. Spectra of O 1s are not shown, the changes are principally same as was observed for the layers on Si wafer.

Similar experiment was done also with pure ceria deposited onto C-foil for comparison. (Fig. 4.2.2) After similar procedure the extent of reduction is only minimal. This suggest that the presence of platinum is necessary and have key role in the reduction of ceria layer on C-foil.

Appearance of Pt in oxidised form inside the Pt-CeO_2 is a very interesting thing. Although the various platinum oxides itself are not very stable the platinum interacting with cerium oxide forming Pt^{2+} state seems to be quite stable and resist even strong reducing condition.

Platinum oxide deposited on carbon foil or other substrates can be readily reduced in hydrogen atmosphere even at room temperature as was shown for example in [82]. After decomposition the PtOx, platinum particles are formed with very small sizes which then present high active surface area, this can be used as a way how to prepare Pt catalyst with small particles and large surface area. However in case of interaction with ceria the Pt stays in the oxidised form is quite stable.

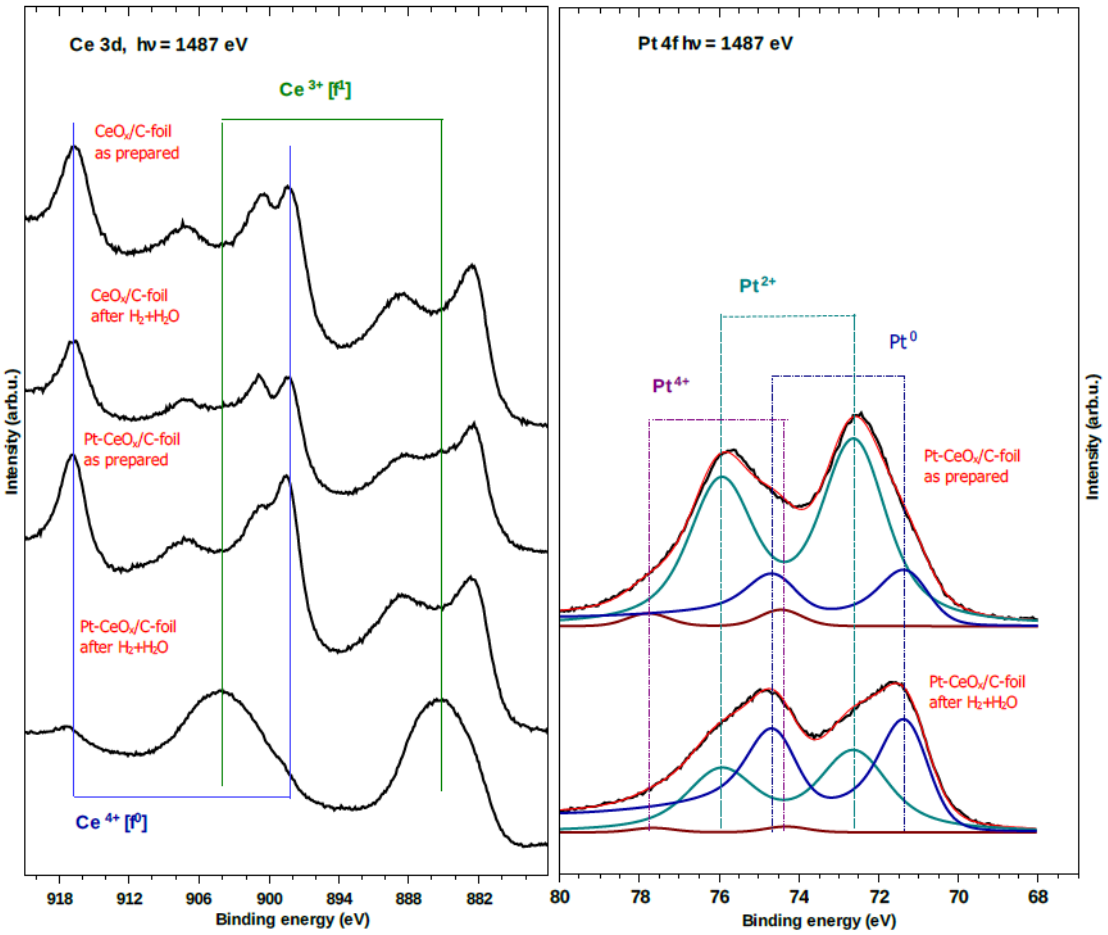

Figure 4.2.2: Effects of humidified hydrogen exposure on Pt-CeOx/C-foil and CeOx/C-foil samples at 80 °C: XPS spectra of Ce 3d, Pt 4f.

Summary

Pt–cerium oxide catalyst is at least partially reduced in working PEMFC anode conditions.

The most important result is a high stability of Pt^{2+} ionic species in spite of strong reducing conditions.

Long enough treatment with hydrogen can cause whole surface region (as far as the XPS surface sensitivity goes) to be reduced, forming Ce atoms mostly in 3+ state. This change is interconnected with changes in platinum state – metallic platinum is formed after such exposure in metallic state nevertheless still significant amount of Pt^{2+} is surviving. This apparently depends on available sites able to stabilize the Pt cation.

Pure ceria without platinum is reduced much less compared to platinum doped ceria, the platinum plays key role in the process of reducing the catalyst layer with hydrogen at atmospheric pressure.

Therefore, we believe that Pt^{4+} ions are dispersed in substituting bulk Ce^{4+} ions whilst Pt^{2+} are stabilized in specific surface sites. DFT calculations [80] explained the high stability of Pt^{2+} by their anchoring as single ions in 4 oxygen square pockets of the $CeO_2(100)$ nanofacets. Low stability of Pt^{4+} is explained by their substitutional character in the bulk ceria lattice. These defect-like states are not stable in principle.

5 Sputtered Pt-Co and Pt-Ni low platinum content Fuel Cell Cathode Catalyst

Introduction

The cathode side reaction – oxygen reduction reaction (ORR) in the PEMFC is regarded as very challenging from the point of view of active catalyst. There are only few known well working catalyst and among them the only practically usable catalysts requires platinum. The problem of this reaction is the kinetic limitation. For example the ORR running on platinum catalyst is running roughly 1000 times more slowly than the hydrogen oxidation reaction (HOR) taking place on anode of PEMFC. There is no catalyst known so far that would dramatically change this situation. Since platinum is rare and expensive it is viable to at least reduce the amount of platinum on the cathode side as much as possible. One of the ways is to alloy Pt with other metals (Ni, Co, Fe), use advanced types of catalyst supports. There exist ORR catalysts that do not contain platinum (e.g. based on N-doped graphene, or based on polyaniline, Iron and Cobalt) [85] but their performance and stability is inferior to platinum based catalyst still. PtCo and PtNi based catalysts are regarded as one of the most reliable ways, how to improve the specific activity on the cathode[22] [71].

There have been a lot of research on the use of PtCo catalyst for ORR on the fuel cell cathode, because of the improved performance, notably studying the stability and identifying the active phases [43] [44]. Also many studies that tried to explain the role of Co in the mixed catalyst in the increased activity towards ORR. There are several effects increasing the surface area/number of active sites. Modifying the electronic structure of valence band in Pt alloy to improve adsorption properties of oxygen.

The experiences gained with thin film anode catalyst with low Pt loading were

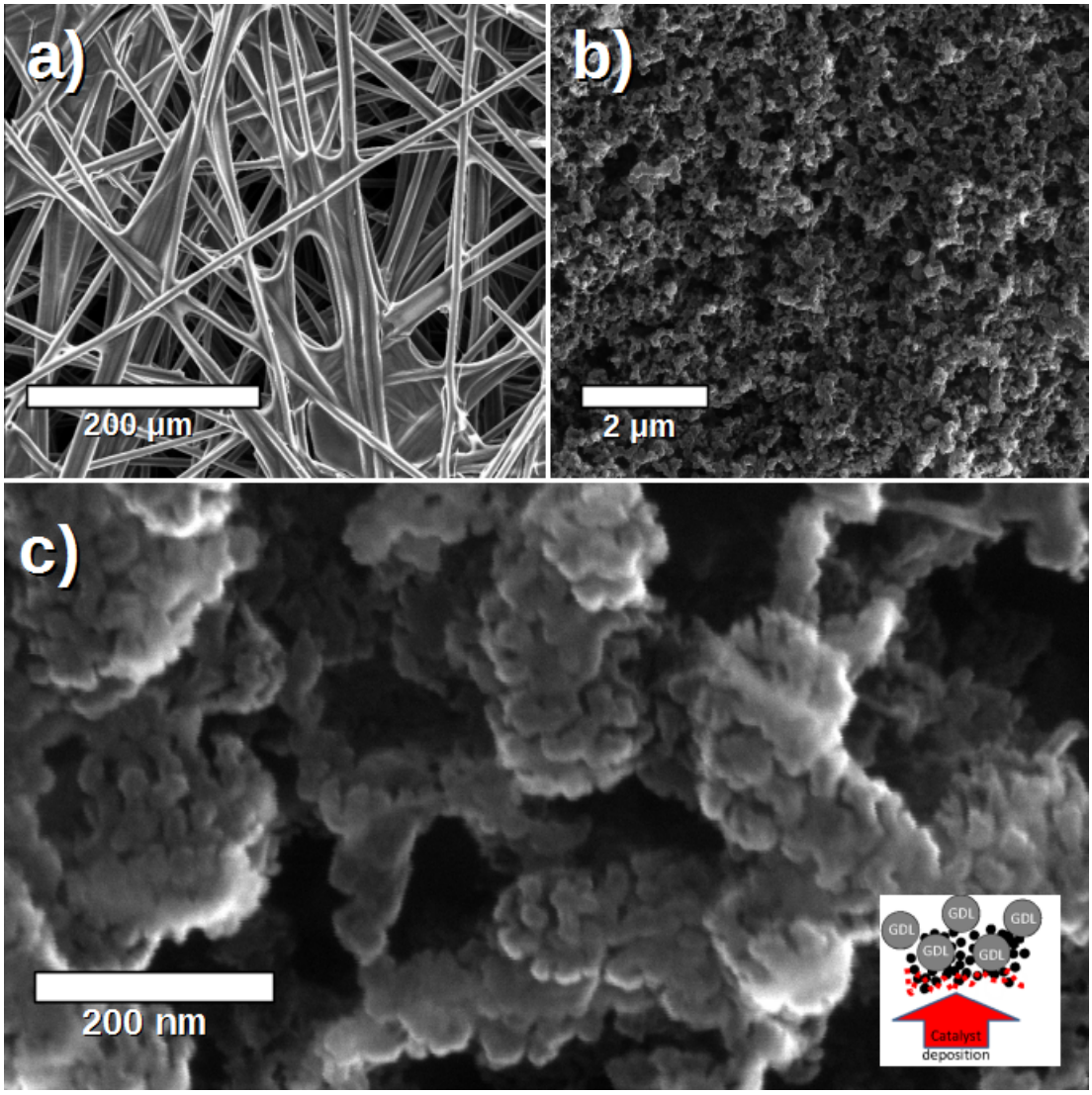

used to prepare series of catalysed electrodes for fuel cell cathode. Samples with different thickness of catalyst layer and with different composition were prepared to be tested in real FC conditions. Pt-Co based catalyst was selected as the material to explore in more detail and evaluate the best parameters of preparation from the point of view of performance in real fuel cell condition and then further optimize catalysts properties.

Experimental

Catalytic thin films based on platinum and cobalt used in this study were prepared by simultaneous (non-reactive) magnetron sputtering from two sources. One, TORUS 2" (Kurt J. Lesker) UHV magnetron, powered by r.f. signal (Advanced energy, Cesar 136 r.f. generator) was used to deposit cobalt from a Co target (1mm

thick, 99.9%). The second source for deposition of platinum was a laboratory designed magnetron using a Pt target (51mm diameter, 2mm thick, purity 99,9%), powered by DC sputtering source (Advanced Energy, MDX-500). The deposition was carried out in Ar atmosphere at 6 $x10^{-1}$ Pa working pressure, distance target-sample was about 9cm from both sources, angle between sources normal was about 45 degrees. The concentration of constituents in the Pt-Co catalyst were controlled by changing the applied power to each magnetron. Sputtering at typical conditions (20W DC power on Pt source and 20W r.f. Power on Co source) gave the Pt-Co film deposition rate of 3.3 nm/min. Equivalent thickness of deposited layers was checked on a flat substrate (Si wafer) that was coated together with samples using Atomic Force Microscopy.

The FC tests were performed by using pneumatically compressed graphite single cell (Greenlight TP-5 Research Cell) using 800 kPa piston pressure (yielding about 70 $N.cm^{-2}$ pressure on MEA). We used MEA with an active area of 4.6 cm^2 formed from 0.05 mm thick Nafion membranes (DuPont Inc., Nafion NR-212) and from the catalysed anode and cathode GDLs. As each FC anode electrode we used commercially available catalyst coated GDL (Alfa Aesar, Reformate Anode, product No. 45368, nominal loading of Pt 0.39 mg/cm^2) in all prepared samples. The cathode electrodes were created by coating GDL with nanostructured carbon particles (nGDL) (SGL TECHNOLOGIES GmbH, Sigracet GDL 25 BC) with our catalysts deposited by magnetron sputtering.

In order to compare results with commercially available catalysts, we also made a measurement with cathode electrode from Alfa Aesar (Reformate Cathode, No. 45452, nominal loading of Pt 0.39 mg/cm^2).

The flow rates of hydrated H_2 and O_2 were controlled to give stoichiometry of 1.2 for hydrogen and 2 for oxygen, with minimum flow of 40 $ml.min^{-1}$ and 30 $ml.min^{-1}$ respectively. If not noted otherwise the presented results are for reactants over-pressure of 0.5 bar relative to atmospheric pressure, on both anode and cathode, the cell was operated at 70 degree Celsius and with close to 100% relative humidity (humidifiers operated at the same temperature as the cell, 70 °C).

During the test, we observed the same procedure, consisting of break-in sequence, series of polarization curves for different conditions, impedance

spectroscopy characterization, cyclic voltammetry characterization and repeated checking of IV characteristic measurements.

X-ray photoelectron spectroscopy (XPS) analysis of prepared catalytic layers was performed in laboratory XPS apparatus described in chapter 2.

Morphology and structure of Pt-CeOx/nGDL were observed by means of Scanning Electron Microscopy (SEM) using the Tescan MIRA 3 microscope and TEM measurements were done using the JEOL 2100F microscope more details are given in chapter 2 as well.

The typical SEM image of the sputtered mixed Pt-Co catalyst deposited onto a nGDL support can be seen in the figure 5.1 b). The nGDL has a layer of carbon nanoparticles with typical sizes in range of 30 to 100nm fixed onto carbon fiber GDL, that creates the roughness on the larger micro-scale. These carbon nanoparticles are then decorated by the deposited catalyst, which exhibit structure on the fine nano-scale by forming small grains. Here can be observed some difference between pure Pt catalyst and Pt-Co one. When mixed with cobalt, the layer has much finer grain structure in the range below 10 nm. More details can be seen from TEM observation shown in Fig 5.1 c), which confirms presence of many nanocrystals in size range of typically 3-8 nm.

Within the group of samples with different Pt-Co mixture there was however no observable morphology difference seen by SEM (not shown) with available resolution.

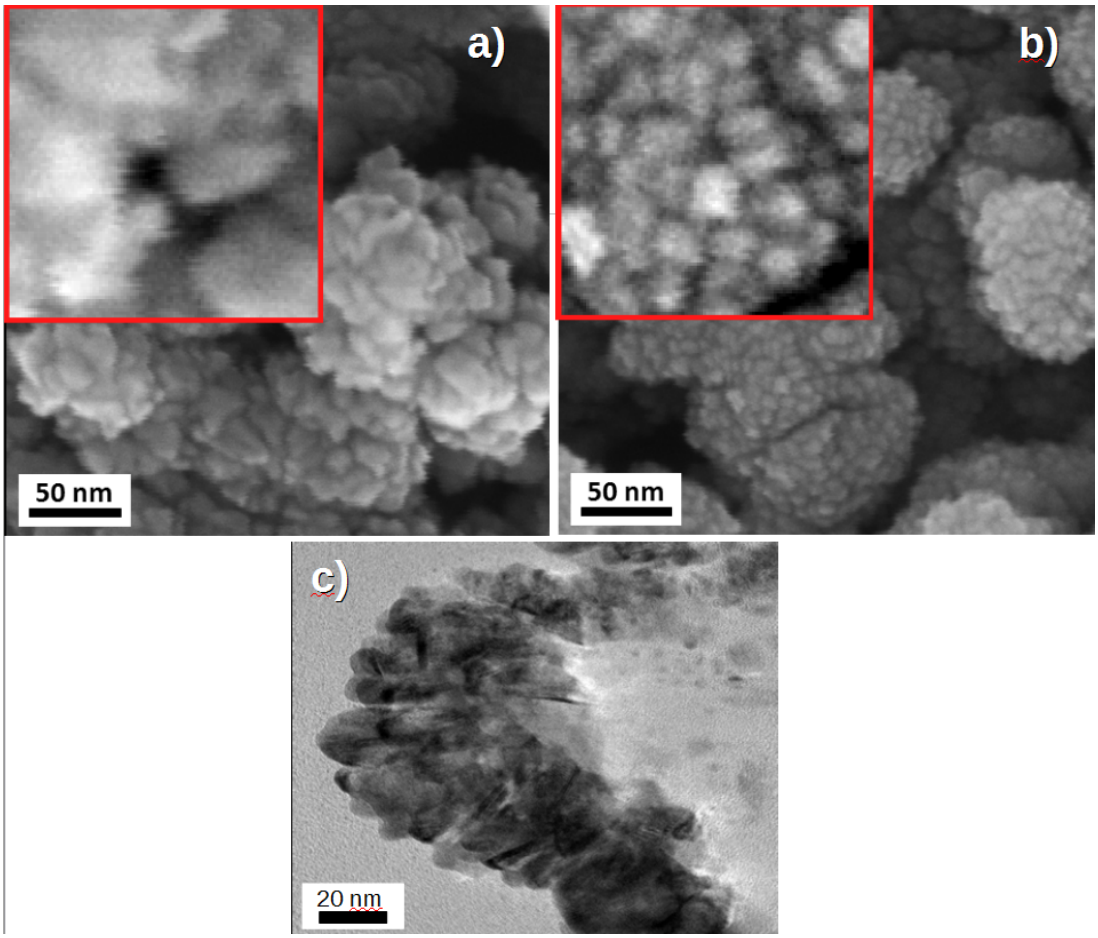

Figure 5.1: SEM image of sputtered Pt (a) and Pt60%-Co40% (b) catalysts (50nm equivalent thickness) on nGDL support, panel (c) shows TEM detail form the sputtered Pt-Co catalyst

XPS spectra of the Co-Pt sample with 60% Pt content and about 50nm equivalent thickness are displayed in Fig. 5.2. The Co 2p spectrum of the as-prepared sample consists of three characteristic doublets: Co2+ as predominant species at binding energy (BE) of about 781-797.2 eV, shake-up satellite of Co^{2+} at 786.1-802.7 eV and metallic component at 778.5-793.8 eV. From relative intensities of the

components in the spectrum, it is evident that amount of cobalt oxides in the as-prepared Pt-Co catalyst is substantially higher relative to the Co-metal content.

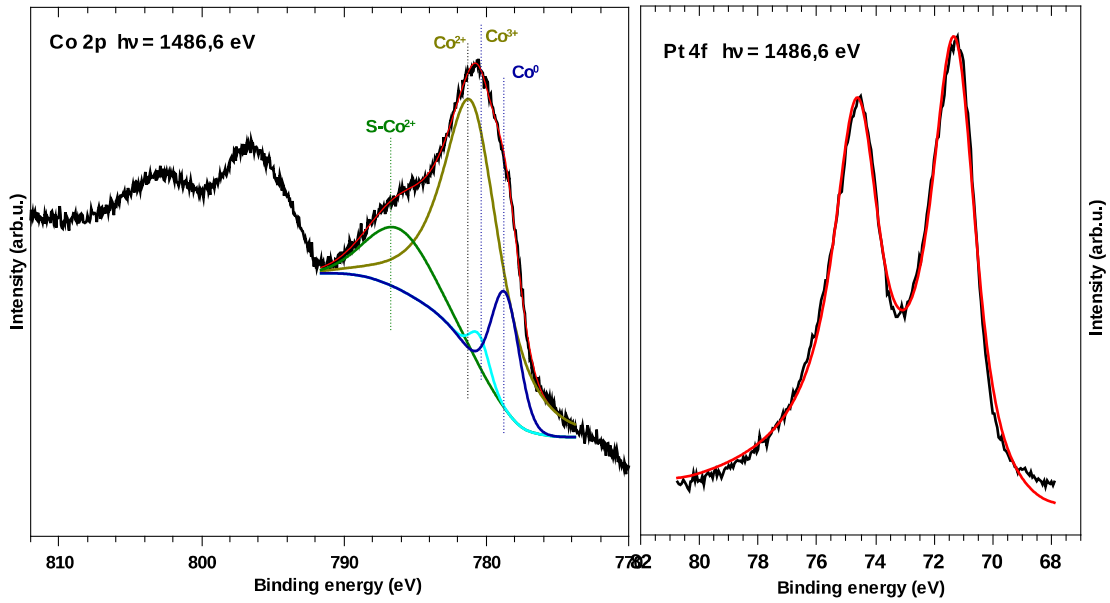

Figure 5.2: XPS spectra of as prepared layer of $Pt_xCo_{(1-x)}$ catalyst layer (50nm thickness, about 60% Pt content)

This occurs because Co is easily oxidized on the surface of the Pt-Co catalyst by ambient atmosphere after removing the sample out from the deposition chamber. Metallic Co in turn corresponds to bulk Co. In the Pt 4f XPS spectra there is no indication of any difference from metallic Pt, it can be reasonably well fitted using one doublet of asymmetric Doniach-Šunjić shape. It is likely that the Pt is partially alloyed with Co, but the typical BE shift is very small, reportedly about 0.2 eV [86] and is not possible to distinguish in this case with XPS.

The Pt/Co concentration ratios for the catalyst samples were determined using XPS analysis from the corresponding Co 3p and Pt 4f peak areas corrected using calculated atomic photo-ionization cross sections (more details are in chapter 2). It should be noted that this approach provides only ratio in the surface layer depending on the information length and that may differ significantly from the film bulk. The

values were generally in agreement with ration obtained by EDX. The results and loading of platinum calculated from them are presented in table 5.1.

Sample	Equivalent layer thickness (nm)	Pt concentration $Pt_xCo_{(1-x)}$	Loading of Pt ($\mu g.cm^{-2}$)
10nm_Pt100	10	1	20
10nm_Pt80	12	0,8	19,2
10nm_Pt60	12	0,62	14,88
10nm_Pt40	11	0,4	8,8
25nm_Pt100	22	1	44
25nm_Pt80	25	0,75	37,5
25nm_Pt60	30	0,6	36
25nm_Pt40	30	0,35	21
50nm_Pt100	50	1	100
50nm_Pt80	58	0,84	97,44
50nm_Pt60	51	0,62	63,24
50nm_Pt40	50	0,45	45
reference - cathode	---	1	390

Table 5.1: List of Pt-Co samples for fuel cell tests with determined parameters of thickness and composition

From the results it is obvious there were some variation (up to 20%) from the expected values of thickness and composition, but since many fuel cell parameters can be normalized to platinum loading, it should not cause much problems. Nevertheless the error of the determination itself of both concentration and thickness can be estimated to be at least 10%.

PtCo Fuel Cell Tests

Fuel cell test were done according to internally developed testing protocol which includes break-in procedure and contains a series of IV polarization curves and is derived from the publicly available testing protocols.

Maximum power density from FC polarization curves (obtained for 1,5 barA operation, 70 °C H_2 & O_2 operation) and calculated corresponding specific power density are shown in table 5.2.

Sample	Maximum power density ($mW.cm^{-2}$)	Deviation from mean value of power density	High frequency resistance ($m\Omega.cm^{-2}$)	Specific power ($W.mg_{Pt}^{-1}$)
10nm_Pt100	287	2,0%	166	14,4
10nm_Pt80	330	5,0%	129	17,2
10nm_Pt60	297	6,0%	180	20
10nm_Pt40	250	1,6%	129	28,4
25nm_Pt100	394	3,0%	139	9
25nm_Pt80	389	2,0%	162	10,4
25nm_Pt60	382	8,0%	116	10,6
25nm_Pt40	342	1,0%	185	16,3
50nm_Pt100	365	2,5%	125	3,7
50nm_Pt80	379	6,0%		3,9
50nm_Pt60	332	3,0%	439	5,2
50nm_Pt40	297	14,0%	490	6,6
reference	720	0,5%	153	1,8

Table 5.2: Determined maximum power density and corresponding specific power density together with high frequency resistance from impedance spectroscopy analysis. The maximum PD is average from several measurements with 30s stabilization for each step, the deviation is standard deviation from the averaged values.

Presented data of maximum power density are an average of 3 repeated measurements (on each single sample) with stabilization of 30s per step. The high frequency resistance (HFR) necessary for internal cell resistance (iR) correction were obtained using external potentiostat equipped with impedance spectroscopy module, before break-in procedure. Details about the method are in chapter 2.

Stabilization time of 30s per step was chosen as a compromise between sufficient stabilization and elapsed time of the whole experiment. Polarization with other time values were tried also (300s per step and 3s per step), nevertheless the obtained values are typically almost linearly related, anyway within the error of determination of the value of maximum PD. The error can be estimated to be on the order of 10% given precision of electric parameters measurement and the individual variation of results obtained from one sample (influenced for example by slow processes connected with humidification).

The obtained values of maximum PD and specific power density are also plotted as a bar-graph in Fig. 5.4.

Within the group of laboratory prepared catalysts the highest performance was surprisingly obtained on some of samples with 25nm thickness (Pt60 – Pt100) and on some 50nm thick samples with high Pt loading (Pt80, Pt100), the values of PD were bigger than in case of all other samples. Regarding PD value, the 10nm samples on the other hand had the lowest PD from all the results.

If the dependence on composition of Pt and Co is compared then highest power densities were obtained from samples with 100% Pt or about 80% Pt content. Samples with lower Pt content showed generally in all cases relatively low power densities in absolute numbers.

It is evident, that the maximum performance obtained with the commercial reference cathode catalyst is better than any of the studied samples prepared by sputtering (although by a small factor). Obviously, the commercial catalyst has much higher loading and it can be expected to be optimized from the structure a composition point of view.

In case of the samples 50nm_Pt60 and 50nm_Pt40 the measured value of HFR unfortunately suggest that these cells have been probably poorly assembled and so the performance was influenced by this and therefore all other reported values for them might be unreliable.

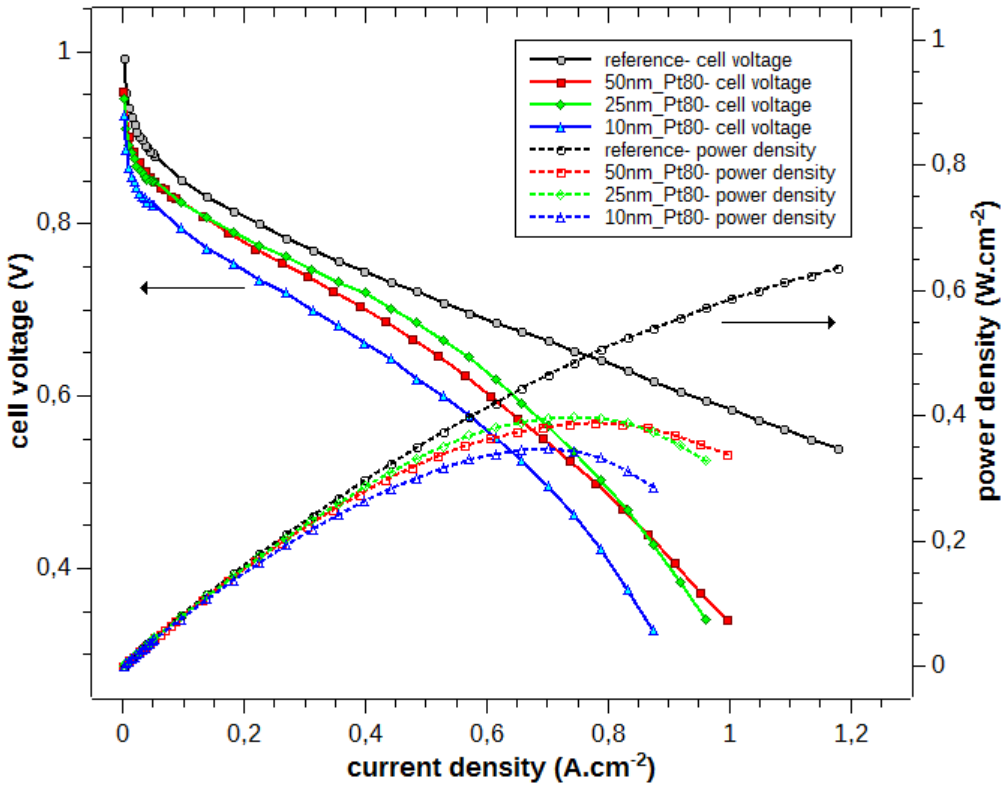

Figure 5.3: Polarization & power density curves for selected Pt-Co cathode samples and comparison with reference. (H2 & O2 operation, 1,5barA, 70 °C, 30 s per step stabilization).

If one looks at obtained specific power values, then the figure is completely opposite. Samples with lowest platinum loading, that is 10nm samples and especially those with smaller fraction of Pt, exhibit the highest specific power values (up to 20 $W.mg_{Pt}^{-1}$). Specific power calculated for the commercial catalyst was found to be rather low on the other hand (<2 $W.mg_{Pt}^{-1}$). The reason is probably that in the commercial electrode there is much more catalyst used than is necessary (in order to increase durability) and also Pt particles which are typically used in these type of catalyst contain in the core significant amount of Pt atoms that are not contributing to the active phase.

This effect could be in principle used to prepare fuel cell electrodes with minimized platinum loading which would require, however, large geometric area of MEAs in order to compensate the smaller power density in absolute measure. This

might useful e.g. in some stationary powering systems. Nevertheless, these electrocatalysts might be suitable to low cost low power applications like Edu-stacks, small electronic powering and similar. It would be dependent on cost benefit analysis of the price of all the other components necessary to produce larger size MEAs.

In certain applications, there are more important priorities. For example for automotive applications, the volumetric power density is more important than high specific power. And in such cases, also different catalyst parameters would be priority. So in this automotive example certainly the PD has to be high as priority. If economy should also taken into account, then high catalyst mass activity together with high PD would be priority.

Typical polarization curves of selected samples are presented in Fig. 5.3. Chosen were curves for each sample from group of 10 nm, 25nm and 50 nm thickness and they are compared with reference catalyst.

From the polarization curves it is obvious, that the sputtered samples exhibit somewhat lower voltage at given current density compared to reference catalyst. For small current densities, this difference is not so large, however for higher current densities there starts to be the most prominent effect of mass transport limitation.

The reference catalyst obviously does not show any significant mass transport overpotential in the displayed range whereas the performance of sputtered samples start to drop already from about 0.6 $A.cm^{-2}$. Better view into this matter is possible using a corresponding Tafel plot on Fig. 5.5. This issue is discussed in more detail later.

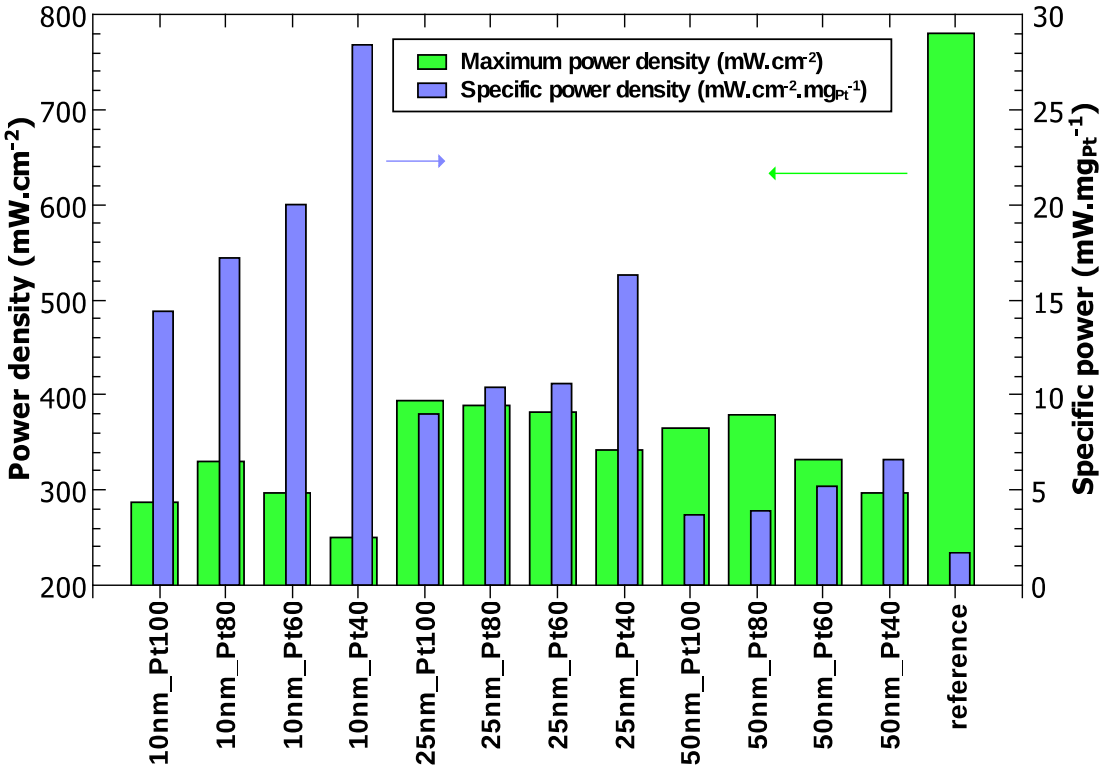

Figure 5.4: Average maximum power density and Specific power density (H2 & O2 operation, 1,5barA, 70 °C). Dependence on layer thickness and composition and comparison with reference cathode results.

Electrochemically active surface area

To obtain values of ECSA of the catalyst (microscopic active area corresponding to number of active sites on the catalyst-electrolyte interface) which is needed e.g. for calculation of specific activity. cyclic voltammetry measurement was done on the cathode catalyst samples using the simplified electrochemical setup, where the anode works both as a counter and a reference electrode. (details in chapter 2). And from the cyclic voltammetry the number of active catalyst sites were estimated form determination of integrated charge corresponding to hydrogen desorption from the surface (H_{upd} desorption). It should be noted that this method may produce biased values for Pt alloy catalyst in some cases, as was demonstrated in [44] where for well-defined skin type Pt-Co particles or for annealed particles,

where the skin is formed, the ECSA determined from H_{upd} peak and by CO stripping is different. In this case there is no annealing so the influence should not be so big. The error of ECSA determination is anyway rather large because of experimental difficulties obtaining stable voltammogram and also there is uncertainty in defining scanning ranges so as not to influence the desorbed charge and also issue of correctly subtracting the background signal (double layer capacity + hydrogen crossover effects). The total error may be in some cases even in absolute value comparable to the determined value. So here the alloy effect is considered to be negligible.

Sample	H_2 desorption charge ($mC.cm_{geo}^{-2}$)	Roughness factor ($cm_{micro}^2.cm_{geo}^{-2}$)	ECSA ($m_{micro}^2.g_{Pt}^{-1}$)
10nm_Pt100	0,12	0,6	2,8
10nm_Pt80	0,18	0,8	4,3
10nm_Pt60	0,24	1,1	7,6
10nm_Pt40	0,17	0,8	9,4
25nm_Pt100	0,39	1,8	4,2
25nm_Pt80	0,45	2,1	5,7
25nm_Pt60	0,41	2	5,4
25nm_Pt40	0,22	1,1	5,1
50nm_Pt100	1	4,6	4,6
50nm_Pt80	1,5	7,2	7,4
50nm_Pt60	0,8	3,8	6
50nm_Pt40	0,37	1,8	3,9
reference cathode	19	36	23

Table 5.3: ECSA of Pt-Co catalyst samples

From the value of integrated charge corresponding to the H_2 anodic desorption one can calculate the ECSA of the catalyst relating the determined value of charge to generally accepted value for an ideal polycrystalline flat platinum sample, which is 210 $\mu C.cm^{-2}$ [87].

Obtained values of ECSA for studied samples are shown in table 5.3. The H_2 anodic desorption charge, which is assumed to be proportional to the number of active sites, display a trend, which can be roughly summarized as that the desorption charge is proportional to the thickness of catalyst layer for given composition of Pt_xCo_{1-x}. With changing composition for one thickness, it can be said that samples

with 80% Pt had the highest values within the group, whereas the sample with 40% had the lowest.

The values of determined ECSA, which describes how effectively is the contained platinum forming active sites suggest that the sputtered catalyst sample exhibit comparable values (just little lower, typically within 30%) compared to the value of about 23 $m^2.g_{Pt}^{-1}$ determined for the commercial catalyst. Only samples with very low Pt content (40%) and the sample "10nm_Pt100" had relatively lower values of ECSA. Effects that may play role are for example contact of active sites with the solid electrolyte (Nafion membrane) in this special setup unlike in the case of half-cell experiments with classical liquid electrolyte.

The value determined for sample "50nm_Pt80" seems to be out of reasonable range and is most likely result of some error. When compared with value of H_2 desorption on reference cathode catalyst it is evident that the commercial electrode has at least an order or two higher active surface area. This obviously explains the observed difference in performance of the catalyst.

The addition of Co or possibly other transitional metal into Pt alloy has positive effects towards ECSA, it might be explained for example by influencing surface roughness.

Mass activity

The most suitable parameter to characterize and compare efficiency of different catalysts for the ORR reaction at FC cathode free from effect of other losses such as mass transport limitation is the mass activity (MA). In order to eliminate any concentration polarization and other mass transport losses it is determined from low current density region of polarization curve and with pure O_2 and H_2 reactants. The ohmic losses can be subtracted when the internal resistance is known (it can be measured by impedance spectroscopy). In the simple model of electrochemical reaction then only process remaining is the kinetic polarization, which is a specific process for given catalyst and electrolyte combination.

The kinetics of the electrochemical reactions are well described by Butler-Volmer equation 2.6 or when far from equilibrium it can be simply described by Tafel equation 2.7. The main parameters are the exchange current density (defined at equilibrium from the Nernst equation) together with Tafel slope. Since it is not practical and almost impossible to measure directly the exchange current density,

usually the fact that polarization follows Tafel equation is used and instead of exchange current density a kinetic current at certain selected point is used (typically at 900 mV). From this kinetic current it is eventually possible to extrapolate and find the value of exchange current density (using Tafel slope), as long as polarization follows the Tafel equation.

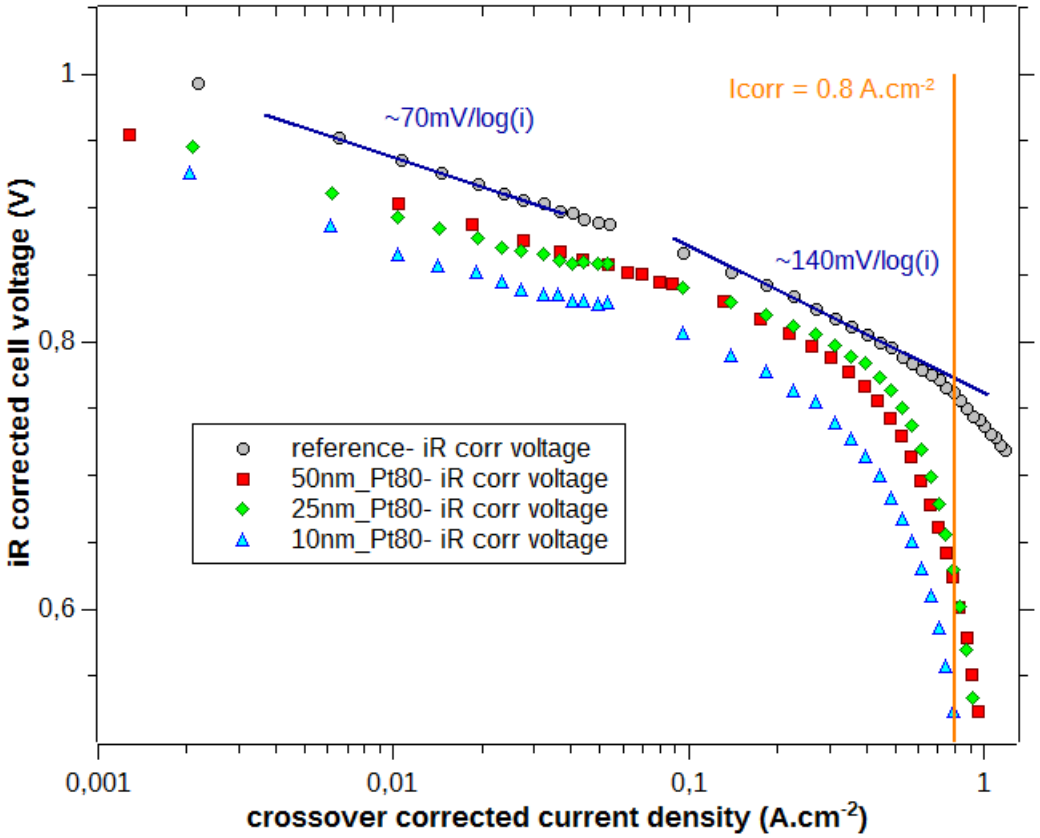

Figure 5.5: Tafel plots of polarization curves of selected PtCo catalyst samples and the reference catalyst (H2 & O2 operation, 1,5barA, 70 °C).

Tafel plot for selected polarization curves (same data as was used in figure with polarization curves) is displayed in Fig. 5.5.

In the low current density region (LCR) the polarization curves typically exhibit a Tafel slope of about 60 to 70 mV per decade of current, which can be

considered typical for the platinum based catalyst. It also means that kinetic limitation comes solely from the cathodic side in this region of current density, otherwise the observed Tafel slope would be sum of the cathodic and anodic Tafel slopes.

From this plot it can be clearly seen that for higher current density (higher than about 200 $mA.cm^{-2}$) there is a significant mass transport limitation for the sputtered samples.

The reference catalyst also start to exhibit some minor mass transport loss starting from about 700 $mA.cm^{-2}$, but the voltage loss is much lower. Vertical line at current density of 800 $mA.cm^{-2}$ helps illustrate the difference. Tafel slope values determined for the samples are presented in table 5.4. Two of the samples (10nm thickness, Pt100 and Pt40) exhibit somehow higher value of Tafel slope. That might be explained for example by instability of the samples during IV char measurement or that there other voltage loss sources.

Also the current density at 900 mV from corrected data (for iR and crossover current) are listed in the table. From that value of selected current density and platinum loading, it is possible to calculate the mass activity. Values are presented in the table as well.

Sample	Activation polarization current @900 mV, 1.5barA ($mA.cm_{geo}^{-2}$)	Tafel slope - LCR ($mV.log(A)^{-1}$)	Mass Activity @900mV, 1.5barA ($mA.mg_{Pt}^{-1}$)	Specific Activity @900 mV, 1.5barA ($mA.cm_{micro}^{-2}$)
10nm_Pt100	1,8	90	92	3,3
10nm_Pt80	3,2	63	164	3,3
10nm_Pt60	3,2	82	215	3,0
10nm_Pt40	2,2	83	244	2,6
25nm_Pt100	6,4	62	146	3,5
25nm_Pt80	8,4	62	225	4,0
25nm_Pt60	8,9	60	248	4,6
25nm_Pt40	5,2	62	246	4,9
50nm_Pt100	10,4	62	104	2,3
50nm_Pt80	11,8	66	121	1,6
50nm_Pt60	4,8	62	76	1,3
50nm_Pt40	3,7	67	81	2,0
reference	34	73	87	0,4

Table 5.4: Determined mass activity (kinetic current at 900 mV) in fuel cell operation from iR and crossover corrected data (1.5 barA reactant pressure)

The most interesting thing about the Pt-Co mixture catalyst is the fact that they exhibit substantially higher mass activity compared to pure platinum catalyst, in other words the activity of the catalyst does not change in spite of the decreasing content of platinum in the Pt-Co mixture. All the samples without addition of cobalt and also the reference catalyst exhibited mass activity close to 100 $mA.mg_{Pt}^{-1}$ at the experimental conditions (with the exception of 25nm_Pt100, which gave somehow higher MA for unknown reason). Opposite to that samples with mixture of Co and Pt (and thickness 10 or 25nm) exhibited MA of close to 200 $mA.mg_{Pt}^{-1}$ and better. The best MA from the set was obtained for samples with 40% and 60% of cobalt in the mixture (25nm and also 10nm thickness). So it seems that the best catalyst efficiency is available up to about 25nm, possibly somewhere between 25 and 50 nm equivalent layer thickness.

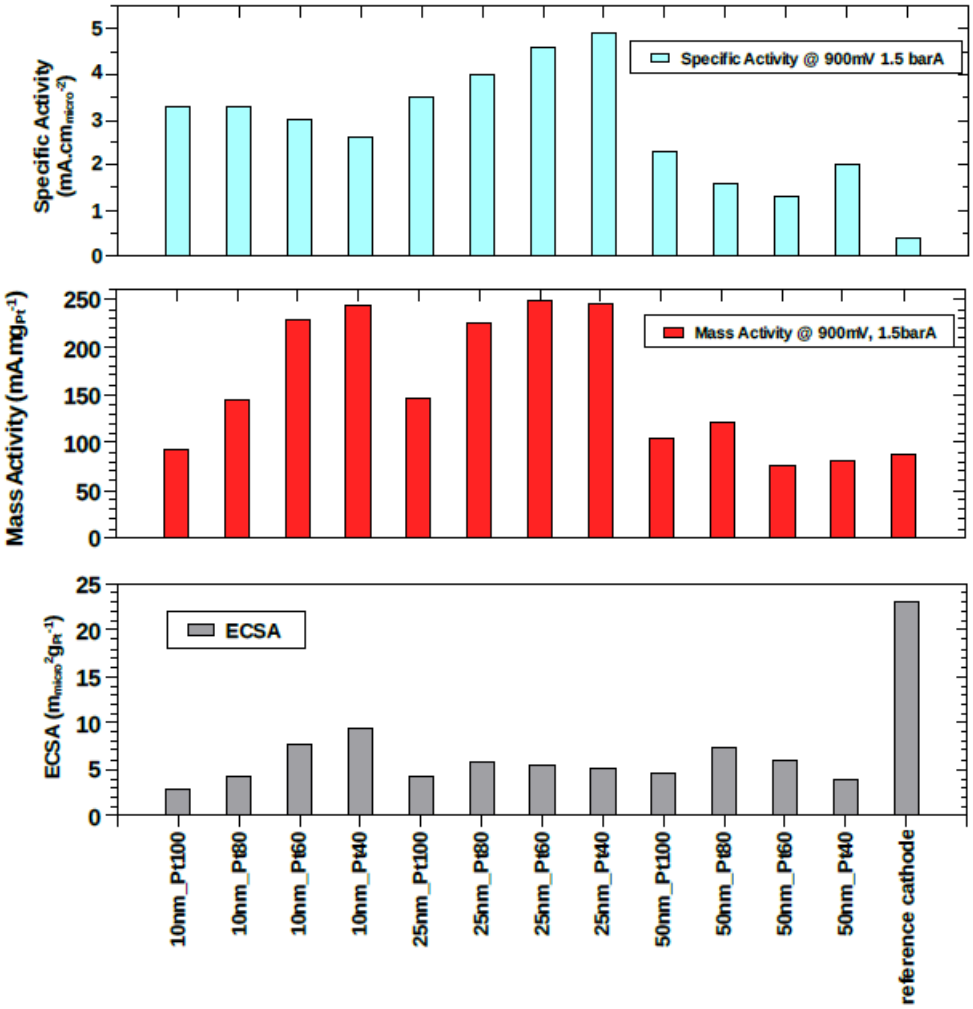

Figure 5.6: ECSA, Mass activity @ 900mV and Specific activity @ 900mV from PEMFC test with sputtered cathode PtCo/nGDL catalyst (H2 & O2 operation, 1,5barA, 70 °C). Dependence on layer thickness and composition and comparison with reference cathode results.

As has been noted earlier, the samples 50nm_Pt60 and 50nm_Pt40 might have been improperly assembled and therefore the results could be unreliable – as in this case, where the MA is outstandingly lower compared to other samples in the set.

When developing a catalyst with good performance the way could be to increase loading of a catalyst with good mass activity as much as the mass activity does not drop.

The fact, that some of the prepared samples exhibit from 2.5 up to 3 times higher mass activity is indication, that the technology indeed could provide way to prepare active catalyst with decreased loading of platinum. If the MA could be kept

constant, for the same power density obtained from reference catalyst with certain loading of Pt it would be sufficient to theoretically have one third less platinum when the mixed catalyst is used.

From the measured results it is unfortunately evident, that at some equivalent thickness between 25nm and 50 nm the mass activity starts to decrease.

So if there should be chosen a sample catalyst for further use, the MA results indicate the 25nm thickness and between 40 and 60 % platinum content should be used.

The error of determining MA is a combination of errors from determining the Pt loading and determining the current at 900 mV (using interpolation and averaging from more measurements), the total error is estimated to be at least 20%.

Specific activity

When both mass activity and ECSA are known it is possible to calculate another parameter using equation 2.5 (chapter 2, page 19) and that is Specific activity (SA).

Specific activity describes how effectively an active site promotes reaction. The determined values are also presented in the table 5.4. It is apparent that most of the thin film catalyst samples exhibit rather large SA of about 3 $mA.cm^{-2}$ whereas the commercial reference has value one order smaller. 50nm thick samples also have somewhat lower numbers, on the other hand the 25nm samples have the highest value.

It is possible that in case of here presented samples the values of SA are influenced by the measured ECSA values, which have rather large errors of determination, especially for the samples with low absolute ECSA.

Fuel cell operation with Air on cathode

Results presented above were all acquired from measurements done using pure oxygen on cathode which was essential for proper determination of catalyst activity and kinetic properties. However real fuel cell applications often require operation with air. In case of air fed cathode the mass transport problems typically becomes much more significant as the large amount of nitrogen present in air blocks transport of oxygen to the catalyst surface a therefore can cause concentration gradients and the increase of concentration/mass transport overvoltage.

Obtained maximum power density from polarization curves for selected samples operated on H_2 and air at 1.5 barA are displayed in figure 5.7. The values are compared with values obtained at otherwise similar condition with pure oxygen. The reference commercial catalyst was obviously designed to be operating with as it can provide more than 40% of PD obtained with oxygen, because initially the sample provided quite high PD already, even with air the PD is quite high, more than 300 $mW.cm^{-2}$.

In case of laboratory prepared samples however the drop in performance is much higher.

The trend is that samples with more platinum loading (thicker equivalent layer thickness) suffer less decrease in PD (in the figure, samples with 100% Pt and different thickness can be compared). Sample 10nm_Pt100 showed only little above 10% of PD obtained with oxygen, in absolute measure less than 50 $mW.cm^{-2}$ which is evidently insufficient for practical applications.

Within samples of the same thickness with different concentration of Pt it can be seen that samples with lower platinum concentration also suffer more form the mass transport losses induced by air operation.

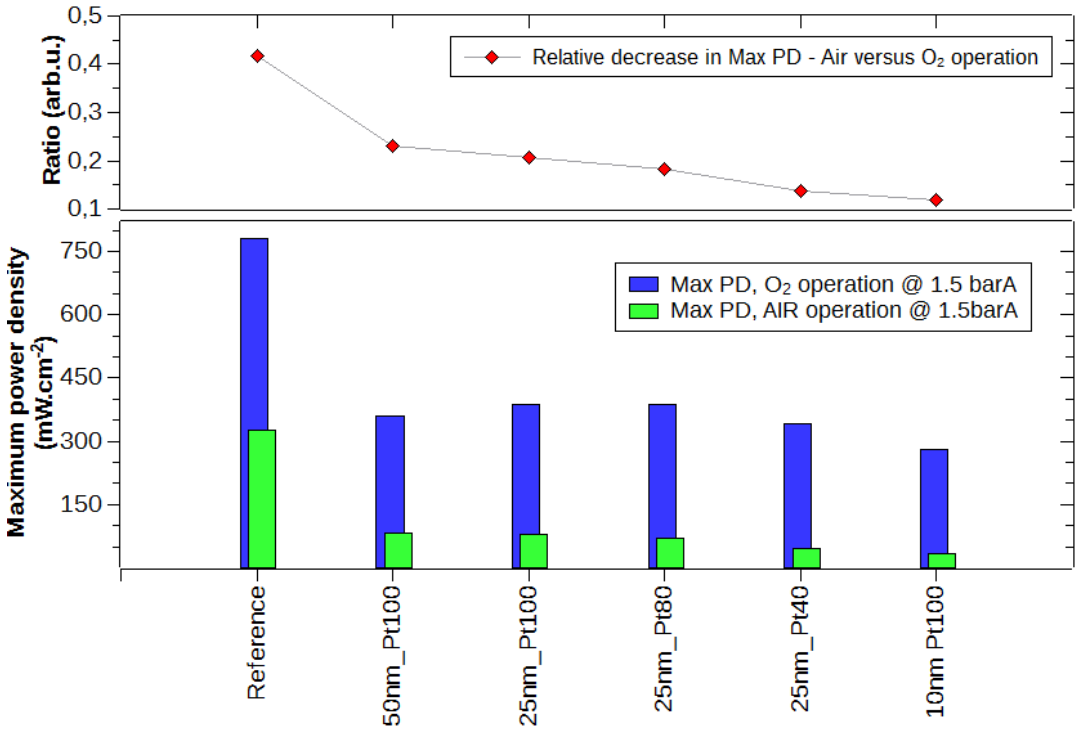

Figure 5.7: Average maximum power density and Mass activity @900mV from PEMFC test with sputtered cathode PtCo/nGDL catalyst (H2 & O2 operation, 1,5barA, 70 °C). Dependence on layer thickness and composition and comparison with reference cathode results.

Loss of activity due to ageing induced by cyclic voltammetry

It was observed that in case of many samples the performance has decreased in repeated checking measurement of polarization curves, which were done after the basic series of measurement with air, oxygen, different pressures and after cyclic voltammetry characterization.

The effect can is illustrated on two selected samples with 25nm thickness. Maximum power density at 1,5 barA with oxygen has decreased from 394 $mW.cm^{-2}$ to about 280 $mW.cm^{-2}$ (about 1.4 times lower) for the sample with 25nm thickness

and 100% Pt. For this sample also the mass activity has decreased from about 170 $mA.mg_{Pt}^{-1}$ to 100 $mA.mg_{Pt}^{-1}$.

For another sample with 40% Pt and 25 nm thickness the maximum power density for oxygen at 1 barA has decreased from value of about 240 $mW.cm^{-2}$ to 230 $mW.cm^{-2}$. Mass activity in this case dropped from 150 $mA.mg_{Pt}^{-1}$ to 110 $mA.mg_{Pt}^{-1}$.

Repeated cycling as done during cyclic voltammetry can be used to simulate fastened ageing of catalyst, as was shown for example on very similar samples in electrochemical and AFM study of PtCo catalysts in [88]. Also even repeated measurements of polarization curves lead to cycling, which is part of another ageing test. Typically the platinum surface gets repeatedly oxidized during open voltage (more precisely at potentials above about 0.86 V vs RHE) and reduced again at potentials below certain value and this leads to various morphological changes, reduced activity and ECSA are some of the consequences. In the paper [88] it was reported that for PtCo catalytic layers prepared by sputtering (without any treatment) there is big initial loss of active surface area even within several cycling repetitions (few hundreds), the ECSA dropped 30% after first 600 cycles. Interestingly the loss of ECSA was observed also for sputtered Pt catalyst, where the drop was 10% after first 600 cycles.

In this case it is not so easy to prove the deterioration due to ageing using polarisation data, because there is some, not negligible variation in individual measurements of the IV curves. However on average the trend is observable, it also appeared on more samples than was presented here. It is worth noting, that there was no significant decrease in performance observed on the reference commercial catalyst.

Tafel plots of selected IV curves which correspond best to the average values are displayed in Fig.5.8 There may be more factor influencing power density but loss of mass activity was observed as well. The possible changes in ECSA were not studied on the presented samples.

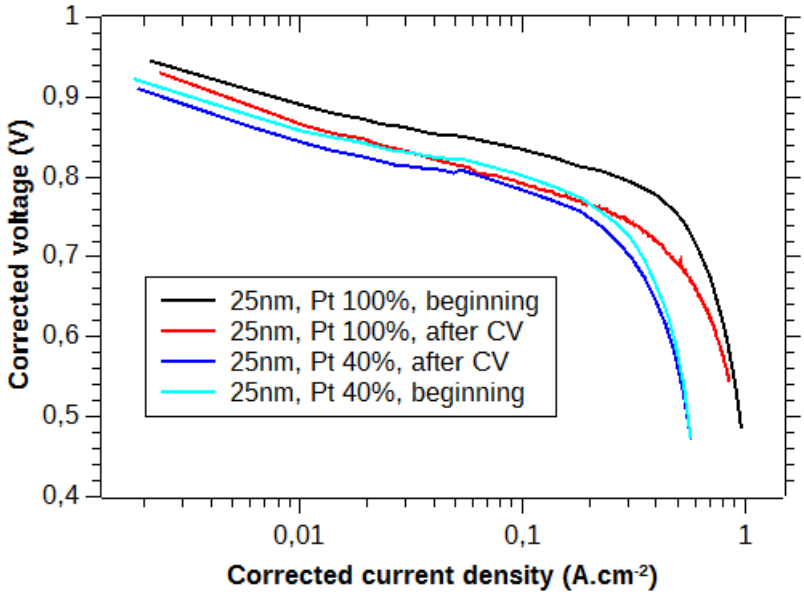

Figure 5.8: Tafel plot illustrating activity loss of samples 25nm_Pt100 and 25nm_Pt40 after completed set of characterization measurements.

Some of the inconsistencies in the sample results could be ascribed to the fact that samples were not prepared at once, but instead there were couple of series and also the measurement were done over a quite large time interval meaning there could have been some changes in e.g. deposition parameters.

Thickness of layers and concentration of Co/Pt are important for determining the platinum loading in the samples, however the uncertainty can be estimated to be at least 10% for each of them.

PtNi results

Next to cobalt also nickel is known to be improving the performance of platinum based catalyst for ORR. In order to compare the effect of addition of Ni with that of Co, another small series (this time with only 10nm equivalent thickness) of samples for FC cathode were prepared. Sputtered mixed Pt-Ni layers containing about 20%, 40%, 50% and 60% of Ni were deposited onto nGDL in order to be evaluated in the PEMFC.

XPS data (not shown) reveal very similar results as in case with Pt-Co mixture. Platinum 4f spectra correspond well to metallic platinum (alloying is possible, but not distinguishable). According to XPS Ni 2p spectra the nickel is present mostly in oxidized form (probably mixture of several oxide species) but again some signal corresponding to metallic Ni is present, which comes most likely from alloying with Pt.

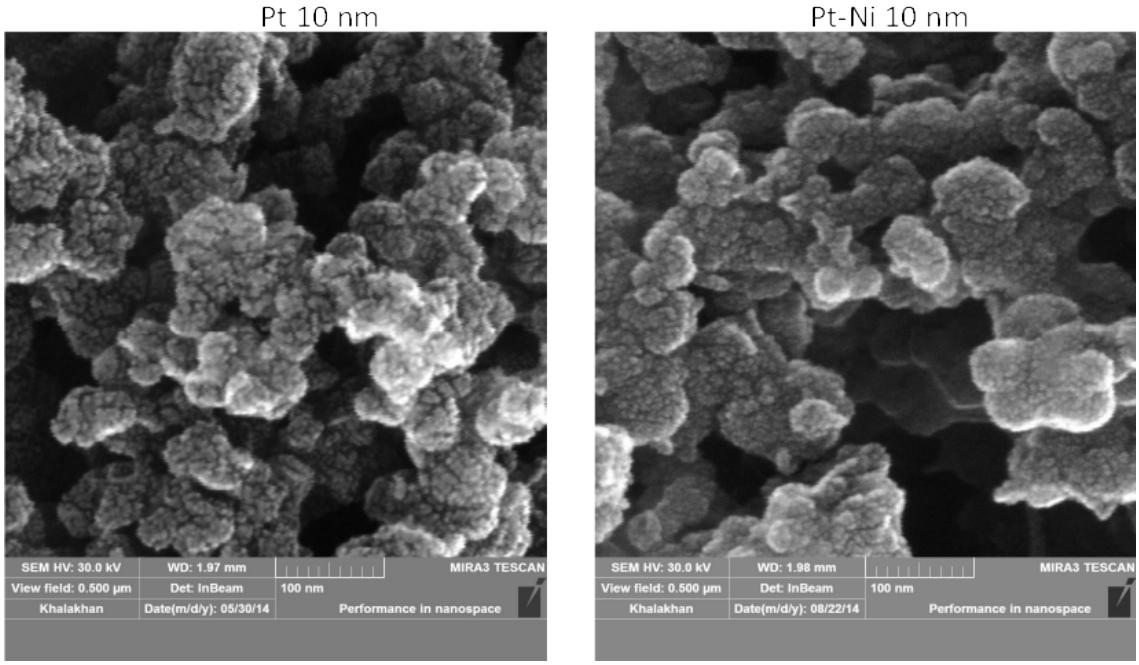

Figure 5.9: SEM images of sputtered 10nm equivalent of Pt (left) and PtNi (50%Pt) (right) onto nGDL support

SEM image shown in Fig. 5.9 reveals very similar structure to the one which has been observed in the case of Pt-Co.

The procedure of evaluating the fuel cell performance was as much as possible identical to that used on Pt-Co samples described before.

Typical polarization curves obtained for the Pt-Ni samples are displayed in Fig. 5.10

It can be said that the performance is comparable to the Pt-Co samples of similar properties.

More detailed comparison is possible using data shown in table 5.5.

Maximum power density is roughly similar, if the specific power related to platinum loading is compared, it can be said that Ni containing samples reached little better values than cobalt based 10nm samples. The highest power density was obtained for sample with 60% of platinum. In case of the 10nm group of Pt-Co samples, the highest performance in power density had the sample with 80% of Pt.

Sample	Catalyst loading ($mg.cm^{-2}$)	Maximum power density ($mW.cm^{-2}$)	Specific power ($mW.mg_{Pt}^{-1}$)
PtNi_10nm_Pt80	0.016	320	20
PtNi_10nm_Pt60	0.012	332	28
PtNi_10nm_Pt50	0.01	245	25
PtNi_10nm_Pt40	0.008	241	30

Table 5.5: List of Pt-Ni samples (10nm equivalent thickness) and fuel cell test results

From comparison of determined ECSA it seems the PtNi samples have a rather higher value on average. But taking into account the uncertainty in determination of the ECSA, the difference is not significant.

The most interesting electrochemical characteristic – mass activity seems to have similar values, possibly little higher. Interesting is the result of sample with Pt60% Ni40% that exhibited rather higher performance compared to other samples (this sample also had the highest maximum PD) yielding mass activity of about 350 $mA.mg_{Pt}^{-1}$.

Specific activity however in this case is about the same value in the group and comparable with results in literature and the PtCo samples..

Sample	ECSA ($m_{micro}^{2}.g_{Pt}^{-1}$)	Mass Activity @900mV, 1.5barA ($mA.mg_{Pt}^{-1}$)	Specific Activity @900 mV, 1.5barA ($mA.cm_{micro}^{-2}$)
PtNi_10nm_Pt80	8	219	2,8
PtNi_10nm_Pt60	12	350	2,9
PtNi_10nm_Pt50	11	230	2,2
PtNi_10nm_Pt40	9	263	2,9

Table 5.6: Pt-Ni samples,determined ECSA Mass activity, Specific activity

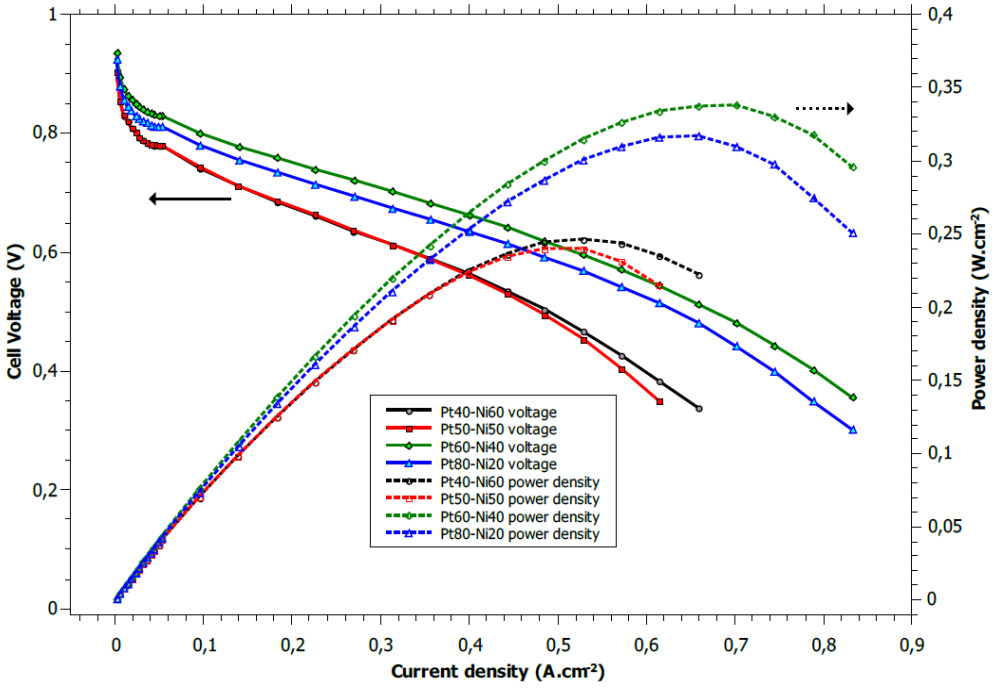

Figure 5.10: Polarization curves for series of $Pt_xNi_{(1-x)}$ samples obtained for 1,5 barA operation with H_2 and O_2 at 70 °C

Fully thin film technology low platinum loading MEA: Pt-CeO_x on anode and PtCo on cathode

After assessment of the performance of Pt-Co cathode catalyst the achievement of producing a PEMFC with laboratory prepared magnetron sputtered thin film catalyst on both electrodes was possible.

A combination of loadings of 0.002 mg_{Pt} .cm^{-2} in the Pt-CeO_x anode and 0.048 mg_{Pt} .cm^{-2} in $Pt_{0,5}Co_{0,5}$ cathode were used. In the fuel cell test with the total loading of 0.05 mg_{Pt} .cm^{-2} power density of 125 mW.cm^{-2} was obtained. This corresponds to about 2.5 kW.g_{Pt}^{-1} overall specific power. The results are published in [89].

Summary

We have shown that magnetron sputtering as thin film technology can be used for fabrication of low platinum loading electrodes for ORR in PEMFCs. We have confirmed that in case of the sputtered catalyst there is a positive effect of Pt mixing with transition metals, cobalt in this case. Fuel cell tests revealed increase of specific power by a factor of about two for mixture of Pt:Co 40:60, while power density remains almost the same.

When an GDE with higher catalyst loading is needed it is very likely to be most challenging with the same technology of preparation as was used to prepare studied samples. When layer thickness reaches some value the catalyst is starting to loose mass activity and therefore increasing loading has limited additional effect on performance of catalyst. There might be ways around this problem, as was shown for example in [90], where authors prepared multilayer of Pt and Co.

For the use in PEMFC cathode a mixed platinum-cobalt and platinum-nickel catalysts were prepared using magnetron sputtering and their performance evaluated.

It was demonstrated that both Pt-Co and Pt-Ni offer a better mass activity by a factor of more than 2 for wide interval of compositions compared to only Pt containing catalyst offering potentially better platinum efficiency of the catalyst.

Dependence of Pt-Co catalyst performance on composition sputtered layer thickness and of catalyst were studied. Within the studied samples, 25nm thick PtCo layers with concentration of Pt from 40% to 60% displayed the highest mass activity.

In case of PtNi the highest mass activity was found for $Pt_{0.6}Ni_{0.4}$ sample.

Conclusion

In this thesis the novel nanostructured Pt-CeO2 material for fuel cell (FC) anode catalysts are shown. The material is based on nanoporous CeO_2 thin films prepared by physical deposition techniques, particularly by simultaneous magnetron sputtering of Pt and CeO_2. This method permits to prepare oxide layers continuously doped with Pt atoms during the growth and, compared to commonly used chemical wet techniques, it is economical, scalable, and environmentally friendly. For making catalysts, Pt-CeO_2 thin films can be sputter deposited on various planar or nanostructured porous substrates, mainly nanoporous carbon. The Pt-CeO_2 films show an exceptionally high activity in mediating formation of protonic hydrogen and they are stable at the anode side of the proton exchange membrane FC.

Despite excellent activity which is demonstrated by unprecedentedly high specific power, we will continue this study by developing further steps toward synthesis of even better ceria based nanocatalysts which require, however, to go beyond the current state of the art and to develop new approaches in model studies for reliable preparation of new type high index surfaces and to develop new advanced techniques for characterisation of electronic and crystallographic structure, charge transfer, morphology and molecular interactions at surface and interface. Particularly, transfer from low pressure to high pressure operando spectroscopy and microscopy surface analysis would represent groundbreaking development of model studies in ceria catalysis. In the broad field of technologically relevant surface reactions we will chose interaction with water which represents foundation stone of reactions in electrochemistry, photochemistry and live science.

Special effort will be devoted to improvement of activity of thin film cathode electrocatalysts. The results presented in this work showing high activity of Pt/Co and Pt/Ni alloys are promising. Actual results which are not shown in the thesis show that we can already reach power density of 0.5 W/cm2 by processing more porous carbon substrate. Such tendency leads to an optimistic vision that development of aforementioned new operando techniques and new approaches will lead to development of entirely thin film MEAs which could meet industrial requirements.

References

[1] W. R. Grove, ‘LXXII. On a gaseous voltaic battery’, *Philos. Mag. Ser. 3*, vol. 21, no. 140, pp. 417–420, Dec. 1842.

[2] S. Bernal, J. . Calvino, M. . Cauqui, J. . Gatica, C. Larese, J. . Pérez Omil, and J. . Pintado, ‘Some recent results on metal/support interaction effects in NM/CeO2 (NM: noble metal) catalysts’, *Catal. Today*, vol. 50, no. 2, pp. 175–206, 1999.

[3] C. M. Y. Yeung, K. M. K. Yu, Q. J. Fu, D. Thompsett, M. I. Petch, and S. C. Tsang, ‘Engineering Pt in ceria for a maximum metal-support interaction in catalysis’, *J. Am. Chem. Soc.*, vol. 127, no. 51, pp. 18010–18011, 2005.

[4] I. Stará and V. Matolín, ‘The influence of particle size on CO adsorption on Pd/alumina model catalysts’, *Surf. Sci.*, vol. 313, no. 1–2, pp. 99–106, Jun. 1994.

[5] J. Wang, H. Chen, Z. Hu, M. Yao, and Y. Li, ‘A Review on the Pd-Based Three-Way Catalyst’, *Catal. Rev.*, vol. 57, no. 1, pp. 79–144, 2015.

[6] M. Fernández-García, A. Martínez-Arias, L. N. Salamanca, J. M. Coronado, J. A. Anderson, J. C. Conesa, and J. Soria, ‘Influence of Ceria on Pd Activity for the CO+O2 Reaction’, *J. Catal.*, vol. 187, no. 2, pp. 474–485, 1999.

[7] P. SHENG, W. CHIU, A. YEE, S. MORRISON, and H. IDRISS, ‘Hydrogen production from ethanol over bimetallic Rh-M/CeO2 (M=Pd or Pt)’, *Catal. Today*, vol. 129, no. 3–4, pp. 313–321, Dec. 2007.

[8] Q. Fu, H. Saltsburg, and M. Flytzani-Stephanopoulos, ‘Active nonmetallic Au and Pt species on ceria-based water-gas shift catalysts.’, *Science*, vol. 301, no. 5635, pp. 935–8, 2003.

[9] Y. Suchorski, R. Wrobel, S. Becker, B. Strzelczyk, W. Drachsel, and H. Weiss, ‘Ceria nanoformations in CO oxidation on Pt(111): Promotional effects and reversible redox behaviour’, *Surf. Sci.*, vol. 601, no. 21, pp. 4843–4848, Nov. 2007.

[10] X. Tang, B. Zhang, Y. Li, Y. Xu, Q. Xin, and W. Shen, ‘The role of Sn in Pt–Sn/CeO2 catalysts for the complete oxidation of ethanol’, *J. Mol. Catal. A Chem.*, vol. 235, no. 1–2, pp. 122–129, 2005.

[11] S. Imamura, T. Higashihara, Y. Saito, H. Aritani, H. Kanai, Y. Matsumura, and N. Tsuda, ‘Decomposition of methanol on Pt-loaded ceria’, *Catal. Today*, vol. 50, no. 2, pp. 369–380, Apr. 1999.

[12] D. Pierre, W. Deng, and M. Flytzani-Stephanopoulos, ‘The Importance of Strongly Bound Pt–CeO x Species for the Water-gas Shift Reaction: Catalyst Activity and Stability Evaluation’, *Top. Catal.*, vol. 46, no. 3–4, pp. 363–373, Dec. 2007.

[13] P. Bera, K. C. Patil, V. Jayaram, G. N. Subbanna, and M. S. Hegde, ‘Ionic Dispersion of Pt and Pd on CeO2 by Combustion Method: Effect of Metal–Ceria Interaction on Catalytic Activities for NO Reduction and CO and Hydrocarbon Oxidation’, *J. Catal.*, vol. 196, no. 2, pp. 293–301, Dec. 2000.

[14] S. Fabris, S. de Gironcoli, S. Baroni, G. Vicario, and G. Balducci, ‘Taming multiple valency with density functionals: A case study of defective ceria’, *Phys. Rev. B*, vol. 71, no. 4, p. 041102, Jan. 2005.

[15] D. R. Mullins, S. H. Overbury, and D. R. Huntley, ‘Electron spectroscopy of single crystal and polycrystalline cerium oxide surfaces’, *Surf. Sci.*, vol. 409, no. 2, pp. 307–319, 1998.

[16] A. Fujimori, ‘Mixed-valent ground state of CeO2’, *Phys. Rev. B*, vol. 28, no. 4, pp. 2281–2283, Aug. 1983.

[17] V. Matolín, L. Sedláček, I. Matolínová, F. Šutara, T. Skála, B. Šmíd, J. Libra, V. Nehasil, and K. C. Prince, ‘Photoemission Spectroscopy Study of Cu/CeO 2 Systems: Cu/CeO 2 Nanosized Catalyst and CeO 2 (111)/Cu(111) Inverse Model Catalyst’, *J. Phys. Chem. C*, vol. 112, no. 10, pp. 3751–3758, Mar. 2008.

[18] M. Spankova, I. Vavra, S. Gazi, D. Machajdik, S. Chromik, K. Froelich, L. Hellemans, and S. Benacka, ‘Growth and recrystallization of CeO thin flms deposited on R -plane sapphire by off-axis RF sputtering’, *J. Cryst. Growth*, vol. 218, pp. 287–293, 2000.

[19] H.-Y. Lee, Y. Lee, Y. Hong, and K. Ko, ‘Interfacial reactions between RF sputtered CeO2 film and Si(100) substrate’, *Appl. Surf. Sci.*, vol. 228, no. 1–4, pp. 164–168, Apr. 2004.

[20] V. Matolin, M. Cabala, I. Matolinova, M. Skoda, J. Libra, M. Vaclavu, K. C. Prince, T. Skala, H. Yoshikawa, Y. Yamashita, S. Ueda, and K. Kobayashi, ‘Au+ and Au3+ ions in CeO2 rf-sputtered thin films’, *J. Phys. D-Applied Phys.*, vol. 42, no. 11, p. 115301, 2009.

[21] V. M. Vishnyakov, ‘Proton exchange membrane fuel cells’, *Vacuum*, vol. 80, no. 10, pp. 1053–1065, Aug. 2006.

[22] H. A. Gasteiger, J. E. Panels, and S. G. Yan, ‘Dependence of PEM fuel cell performance on catalyst loading’, *J. Power Sources*, vol. 127, no. 1–2, pp. 162–171, Mar. 2004.

[23] C. Yang, D. Wang, X. Hu, C. Dai, and L. Zhang, ‘Preparation and characterization of multi-walled carbon nanotube (MWCNTs)-supported Pt-Ru catalyst for methanol electrooxidation’, *J. Alloys Compd.*, vol. 448, no. 1–2, pp. 109–115, Jan. 2008.

[24] A. Katayama, ‘Electrooxidation of methanol on a platinum-tin oxide catalyst’, *J. Phys. Chem.*, vol. 84, no. 4, pp. 376–381, Feb. 1980.

[25] P. K. Shen, ‘Anodic Oxidation of Methanol on Pt/WO[sub 3] in Acidic Media’, *J. Electrochem. Soc.*, vol. 141, no. 11, p. 3082, 1994.

[26] J. Rajeswari, B. Viswanathan, and T. K. Varadarajan, ‘Tungsten trioxide nanorods as supports for platinum in methanol oxidation’, *Mater. Chem. Phys.*, vol. 106, no. 2–3, pp. 168–174, Dec. 2007.

[27] C. Xu, R. Zeng, P. K. Shen, and Z. Wei, ‘Synergistic effect of CeO2 modified Pt/C catalysts on the alcohols oxidation’, *Electrochim. Acta*, vol. 51, no. 6, pp. 1031–1035, Nov. 2005.

[28] C. L. Campos, C. Roldán, M. Aponte, Y. Ishikawa, and C. R. Cabrera, ‘Preparation and methanol oxidation catalysis of Pt-CeO2 electrode’, *J. Electroanal. Chem.*, vol. 581, no. 2, pp. 206–215, Aug. 2005.

[29] M. Takahashi, T. Mori, F. Ye, A. Vinu, H. Kobayashi, and J. Drennan, ‘Design of High-Quality Pt?CeO 2 Composite Anodes Supported by Carbon Black for Direct Methanol Fuel Cell Application’, *J. Am. Ceram. Soc.*, vol. 90, no. 4, pp. 1291–1294, Apr. 2007.

[30] A. Pfau and K. D. Schierbaum, ‘The electronic structure of stoichiometric and reduced CeO2 surfaces: an XPS, UPS and HREELS study’, *Surf. Sci.*, vol. 321, no. 1–2, pp. 71–80, Dec. 1994.

[31] C. Binet, A. Badri, and J. Lavalley, ‘A Spectroscopic Characterization of the Reduction of Ceria from Electronic Transitions of Intrinsic Point Defects’, *J. Phys. Chem.*, vol. 98, no. 25, pp. 6392–6398, Jun. 1994.

[32] G. Vicario, G. Balducci, S. Fabris, S. de Gironcoli, and S. Baroni, ‘Interaction of Hydrogen with Cerium Oxide Surfaces: a Quantum Mechanical Computational Study’, *J. Phys. Chem. B*, vol. 110, no. 39, pp. 19380–19385, 2006.

[33] G. Dutta, U. V Waghmare, T. Baidya, and M. S. Hegde, ‘Hydrogen Spillover on CeO 2 / Pt : Enhanced Storage of Active Hydrogen’, *Chem. Mater.*, vol. 19, no. 26, pp. 6430–6436, Dec. 2007.

[34] B. Hariprakash, P. Bera, S. K. Martha, S. A. Gaffoor, M. S. Hegde, and A. K. Shukla, ‘Ceria-Supported Platinum as Hydrogen-Oxygen Recombinant Catalyst for Sealed Lead-Acid Batteries’, *Electrochem. Solid-State Lett.*, vol.

4, no. 3, p. A23, 2001.

[35] V. Matolín, M. Cabala, I. Matolínová, M. Škoda, M. Václavů, K. C. Prince, T. Skála, T. Mori, H. Yoshikawa, Y. Yamashita, S. Ueda, and K. Kobayashi, 'Pt and Sn Doped Sputtered CeO 2 Electrodes for Fuel Cell Applications', *Fuel Cells*, no. 1, p. NA–NA, Jan. 2010.

[36] Z. Liu, X. Y. Ling, B. Guo, L. Hong, and J. Y. Lee, 'Pt and PtRu nanoparticles deposited on single-wall carbon nanotubes for methanol electro-oxidation', *J. Power Sources*, vol. 167, no. 2, pp. 272–280, May 2007.

[37] S. Kim and S. Park, 'Preparation and electrocatalytic activities of platinum nanoclusters deposited on modified multi-walled carbon nanotubes supports', *Anal. Chim. Acta*, vol. 619, no. 1, pp. 43–48, Jun. 2008.

[38] G. Wu and B. Xu, 'Carbon nanotube supported Pt electrodes for methanol oxidation: A comparison between multi- and single-walled carbon nanotubes', *J. Power Sources*, vol. 174, no. 1, pp. 148–158, Nov. 2007.

[39] V. Matolín, M. Cabala, I. Matolínová, M. Škoda, J. Libra, M. Václavů, K. C. Prince, T. Skála, H. Yoshikawa, Y. Yamashita, S. Ueda, and K. Kobayashi, 'Au + and Au 3+ ions in CeO 2 rf-sputtered thin films', *J. Phys. D. Appl. Phys.*, vol. 42, no. 11, p. 115301, Jun. 2009.

[40] S. K. Natarajan and J. Hamelin, 'High-performance anode for Polymer Electrolyte Membrane Fuel Cells by multiple-layer Pt sputter deposition', *J. Power Sources*, vol. 195, no. 22, pp. 7574–7577, Nov. 2010.

[41] S. Motokawa, M. Mohamedi, T. Momma, S. Shoji, and T. Osaka, 'MEMS-based design and fabrication of a new concept micro direct methanol fuel cell (μ-DMFC)', *Electrochem. commun.*, vol. 6, no. 6, pp. 562–565, Jun. 2004.

[42] P. O. López-Montesinos, N. Yossakda, A. Schmidt, F. R. Brushett, W. E. Pelton, and P. J. A. Kenis, 'Design, fabrication, and characterization of a planar, silicon-based, monolithically integrated micro laminar flow fuel cell with a bridge-shaped microchannel cross-section', *J. Power Sources*, vol. 196, no. 10, pp. 4638–4645, May 2011.

[43] L. Dubau, M. Lopez-haro, L. Castanheira, J. Durst, P. Bayle-guillemaud, L. Guétaz, N. Caqué, E. Rossinot, and F. Maillard, 'Applied Catalysis B : Environmental Probing the structure , the composition and the ORR activity of Pt 3 Co / C nanocrystallites during a 3422 h PEMFC ageing test', *"Applied Catal. B, Environ.*, vol. 142–143, pp. 801–808, 2013.

[44] D. F. van der Vliet, C. Wang, D. Li, A. P. Paulikas, J. Greeley, R. B. Rankin, D. Strmcnik, D. Tripkovic, N. M. Markovic, and V. R. Stamenkovic, 'Unique Electrochemical Adsorption Properties of Pt-Skin Surfaces', *Angew. Chemie Int. Ed.*, vol. 51, no. 13, pp. 3139–3142, Mar. 2012.

[45] V. R. Stamenkovic, B. Fowler, B. S. Mun, G. Wang, P. N. Ross, C. A. Lucas, and N. M. Markovic, 'Improved Oxygen Reduction Activity on Pt3Ni(111) via Increased Surface Site Availability', *Science (80-.).*, vol. 315, no. 5811, pp. 493–497, Jan. 2007.

[46] Fuel Cell Technology Office DoE and USA, 'Multi-year Research, Development, and Demonstration Plan - Section 3.4 Fuel Cells', 2016. [Online]. Available: http://energy.gov/sites/prod/files/2016/06/f32/fcto_myrdd_fuel_cells_0.pdf. [Accessed: 07-Aug-2016].

[47] J. W. Coburn and E. Kay, 'Positive-ion bombardment of substrates in rf diode glow discharge sputtering', *J. Appl. Phys.*, vol. 43, no. 12, p. 4965, 1972.

[48] M. Vorokhta, 'Doctoral thesis', Charles University, 2013.

[49] K. Wasa and S. Hayakawa, *Handbook of sputter deposition technology*. 1992.

[50] J. Chastain, Ed., *Handbook of X-ray Phototelectron Spectroscopy*. Minesota: Perkin-Elmer Corporation, 1992.

[51] V. Matolín, M. Cabala, V. Cháb, I. Matolínová, K. C. Prince, M. Škoda, F. Šutara, T. Skála, and K. Veltruská, 'A resonant photoelectron spectroscopy study of Sn(Ox) doped CeO2 catalysts', *Surf. Interface Anal.*, vol. 40, no. 3–4, pp. 225–230, Mar. 2008.

[52] Hüfner Stefan, *Photoelectron spectroscopy: principles and applications. 3rd rev. and enl. ed.*, 3rd ed. Berlin, Heidelberg, New York: Springer-Verlag, 2003.

[53] R. EGERTON, *Physical principles of electron microscopy: an introduction to TEM, SEM, and AEM*. New York: Springer, 2005.

[54] G. Haugstad, *Atomic force microscopy: understanding basic modes and advanced applications*. Hoboken: John Wiley & Sons, Inc., 2012.

[55] C. Heitner-Wirguin, 'Recent advances in perfluorinated ionomer membranes: Structure, properties and applications', *J. Memb. Sci.*, vol. 120, no. 1, pp. 1–33, 1996.

[56] G. Tsotridis, A. Pilenga, G. De Marco, and T. Malkow, 'EU HARMONISED TEST PROTOCOLS FOR PEMFC MEA TESTING IN SINGLE CELL CONFIGURATION FOR AUTOMOTIVE APPLICATIONS'. Publications Office of the European Union, 2015.

[57] H. Wang, X. Yuan, and H. Li, *PEM FUEL CELL DIAGNOSTIC TOOLS*. Boca Raton, FL: Taylor & Francis Group, LLC, 2012.

[58] X. Yuan, H. Wang, J. Colin Sun, and J. Zhang, 'AC impedance technique in PEM fuel cell diagnosis-A review', *Int. J. Hydrogen Energy*, vol. 32, no. 17,

pp. 4365–4380, 2007.

[59] J. Larminie and A. Dicks, *Fuel Cell Systems Explained*, Second edi. Chichester: John Wiley & Sons Ltd, The Atrium, Southern Gate, Chichester, West Sussex PO19 8SQ, England, 2003.

[60] S. H. Overbury, D. R. Mullins, D. R. Huntley, and L. Kundakovic, 'Chemisorption and Reaction of NO and N2O on Oxidized and Reduced Ceria Surfaces Studied by Soft X-Ray Photoemission Spectroscopy and Desorption Spectroscopy', *J. Catal.*, vol. 186, no. 2, pp. 296–309, Sep. 1999.

[61] S. Tanuma, C. J. Powell, and D. R. Penn, 'Calculations of electron inelastic mean free paths. V. Data for 14 organic compounds over the 50-2000 eV range', *Surf. Interface Anal.*, vol. 21, no. 3, pp. 165–176, Mar. 1994.

[62] Y. Chen, P. Hu, M. Lee, and H. Wang, 'Au on (111) and (110) surfaces of CeO2: A density-functional theory study', *Surf. Sci.*, vol. 602, no. 10, pp. 1736–1741, May 2008.

[63] J. G. Wang and B. Hammer, 'Oxidation state of oxide supported nanometric gold', *Top. Catal.*, vol. 44, no. 1–2, pp. 49–56, Jun. 2007.

[64] G. Q. Lu, C. Y. Wang, T. J. Yen, and X. Zhang, 'Development and characterization of a silicon-based micro direct methanol fuel cell', *Electrochim. Acta*, vol. 49, no. 5, pp. 821–828, Feb. 2004.

[65] K. Shah, W. C. Shin, and R. S. Besser, 'A PDMS micro proton exchange membrane fuel cell by conventional and non-conventional microfabrication techniques', *Sensors Actuators B Chem.*, vol. 97, no. 2–3, pp. 157–167, Feb. 2004.

[66] A. Caillard, C. Charles, R. Boswell, and P. Brault, 'Improvement of the sputtered platinum utilization in proton exchange membrane fuel cells using plasma-based carbon nanofibres', *J. Phys. D. Appl. Phys.*, vol. 41, no. 18, p. 185307, Sep. 2008.

[67] D. Gruber, N. Ponath, and J. Müller, 'Microfabricated polymer electrolyte membrane fuel cells with low catalyst loadings', *Electrochim. Acta*, vol. 51, no. 4, pp. 701–705, Nov. 2005.

[68] Y. T. Kim and T. Mitani, 'Surface thiolation of carbon nanotubes as supports: A promising route for the high dispersion of Pt nanoparticles for electrocatalysts', *J. Catal.*, vol. 238, no. 2, pp. 394–401, 2006.

[69] J. M. Ramallo-López, G. F. Santori, L. Giovanetti, M. L. Casella, O. a. Ferretti, and F. G. Requejo, 'XPS and XAFS Pt L 2,3 -Edge Studies of Dispersed Metallic Pt and PtSn Clusters on SiO 2 Obtained by Organometallic Synthesis: Structural and Electronic Characteristics', *J. Phys. Chem. B*, vol.

107, no. 41, pp. 11441–11451, Oct. 2003.

[70] E. Janin, M. Bjijrkqvist, T. M. Grehk, M. Giithelid, C. Pradier, U. O. Karlsson, and A. Rosengren, ‘Hydrogen adsorption on the Pt(111)(sqrt3xsqrt3)R30°-Sn surface alloy studied by high resolution core level photoelectron spectroscopy’, *Appl. Surf. Sci.*, vol. 99, p. 371, 1996.

[71] H. A. Gasteiger, S. S. Kocha, B. Sompalli, and F. T. Wagner, ‘Activity benchmarks and requirements for Pt, Pt-alloy, and non-Pt oxygen reduction catalysts for PEMFCs’, *Appl. Catal. B Environ.*, vol. 56, no. 1–2, pp. 9–35, Mar. 2005.

[72] K. Mašek, M. Václavů, P. Bábor, and V. Matolín, ‘Sn–CeO2 thin films prepared by rf magnetron sputtering: XPS and SIMS study’, *Appl. Surf. Sci.*, vol. 255, no. 13–14, pp. 6656–6660, Apr. 2009.

[73] M. Václavů, I. Matolínová, J. Mysliveček, R. Fiala, and V. Matolín, ‘Anode Material for Hydrogen Polymer Membrane Fuel Cell: Pt–CeO2 RF-Sputtered Thin Films’, *J. Electrochem. Soc.*, vol. 156, no. 8, p. B938, 2009.

[74] K. Kobayashi, M. Yabashi, Y. Takata, T. Tokushima, S. Shin, K. Tamasaku, D. Miwa, T. Ishikawa, H. Nohira, T. Hattori, Y. Sugita, O. Nakatsuka, A. Sakai, and S. Zaima, ‘High resolution-high energy x-ray photoelectron spectroscopy using third-generation synchrotron radiation source, and its application to Si-high k insulator systems’, *Appl. Phys. Lett.*, vol. 83, no. 5, p. 1005, 2003.

[75] S. Tanuma, C. J. Powell, and D. R. Penn, ‘Calculations of electron inelastic mean free paths (IMFPS). IV. Evaluation of calculated IMFPs and of the predictive IMFP formula TPP-2 for electron energies between 50 and 2000 eV’, *Surf. Interface Anal.*, vol. 20, no. 1, pp. 77–89, Jan. 1993.

[76] M. Škoda, M. Cabala, V. Cháb, K. C. Prince, L. Sedláček, T. Skála, F. Šutara, and V. Matolín, ‘Sn interaction with the CeO2(111) system: Bimetallic bonding and ceria reduction’, *Appl. Surf. Sci.*, vol. 254, no. 14, pp. 4375–4379, May 2008.

[77] M. T. Paffett, S. C. Gebhard, R. G. Windham, and B. E. Koel, ‘Chemisorption of carbon monoxide, hydrogen, and oxygen on ordered tin/platinum(111) surface alloys’, *J. Phys. Chem.*, vol. 94, no. 17, pp. 6831–6839, Aug. 1990.

[78] S. Haviar, M. Dubau, J. Lavková, I. Khalakhan, V. Potin, I. Matolínová, and V. Matolín, ‘Investigation of growth mechanism of thin sputter coated cerium oxide films on carbon substrates’, *Science of Advanced Materials*. pp. 1278 – 1285, 2014.

[79] R. Fiala, I. Khalakhan, I. Matolinova, M. Vaclavu, M. Vorokhta, Z. Sofer, S. Huber, V. Potin, and V. Matolin, ‘Pt-CeO2 Coating of Carbon Nanotubes Grown on Anode Gas Diffusion Layer of the Polymer Electrolyte Membrane

Fuel Cell', *J. Nanosci. Nanotechnol.*, vol. 11, no. 6, pp. 5062–5067, 2011.

[80] A. Bruix, Y. Lykhach, I. Matolínová, A. Neitzel, T. Skála, N. Tsud, M. Vorokhta, V. Stetsovych, K. Ševčíková, J. Mysliveček, R. Fiala, M. Václavů, K. C. Prince, S. Bruyère, V. Potin, F. Illas, V. Matolín, J. Libuda, and K. M. Neyman, 'Maximum Noble-Metal Efficiency in Catalytic Materials: Atomically Dispersed Surface Platinum', *Angew. Chemie Int. Ed.*, vol. 53, no. 39, pp. 10525–10530, Sep. 2014.

[81] Y. Lykhach, A. Figueroba, M. F. Camellone, A. Neitzel, T. Skála, F. R. Negreiros, M. Vorokhta, N. Tsud, K. C. Prince, S. Fabris, K. M. Neyman, V. Matolín, and J. Libuda, 'Reactivity of atomically dispersed Pt2+ species towards H2 : model Pt–CeO 2 fuel cell catalyst', *Phys. Chem. Chem. Phys.*, vol. 18, no. 11, pp. 7672–7679, 2016.

[82] V. Johánek, M. Václavů, I. Matolínová, I. Khalakhan, S. Haviar, and V. Matolín, 'High low-temperature CO oxidation activity of platinum oxide prepared by magnetron sputtering', *Appl. Surf. Sci.*, vol. 345, pp. 319–328, Aug. 2015.

[83] R. Fiala, M. Vaclavu, A. Rednyk, I. Khalakhan, M. Vorokhta, J. Lavkova, V. Potin, I. Matolinova, and V. Matolin, 'Pt–CeOx thin film catalysts for PEMFC', *Catal. Today*, vol. 240, pp. 236–241, Feb. 2015.

[84] J. Lavkova, I. Khalakhan, M. Chundak, M. Vorokhta, V. Potin, V. Matolin, and I. Matolinova, 'Growth and composition of nanostructured and nanoporous cerium oxide thin films on a graphite foil', *Nanoscale*, vol. 7, no. 9, pp. 4038–4047, 2015.

[85] G. Wu, K. L. More, C. M. Johnston, and P. Zelenay, 'High-Performance Electrocatalysts for Oxygen Reduction Derived from Polyaniline, Iron, and Cobalt', *Science (80-.).*, vol. 332, no. 6028, pp. 443–447, Apr. 2011.

[86] M. Vorokhta, I. Khalakhan, M. Václavů, G. Kovács, S. M. Kozlov, P. Kúš, T. Skála, N. Tsud, J. Lavková, V. Potin, I. Matolínová, K. M. Neyman, and V. Matolín, 'Surface composition of magnetron sputtered Pt-Co thin film catalyst for proton exchange membrane fuel cells', *Appl. Surf. Sci.*, vol. 365, pp. 245–251, Mar. 2016.

[87] C. S. Rao, D. M. Singh, R. Sekhar, and J. Rangarajan, 'Pt e Co electrocatalyst with varying atomic percentage of transition metal', *Int. J. Hydrogen Energy*, vol. 36, no. 22, pp. 14805–14814, 2011.

[88] I. Khalakhan, M. Vorokhta, M. Václavů, B. Šmíd, J. Lavková, I. Matolínová, R. Fiala, N. Tsud, T. Skála, and V. Matolín, 'In-situ electrochemical atomic force microscopy study of aging of magnetron sputtered Pt-Co nanoalloy thin films during accelerated degradation test', *Electrochim. Acta*, vol. 211, pp. 52–

58, Sep. 2016.

[89] R. Fiala, M. Vaclavu, M. Vorokhta, I. Khalakhan, J. Lavkova, and V. Potin, ‘Proton exchange membrane fuel cell made of magnetron sputtered Pt e CeO x and Pt e Co thin fi lm catalysts’, *J. Power Sources*, vol. 273, pp. 105–109, 2015.

[90] G. Sievers, S. Mueller, A. Quade, F. Steffen, S. Jakubith, A. Kruth, and V. Brueser, ‘Mesoporous Pt e Co oxygen reduction reaction (ORR) catalysts for low temperature proton exchange membrane fuel cell synthesized by alternating sputtering’, *J. Power Sources*, vol. 268, pp. 255–260, 2014.

List of tables

List of figures

List of Abbreviations

AFM: Atomic force microscopy

BE: Binding energy

CNT: Carbon nanotubes

DFT: Density functional theory

DMFC: Direct methanol fuel cell

DOS: Density of states

DWCNT: Double wall carbon nanotubes

ECSA: Electrochemical specific surface area

EDC: Energy distribution curve

EDX: Energy dispersive X-ray spectroscopy

EIS: Electrochemical impedance spectroscopy

CV: Cyclic voltammetry

CVD: Chemical vapour deposition

FC: Fuel cell

FIB: Focus ion beam

FWHM: Full width at half maximum

GDE: Gas diffusion electrode

GDL: Gas diffusion layers

HOPG: Highly oriented pyrolytic graphite

HOR: Hydrogen oxidation reaction

HFR: High frequency resistance

HX-PES: Hard x-ray photoelectron spectroscopy

IMFP: Inelastic mean free path

iR: Internal cell resistance

LCR: Low current density region

MA: Mass activity

MEA: Membrane electrode assembly

nGDL: Gas diffusion layer enhanced with microporous layer of carbon nanoparticles

ORR: Oxygen reduction reaction

OSC: Oxygen storage capacity

PD: Power density

PEM: Proton exchange membrane

PEMFC: Proton exchange membrane fuel cell

PES: Photoelectron spectroscopy

PGM: Platinum group metal

PM: Precious metals

PVD: Physical vapour deposition

RER number: Resonance enhancement ratio

r.f.: Radio frequency

RHE: Reversible hydrogen electrode

RPES: Resonance photoelectron spectroscopy

SA: Specific activity

SEM: Scanning electron microscopy

SMSI/MSI: /Metal-support interaction

SP: Specific power

SRPES: Synchrotron radiation photoelectron spectroscopy

SX-PES: Soft X-ray photoelectron spectroscopy

TEM: Transmission electron microscopy

TWC: Three-way catalysts

UHV: Ultrahigh vacuum

VB: Valence band

WGS: Water-gas shift

XPS: X-ray photoelectron spectroscopy

XRD: X-ray diffraction